LAPPEENRANTA
UNIVERSITY OF TECHNOLOGY

Mikko Valtonen

PERFORMANCE CHARACTERISTICS OF AN AXIAL-FLUX SOLID-ROTOR-CORE INDUCTION MOTOR

Thesis for the degree of Doctor of Science (Technology) to be presented with due permission for public examination and criticism in Auditorium 1383 at Lappeenranta University of Technology, Lappeenranta, Finland, on the 13th of December, 2007, at 12.00.

Acta Universitatis
Lappeenrantaensis
285

Supervisor	Professor Juha Pyrhönen Department of Electrical Engineering Lappeenranta University of Technology Finland
Reviewers / Opponents	Emeritus Professor Tapani Jokinen Helsinki University of Technology Finland
	Associate Professor Irina Ivanova Saint-Petersburg State Polytechnical University Russia

ISBN 978-952-214-473-7
ISBN 978-952-214-474-4 (PDF)
ISSN 1456-4491

Lappeenrannan teknillinen yliopisto
Digipaino 2007

ABSTRACT

Mikko Valtonen

Performance Characteristics of an Axial-Flux Solid-Rotor-Core Induction Motor

Lappeenranta 2007

Acta Universitatis Lappeenrantaensis 285
102 pages, 4 appendices
Diss. Lappeenranta University of Technology
ISBN 978-952-214-473-7, ISBN 978-952-214-474-4 (PDF), ISSN 1456-4491

The integration of electric motors and industrial appliances such as pumps, fans, and compressors is rapidly increasing. For instance, the integration of an electric motor and a centrifugal pump provides cost savings and improved performance characteristics. Material cost savings are achieved when an electric motor is integrated into the shaft of a centrifugal pump, and the motor utilizes the bearings of the pump. This arrangement leads to a smaller configuration that occupies less floor space. The performance characteristics of a pump drive can be improved by using the variable-speed technology. This enables the full speed control of the drive and the absence of a mechanical gearbox and couplers. When using rotational speeds higher than those that can be directly achieved by the network frequency the structure of the rotor has to be mechanically durable.

In this thesis the performance characteristics of an axial-flux solid-rotor-core induction motor are determined. The motor studied is a one-rotor-one-stator axial-flux induction motor, and thus, there is only one air-gap between the rotor and the stator. The motor was designed for higher rotational speeds, and therefore a good mechanical strength of the solid-rotor-core rotor is required to withstand the mechanical stresses. The construction of the rotor and the high rotational speeds together produce a feature, which is not typical of traditional induction motors: the dominating loss component of the motor is the rotor eddy current loss. In the case of a typical industrial induction motor instead the dominating loss component is the stator copper loss. In this thesis, several methods to decrease the rotor eddy current losses in the case of axial-flux induction motors are presented. A prototype motor with 45 kW output power at 6000 min^{-1} was designed and constructed for ascertaining the results obtained from the numerical FEM calculations.

In general, this thesis concentrates on the methods for improving the electromagnetic properties of an axial-flux solid-rotor-core induction motor and examines the methods for decreasing the harmonic eddy currents of the rotor. The target is to improve the efficiency of the motor and to reach the efficiency standard of the present-day industrial induction motors equipped with laminated rotors.

Keywords: axial-flux induction motor, solid-rotor-core, harmonic losses.

UDC 621.313.33 : 62-253

ACKNOWLEDGEMENTS

I wish to thank all the people involved in the process, especially I express my gratitude to Professor Juha Pyrhönen, the supervisor of the thesis for his valuable comments and corrections to the work and for always being encouraging and supporting.

I wish to thank the pre-examiners Associate Professor Irina Ivanova and emeritus Professor Tapani Jokinen for their valuable comments and corrections.

The work is a research project of the AXCO-Motors. Special acknowledgements are due to D.Sc. Asko Parviainen, managing director of the AXCO-Motors, for his guidance during this work and for co-operation facilities.

I also wish to thanks M.Sc. Mika Neuvonen for his valuable guidance during the measurements in the laboratory. I am indebted to the laboratory personnel Mr. Jouni Ryhänen Mr. Juha Haikola, Mr. Martti Lindh and Mr. Harri Loisa, for the assistance during the construction of the laboratory prototypes as well as for the practical arrangements in the laboratory.

Many thanks are due to PhD Hanna Niemelä for her contribution to improve the language of this work.

Financial support by Walter Ahlströmin Säätiö, Tekniikan edistämissäätiö and Lappeenrannan teknillisen yliopiston tukisäätiö are grateful acknowledged.

I am deeply indebted to my parents, Tuula and Ilkka, for providing me a good basis for life.

Most of all and with all my heart I am grateful to my wife Elina for her love and patience during the busy years and to my son Tommi, for giving me strength and motivation for this work.

Lappeenranta, November 2007

Mikko Valtonen

CONTENTS

SYMBOLS AND ABBREVIATIONS

Roman letters

a	number of parallel paths in windings
A	linear current density
$\boldsymbol{A}$	magnetic vector potential
a_{1k}	variable
b_r	rotor slot width
b_s	stator slot width
B	magnetic flux density
$\boldsymbol{B}$	magnetic flux density, vector
d	thickness
D_s	inner diameter of the stator
D_{se}	outer diameter of the stator
$\boldsymbol{D}$	electric flux density, vector
$\boldsymbol{E}$	electric field strength, vector
f	frequency
f_{sw}	switching frequency
F_m	magnetomotive force (mmf)
F_{tan}	tangential force
g	coefficient, constant
$\boldsymbol{H}$	magnetic field strength, vector
i	current
I	current
j	imaginary unit
J	current density
$\boldsymbol{J}$	current density, vector
k	factor, coefficient
k_C	Carter factor
k_{Fe}	space factor of the iron
k_w	winding factor
K	transformation ratio
l_e	equivalent core length
l_{ew}	average conductor length of winding overhang
l_m	length of one turn of the winding
$\boldsymbol{l}$	unit vector collinear to the integration path
L	inductance
m	number of phases
n	rotation speed, ordinal of harmonic
N	number of the turns in a winding per phase
p	number of pole pairs
P	power
P_l	additional loss
q	number of slots per pole and phase
Q	number of slots
r	radius
R	resistance, radius
s	slip
S	apparent power
S_c	cross-section area of conductor

S_r	rotor surface area facing the air-gap
t	time
T	torque
$\boldsymbol{T}$	electric vector potential
u	voltage, variable
U	voltage
V	volume
w	length
W	coil span (width)
Z_s	surface impedance

Greek letters

α	angle
β_1	variable
γ	coefficient
δ	air-gap (length)
δ_{er}	equivalent air-gap
ε	permittivity
η	efficiency
Θ	current linkage
λ	inductance factor
μ	permeability
μ_r	relative permeability
μ_0	permeability of vacuum
ν	ordinal of harmonic
ρ	resistivity, electric charge density
σ	tension, leakage factor, conductivity
τ_p	pole pitch
τ_r	rotor slot pitch
τ_s	stator slot pitch
υ	reluctivity
Φ	magnetic flux
ϕ	magnetic flux, electric scalar potential
Ψ	magnetic flux linkage
ψ	magnetic scalar potential
χ	chord factor
Ω	scalar potential
ω	angular frequency

Subscripts

av	average
d	tooth
DC	direct current
e	excess
EC	eddy current
Hy	hysteresis
in	inner
j	source

m	magnetic
max	maximum
min	minimum
n	nominal
out	outer
pad	coating pad
ph	phase
r	rotor
red	reduced
s	stator, supply
tan	tangential
w	end winding leakage flux
x, y, z	coordinate
yr	rotor yoke
1	fundamental

Acronyms

AF	axial-flux
CEMEP	Comité Européen de Constructeurs de Machines Electriques et d'Electronique de Puissance (European committee of manufacturers of electrical machines and power electronics)
EC	European Commission
FEA	finite element analysis
FEM	finite element method
IM	induction motor
MLTM	multi-layer transfer matrix
mmf	magnetomotive force
PM	permanent magnet
PWM	pulse width modulation
RF	radial-flux
2D	two-dimensional
3D	three-dimensional

1. Introduction

Axial-flux (AF) electric motors are an interesting alternative when integrating the motor and the working machine in future applications. The degree of freedom in designing the configuration may be larger compared with the traditional solutions, in which stand-alone electric motors are used. Although the operating principles of AF machines are the same as those of traditional radial-flux (RF) machines, the design principles of AF machines and their characteristics may differ remarkably from those of traditional motors.

This study concentrates on determining the characteristics on an AF induction motor (IM) with one rotor–one stator configuration, which is often easy to integrate directly into the working machine, such as a pump, fan, or compressor. The nominal speed of the motor type studied was designed to be higher than what could be reached directly by means of network frequency. When using higher rotational speeds, the mechanical strength of the rotor has to be high enough. Because of mechanical and constructional reasons, the rotor core of the studied AFIM was manufactured from solid steel. The rotor was also equipped with an aluminium winding manufactured using a high-strength aluminium plate as a starting point.

Using the geometric mean radii $R_{av} = (R_{in} \cdot R_{out})^{1/2}$ of the motor and by applying the theory of conventional RFIMs suitably modified, a prototype motor was first designed and manufactured. The performance characteristics of the prototype motor were determined with finite element (FE) calculations and numerous measurements. It has to be noticed that the prototype motor was not a result of any optimization process; further and in this work, only some guidelines for the design of solid-rotor-core AFIMs are given. The reason for this is that the performance analysis of the saturated AFIM is very complicated because of the disc-shape geometry and the saturation effects in the solid-rotor-core.

The conductors in conventional RF motors are axially arranged, and thus the axial variation of the air-gap field may be neglected or it is taken into account by using the equivalent core length of the machine instead of the real stack length in the design. This assumption leads to a two-dimensional (2D) field problem, and hence the performance calculation may be greatly simplified. However, in AF motors, the conductors are radially arranged, and thereby the pole pitch and the tooth width will increase when increasing the core diameter, as shown in Fig. 1.1.

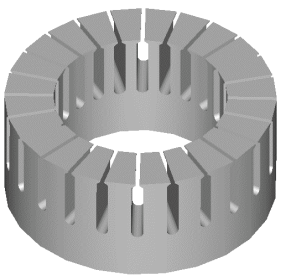

Fig. 1.1 Laminated stator core of an 11 kW, 7200 min^{-1} AFIM. Stator windings are not illustrated.

Therefore, the radial air-gap field distribution of AF motors is non-uniform, in other words, it constitutes a three-dimensional (3D) field calculation. The number of the volume elements in the air-gap regime of the electrical machines tends to be large, because a dense mesh is

required. For large machines, including one or two pole pairs, the size of the system matrix grows large, and computers cannot smoothly handle the matrices. Computation of the numerical field in 3D gives accurate results, but it is also very cumbersome, time-consuming and hence too expensive for present-day personal computers for practical design issues. Thus, it cannot be used in machine design optimization either.

There are several topologies of induction motors. RFIM is one of the most popular motor types because of its low manufacturing costs and high reliability. RFIMs are relatively long in the axial dimension, and a large fraction of the length of an RFIM is attributed to the end turns of the windings. Another topology for an induction motor is the AF motor. AFIMs are very attractive in applications in which the axial length of the machine is a limiting design parameter.

The history of electrical machines shows that the earliest machines were AF machines. In 1821, based on the principle of electromagnetic induction, Faraday invented a primitive disc motor, which was in the form of an AF motor (Atherton, 1984). However, AF machines were replaced by RF machines after a relatively short period of time. That was mainly because of a strong magnetic force existing between the stator and the rotor. In 1837, Davenport claimed the first patent for an RF machine and, later, it became the generally accepted configuration for electrical machines (Chan, 1987). RF machines have been very popular and form still the mainstream in the design of electrical machines. Printed circuit DC servomotors and homopolar machines are, however, examples of AF machines.

An important drawback of the single-stator-single-rotor AF machines is the strong magnetic pull between their stators and rotors. This problem can be alleviated by using a sandwich configuration with a rotor sandwiched between two stators or a stator sandwiched between two rotors. Figure 1.2 shows the basic topologies of the magnetic circuit of the AF machines.

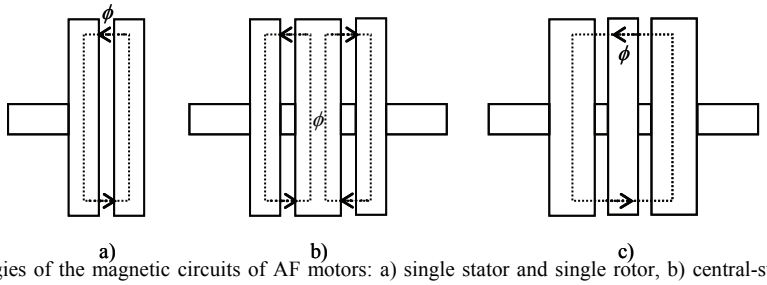

Fig. 1.2 Topologies of the magnetic circuits of AF motors: a) single stator and single rotor, b) central-stator motor, and c) central-rotor motor. ϕ is the magnetic flux.

Motors constructed using a single stator and a single rotor (Fig. 1.2 a) experience a strong attracting magnetic force between the stator and the rotor. Therefore, the sandwich configurations, shown in Fig. 1.2 b) and c), appear much more viable from this point of view. The central-stator motor produces more torque per length of the stator conductor, since both of the stator core surfaces are used as working surfaces of the machine. This configuration, however, has several uncertainties in its mechanical construction. Supporting of the central stator is very difficult, which is the reason why this design is often neglected. The major concern for the topology 1.2 c) at a high peripheral speed (> 100 m/s) is the possibly too low mechanical strength of the rotor core. Figure 1.3 illustrates the deformation of a double-sided AFIM rotor under a rotation; the rotor topology is shown in Fig. 1.2 c). Such a rotor can be produced by using a strong cage winding that supports the whole rotor construction. A pure

solid steel disc would have too poor a performance for a practical motor. The rotor of the type 1.2 c) can be constructed by using high-strength aluminium as the winding material. A strong aluminium cage can support the necessary magnetic parts of the rotor that carry the flux from one stator to another.

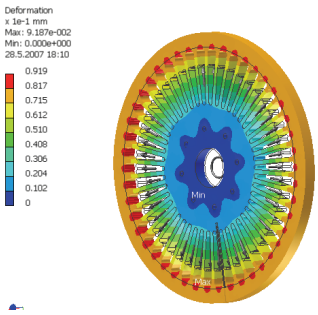

Fig. 1.3 Deformation in the rotor core resulting from rotation-caused forces.

In order to produce an efficient motor, most induction motors are constructed using materials in the stator and rotor yokes of the motor that minimize the losses caused by eddy currents and hysteresis. For example, conventional RFIMs have laminated magnetic circuits, often produced using punched, round steel laminations. Similarly, the magnetic cores of AFIMs can be fabricated using laminated steel. The laminations have to be shaped and arranged in such a way that unifies the lamination direction with the flux direction. These laminated sheets are used to reduce the eddy currents in the magnetic cores.

A normal laminated rotor cannot be used in high-speed machines because of its weakness and insufficient rigidness; one must be satisfied with a solid-rotor that in electromagnetic terms is notably weaker than a laminated one, the mechanical properties of which are yet superior. The solid-rotor-core can be used in conjunction with mechanical bearings at elevated speed, since the rotor easily maintains its balance. Especially in cases, in which elevated speeds are used and the load is connected directly onto the solid-rotor shaft, the solid-rotor construction is still able to achieve a sufficient mechanical strength and avoid natural mechanical vibrations, which might damage the bearings. Nevertheless, when a solid-rotor-core is used, it is essential to take special care of the flux density distribution on the rotor surface. The flux density distribution should be sinusoidal on the surface of the rotor to achieve the lowest possible losses.

The main advantages that are achieved, when the motor is used in a high-speed range are: the reduction of the motor size, and the absence of a mechanical gearbox and couplers. When appropriate materials are used, the volume and weight per power ratio are nearly inversely proportional to the rotating speed in high-speed range. This is valid only for open motor constructions. If a totally closed construction is used, the benefit of the reduced motor size is lost unless a very effective cooling is arranged. According to Jokinen and Arkkio (1999) in very high-speed machines the mechanical losses, that is, the friction, cooling and bearing losses, are the most dominating loss component. The reason for this is that the friction losses of the total machine losses are proportional to the square of the rotational speed. In high-speed machines the proportion of I^2R losses of the total machine losses decreases with the increasing speed, the proportion of hysteresis loss remains constant, and the proportion of the eddy current losses increases proportional to the speed. Iron losses can be reduced by using thin

electrical sheets with high aluminium and silicon content. Thus, the stator current density in high-speed machines can be higher than in low-speed machines.

AFIMs are not as well applicable for a high-speed range than RFIMs, because the characteristics of an induction machine are usually the best when there are only a few poles (2 or 4) in the machine. The inherent characteristics of an AF machine (i.e, the short rotor but with a large diameter) rotor produce excessive frictional losses at high speeds, and also the mechanical strength of the rotor core appears to be insufficient.

In the case of AF motors, a two-pole solution is often unsuitable, because the end-winding arrangements in a two-pole machine are impractical. Therefore, an AF machine has usually to be designed at least as a four-pole configuration. In that case, both the magnetic flux in the stator yoke and the currents in the windings of the machine have to flow a quarter of the inner and the outer peripheries of the machine tangentially without producing torque.

The stator of the AF motor can be fabricated of electrical steel strip by punching the slots and winding the core, and thus the loss of electrical steel material is very small, and the AF machine becomes very short. Permanent magnet (PM) AF machines, in particular, are found in practical embodiments. In 1967, Parker presented a well-known technology for the AFIM. The rotor of the AF motor described in his patent was fabricated by casting. The structure is simple and easy to construct, but its disadvantage is its low durability already at moderately high rotation speeds. A laminated rotor core spiral has no radial strength, and therefore the die-cast aluminium constituting the rotor winding has to take care of the radial strength of the rotor. The die-cast aluminium is usually as pure aluminium as possible, and hence also its yield strength is also very low. Therefore, the structure is suitable only for low rotation speeds, usually below 1500–3000 rpm.

The rotor construction used in this work should eliminate the aforementioned drawbacks. The rotor configuration with a solid steel core and high-strength aluminium windings is simple and compact and endures also high rotation speeds. The construction may, if needed, also be reinforced with suitable integrity-retaining rings. The motor construction used in this work can be conveniently integrated with various power tools, such as pumps, blowers, and compressors.

1.1 Applications of axial-flux motors

The concept of an induction motor with a disc rotor, because of its short length, can easily be adopted in the construction of various devices, and it also has advantages in terms of size, appearance, and function. Despite the many advantages and application possibilities of the AF machine for example in centrifuges, compression refrigerators, hermetic centrifugal pumps, fans, control and industrial engineering systems, etc., induction motors with disc rotors are quite rare in production (Kubzdela and Weglinski, 1988). AFPM machines are used in special applications with special constructional boundary conditions, such as very limited size. Such applications are, for example, electric vehicle wheel motors (Profumo et al., 1997) and direct-drive elevator motors (Hakala, 2000). Typically, AFPM machines have been used in integrated high-torque applications. The lift motor application (Hakala, 2000) is a good example of integration into an application in which the machine shortness is essential. The machine is a single stator–single rotor construction. The strong attracting forces between the stator and the rotor are not a problem, since the machine has to support the lift wire tension that supports the lift cage and its load. In such an application, the attracting forces are easily

tolerated by the overall machine construction. By assembling several machines on the same shaft, more complex arrangements can be found. Such multistage AFPM machines may be considered for ship propulsion drive use (Caricchi et al., 1995), pump (Caricchi et al., 1998), and high-speed PM generator applications (El-Hasan et al., 2000).

In 1978, Brimer patented an AFIM, which was used as a washing machine agitator. The AF motor was constructed of two facing stators and a thin disc rotor between the stators. The rotor was fabricated from aluminium, and thus the rotor currents were flowing in a low-resistivity material. A ferromagnetic material, such as iron or steel was not considered. A problem with the use of copper or aluminium material for the rotor disc was the resulting lack of structural rigidity in the rotor. At that time, also other AFIMs having disc-shaped rotors were designed. The rotors were fabricated from a high-conducting material, wherein small portions of the rotor were fabricated from ferromagnetic material. The ferromagnetic material was inserted into the rotor as an attempt to enhance the flux-carrying capacity of the rotor. For example, Senckel (1976) disclosed a two-phase asynchronous motor having a rotor with ferromagnetic bridges disposed between two offset-facing stator portions. The ferromagnetic bridges were laminated to prevent current from travelling through the ferromagnetic bridges and instead causing current to flow around the bridges. Such a rotor is very light and particularly suitable for high-speed operation.

Lee (1965) presented a dynamo electric machine having a rotor disc fabricated primarily from copper or aluminium. In the rotor, there were axially oriented iron strands, which, however, did not promote the electrical conductivity of the rotor. Therefore, the ferromagnetic material portions in the rotor of the AFIMs proposed by Senckel (1978) and Lee (1965) did not increase the current-carrying capacity of the rotor, although they were designed to enhance the flux-carrying capacity of the rotor. The problem in both Senchel's and Lee's inventions is that the ferromagnetic inserts were attracted to the stators by very large forces, and the copper and aluminium discs were not sufficiently rigid to maintain the small air-gaps, necessary from the power factor point of view.

Morinigo (1996) patented an AFIM having two facing stators and one ferromagnetic and also conducting rotor. The rotor was made of ferromagnetic material; the bulk of the disc shape rotor was fabricated from solid, low-carbon steel. In order to improve the energy efficiency of the motor, the rotor includes also copper bars and outer and inner conduction rings, which are embedded within the rotor. The copper bars were skewed. The angle of skewing was a few degrees. The machine can be used as a motor, a generator, or an alternator/starter.

In 1997, Gerling and Lürkens patented an AFIM that has one stator and a disc rotor facing the stator. Figure 1.4 shows the construction of the motor. The rotor disc was fabricated of two materials; the first material has a relatively high magnetic permeability – in practice this material is iron – and a higher gravity than the second material. The second material has a relatively high electrical conductivity, and the material is for instance aluminium. The aluminium part was in the form of an annular ring. The ring was embedded in or supported by another surface of the iron disc. There can be two or more aluminium ring segments. Another surface of the iron disc faced the stator. An AFIM was constructed in a vacuum cleaner that has an impeller wheel, which was directly coupled to the rotor of the motor, the rotor and the impeller wheel having the same outer radius.

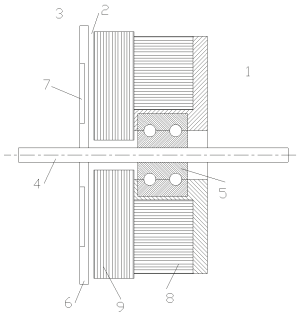

Fig. 1.4 Structure of the motor patented by Gerling and Lürkens (1997). The AFIM has a stator 1 and a rotor 3 displaced by a radial air-gap 2, the rotor of which is mounted on a shaft 4, which is supported by means of a bearing 5. The rotor 3 is made of two materials, i.e., an electrically conductive material 6 (aluminium) and a high-permeability material 7 (iron). The high-permeability material 7 has a higher specific gravity than the electrically highly conductive material 6, is given an annular ring shape, and is embedded in the rotor 3 in such a way that only a layer of the electrically highly conductive material 6 is situated at the side facing the stator 1. The stator 1 has an iron sleeve 8 formed by coiling and electric-sheet band and provided with slots for receiving a winding 9 (Gerling and Lürkens, 1997).

The end turns of the AFIM are not located in an area where the end turns contribute to the length of the motor, but the diameter of the rotor of the AFIM offers the potential for high energy densities related to the radial design. By constructing the rotor of the AF motor such that it has the shape of an impeller of the pump, a short profile in the axial direction can be achieved. Additionally, by using power-electronics-controlled high-speed AF solid-rotor-core IM drives, no mechanical gearboxes are needed when a load-machinery is directly attached on the motor shaft. This gives a full speed control for the drive.

Gearboxes are normally used to reduce or increase the speed. In Fig. 1.5 a) a gearbox takes up space and needs maintenance as well as considerable quantities of oil. By eliminating the gearbox, it is possible to achieve space savings and installation costs, because only one piece of foundation is needed for the driving machinery, as illustrated in Fig. 1.5 b). Additionally, the length and weight of the drive can be reduced by eliminating the gearbox and by employing a high-speed motor.

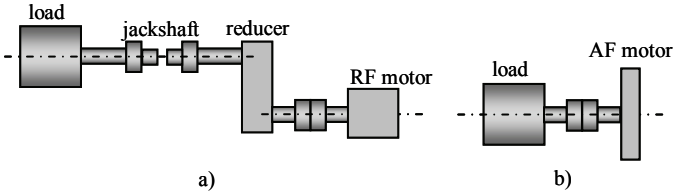

Fig. 1.5 Interface of motor and load. a) Conventional drive and b) gearless AFIM drive.

By eliminating the gearbox, an improved efficiency of the drive can be achieved. The power out of the gearbox and the power put into the gearbox are not equal. Considering that power is made up of speed by torque, one of the two must be lost. It is not possible to lose speed because of the meshing of the gears, and thus the efficiency rating of a gearbox relates to the torque. While gears are turning, dynamic friction causes some loss of torque, whereas static friction causes loss of torque at all times. During acceleration, the inertia of gears causes a loss of some torque. With gearboxes, some position may be lost if there is some backlash in the gears, that is, the gears do not mesh perfectly. Friction and backlash between gears may vary,

if there is any eccentricity between the gears, which can also lead to vibration problems (Laurila, 2004).

The development of frequency converter technology has made the variable speed technology of induction motors feasible in a wide range of applications. There exists a growing need for direct-drive variable-speed systems. There are no need for reducing or multiplier gears when direct-drive systems are used. Direct-drive systems are economical in both energy and space consumption, and additionally, direct drives are easy to install and maintain. Figure 1.6 illustrates an integrated single-shaft screw compressor solution from ALUP (Alup, 2004). The motor is a traditional RFIM.

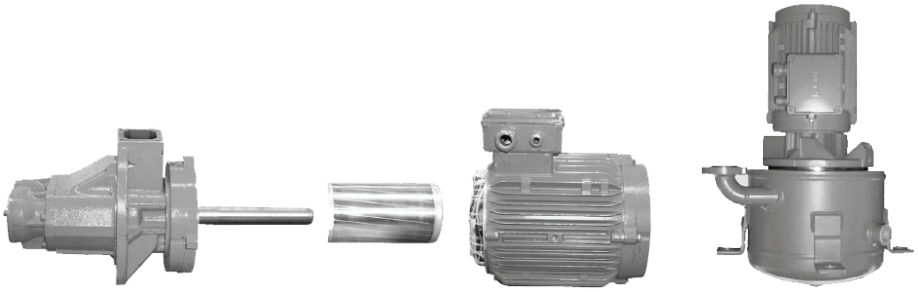

Fig. 1.6 Variable-speed rotary screw air compressor. The compressor shaft and the rotor of the motor form one piece, and thus, no coupling elements are needed. Additionally, there is no need for motor bearings, which increases the operating safety. Generally, loss-free power transmission can be expected with this construction.

With industrial induction motors, the stator copper losses are typically the dominating loss component. Figure 1.7 shows the typical distribution of the loss components and motor main dimensions when comparing a traditional two-pole industrial cage-induction motor and the AFIM studied.

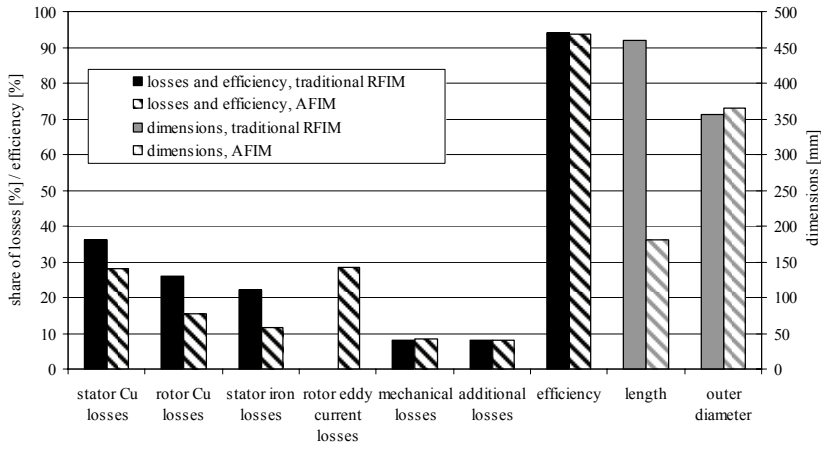

Fig. 1.7 Comparison between a 45 kW, two-pole, 3000 min^{-1} traditional RFIM and a 45 kW, four-pole, 6000 min^{-1} solid-rotor-core AFIM. Stator copper loss is the most dominating loss component with RFIM, while the rotor eddy current loss caused by the air-gap harmonics is the most dominating loss component in the solid-rotor-core AFIM. The rated efficiency of the RFIM is somewhat higher than the efficiency of the AFIM. The power factors of RFIM and AFIM are 0.88 and 0.67, respectively. The outer diameter of the AFIM is about 10 mm longer than the outer diameter of the RFIM. However, the length of the AFIM is approximately half of the length of the RFIM. The RFIM used as a reference belongs to the highest efficiency class level EFF1 motor according to EC/CEMEP.

The AFIM studied was fed by a frequency converter, and thus there are voltage and current harmonics present. Also the discrete distribution of the slots causes winding harmonics, and the local permeance minima under the slots cause permeance harmonics. These harmonics cause eddy current losses on the solid-rotor-core, as can be seen in Fig. 1.7. The results of this comparison justify one of the main topics in this thesis – the minimization of the eddy current losses on the solid-rotor parts. This is very important, because the efficiency of the motor depends largely on the harmonic eddy current losses. Stator and rotor copper losses are generated in the stator and rotor windings according to Ohm's law. Stator iron losses are generated in the conducting core laminations, and they can be divided into hysteresis, eddy current and excess losses. The rotor iron losses, however, are neglected because in speed-controlled induction motor drives, the motor operates on the linear part of the torque-speed curve, where the rotor frequency is low. According to IEC 60034-2 standard, additional losses or stray load losses are defined as a fraction of the machine input power ($P_l = 0.005P_{in}$). Additional losses are caused by leakage fluxes and high-frequency flux pulsations, which generate iron and eddy current losses. Mechanical losses can be divided into friction losses, which are generated in the bearings, and windage losses.

Figure 1.8 illustrates the power balance of one of the AFIM studied. Approximately 6.5 per cent of the input electric energy is converted into heat at the nominal power of the motor. The proportions of the rotor eddy current losses and the stator copper losses are high – around 1.9 and 1.8 per cent each. The proportion of the stator iron losses remains low.

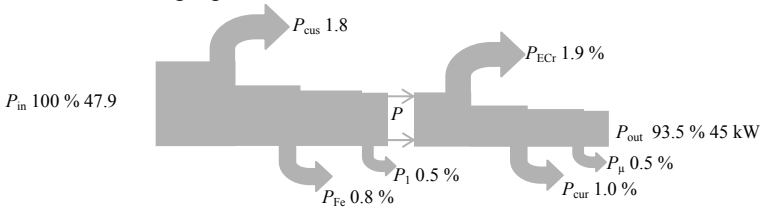

Fig. 1.8 Sankey diagram for one of the 45 kW four-pole 6000 min^{-1} induction motors. P_{ECr} indicates the rotor eddy current losses, P_{Fe} the stator iron losses, P_{Cus} the copper losses of the stator, P_l the additional losses, P_δ the air-gap power, P_{Cur} the copper losses of the rotor, P_μ the friction losses. The total losses are 2.9 kW. The large portion of rotor eddy current loss separates this type of the machine from the traditional squirrel cage motor.

1.2 Principles of an AF solid-rotor-core induction motor

Figure 1.9 presents an AFIM studied in this work. The motor comprises a frame, a shaft (1) which is bearing mounted to the frame, a disc rotor (2) which is supported by the shaft, a stator (4) which is supported rotatably by the frame and stator windings (3). The rotor frame (8) is fabricated of a non-ferromagnetic material, for instance cast aluminium, which has a high electrical conductivity. The rotor frame is comprised of a uniform inner periphery (10), an outer periphery (9), and conductor bars (11). The conductor bars are galvanically connected to the peripheries. Additionally, the conductor bars together with the inner and outer peripheries constitute the cage winding of the rotor. Between the inner and outer peripheries of the rotor there are ferromagnetic pieces (12). These ferromagnetic pieces extend through the rotor frame plate and are spaced apart from each other at a suitable distance so that the radial conductor bars of the rotor are located appropriately between the pieces. This AFIM construction is presented in the patent of AXCO Motors (2004).

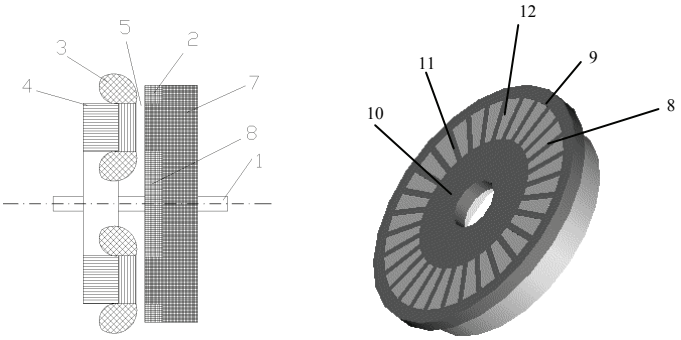

Fig. 1.9 AF motor and the rotor of the motor studied in this work in which there is a shaft (1) rotating with respect to the machine frame, and a rotor (2) supported to the shaft. A stator (4) is supported to the machine frame and comprising a stator winding (3). An air-gap (5) is between the rotor (2) and the stator (4). (7) is an element that conducts the magnetic flux, the element is the rotor yoke (7). The rotor yoke (7) is fabricated from ferromagnetic solid steel. The rotor frame plate (8) (the "cartwheel") is machined of work-hardened, rolled sheet of suitable aluminium alloy. The rotor frame (8) is comprised of a uniform inner periphery (10), an outer periphery (9) and conductor bars (11). Between the inner and outer peripheries of the rotor there are ferromagnetic pieces (12).

Traditionally, as pure aluminium as possible is used in casting the cage windings of the rotor of the machine in induction motors. In the case of the AF motor studied, appropriately composed aluminium alloy is used both in the electrically conductivity structure and in the actual rotor frame structure, which is machined of rolled or work-hardened aluminium alloy sheet. The electrical resistivity of the aluminium alloys varies between 3.6–6.7 μΩcm and the relative permeability of the aluminium alloy is approximately one ($\mu_r \approx 1$) (Aluminium handbook, 1999). The resistivity of pure aluminium is 2.9 μΩcm, which is somewhat better than the resistivity of the aluminium alloys. However, pure aluminium is mechanically soft, and therefore its use in medium and high-speed motors cannot be justified.

The ferromagnetic pieces between the inner and outer peripheries of the rotor are used as a path for the magnetic flux. These ferromagnetic pieces are fabricated of common structural steel Fe52. The saturation flux density and the permeability of steel Fe52 are high, and thus the steel is suitable for carrying the magnetic flux through the rotor. These ferromagnetic parts in the rotor cause centrifugal forces during rotation. When using a strong aluminium in the entire rotor, that is, both in the rotor frame and in the short-circuit rings, a firm structure is achieved that can also well withstand the centrifugal forces. From the electromagnetic point of view, the solid steel parts can be replaced with laminated materials to reduce iron losses. The structural durability is nevertheless not as good as with a laminated material. The permeability and the saturation flux density values of the material that carries the magnetic flux through the rotor should be high. However, it is typical for ferromagnetic materials to have a low electrical conductivity (the room temperature resistivity of the Fe52 is about 26.0 μΩcm), and when the electrical conductivity becomes lower, also the saturation flux density becomes lower. Therefore, a satisfactory compromise has to be found when a ferromagnetic material is chosen. Chapter 4 presents the resistivities and *BH* curves of Fe52 steel and two other commercial ferromagnetic materials.

In the case of the studied AFIM shown in Fig. 1.9, the annular element (7) for the conduction of the magnetic flux is supported to the rotor. Thus, the element is a part of the rotating rotor. The element is a solid steel rotor yoke, not a laminated element. However, the function of the element is again to carry the flux in the rotor over the pole pitch so that the flux can return to the stator. The main drawback in this case is a large axial force that is present between the

stator and the rotor. However, it can be accepted in certain embodiments. Of course, from the electromagnetic point of view, a solid-rotor yoke is an unwanted solution, but when the rotor winding is manufactured from aluminium, the slip frequency of the rotor is very low (< 1 per cent), and thus the solid-rotor yoke is only a marginal disadvantage. By using the rotor construction of the studied AFIM shown in Fig. 1.9, a blower or pump blade can be fixed directly on the rotating rotor yoke. In that case, it is possible to build a fully integrated machine solution. The construction of the studied AFIM has significant advantages: the machine configuration becomes very short, it is easy to manufacture, and the rotor is very durable when compared with traditional rotor constructions. The high rigidity enables high rotation speeds.

The rotor frame comprises two or a plurality of work-hardened aluminium alloy plates. The rotor frame, that is, the rotor winding, was manufactured by punching high yield strength aluminium "cartwheels" of aluminium plate having resistivity of 3.6 μΩcm. In any case, the mechanical strength of the rotor is relevant. The durability of the rotor can be increased by using carbon fibre plates on the surface of the rotor or preferably between the aluminium plates of the rotor. The fibres have to be oriented to obtain the centrifugal forces acting in the direction of the rotor radius. Tightening of the rotor structure in radial direction will take place during operation because the carbon fibre contracts when it warms up.

A disadvantage of the AFIM is the presence of axial magnetic force that acts on the rotor bearing. Therefore, manufacturers are forced to apply a special kind of bearing, sometimes a very expensive one. However, in some applications, there are trust bearings of this kind, and they are usually oil lubricated. The axial force of the AFIM can be decreased by using a laminated annular disc (7) fabricated of ferromagnetic material, which conducts the magnetic flux as shown in Fig. 1.10.

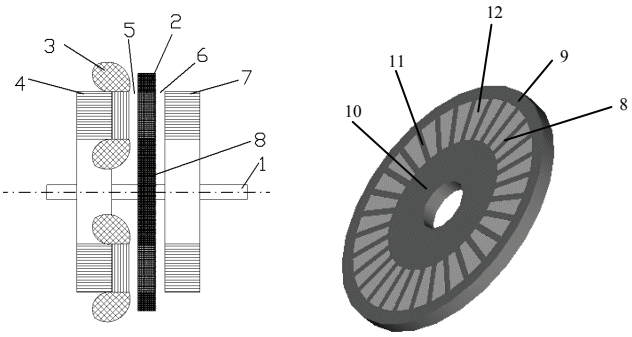

Fig. 1.10 AFIM, in which there is a shaft (1) rotating with respect to the machine frame, and a rotor (2) supported to the shaft. On the first side of the rotor (2) there is a stator (4) supported to the machine frame and comprising a stator winding (3). There is a air-gap (5) between the rotor (2) and the stator (4), and the corresponding air-gap (6) on the other side of the rotor. (7) is an element that conducts the magnetic flux, the element is the rotor yoke (7) that is fixed with respect to the frame. The rotor yoke (7) is fabricated from laminated electrical sheet. The rotor frame plate (8) is machined of work-hardened, rolled sheet of suitable aluminium alloy. The rotor parts (8), (9), (10), (11), and (12) are presented in Fig. 1.9. This AFIM construction is patented by AXCO Motors (2004).

An annular disc (7) shown in Fig. 1.9 is supported to the machine frame. It is stationary and at an appropriately small air-gap distance from the rotating rotor. The stationary rotor yoke constitutes in practice the magnetic back part to the rotor, through which the magnetic flux passes over a pole pitch and then returns through the rotor, and back to the stator. By using the annular element, the machine produces very little axial force, because nearly the same magnetic flux flows over both air-gaps of the machine. If high-quality electrical steel is used

in the stationary yoke, the power factor of the system could, at least in principle, be improved but this construction; however, it easily suffers from reduced performance. The secondary air-gap may be made very small, since no permeance variations are present, but still the double air-gaps tend reduce the power factor of the machine and the additional “dummy”; also the stator generates iron losses, since it is exposed to the same fundamental frequency flux variation as the actual active stator. Instead of a dummy stationary rotor yoke, an active secondary stator may of course be used. In such a case, the rotor current-carrying surface must, of course, be increased correspondingly.

By using two stators, one at both sides of the rotor, the magnetic flux of the AF machine flows over both air-gaps, in which case only a marginal amount of axial magnetic net attractive force is produced in the machine. This AFIM construction is presented in the patent of AXCO Motors (2004).

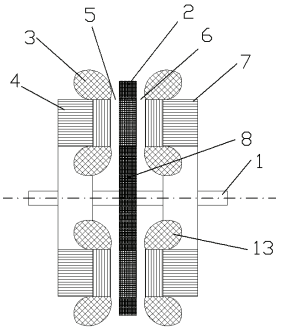

Fig. 1.11 AF induction motor in which there is a shaft (1) rotating with respect to the machine frame, and a rotor (2) supported to the shaft. On the first side of the rotor (2) there is a stator (4) supported to the machine frame and comprising a stator winding (3). There is the element (7) to conduct the magnetic flux instead is a construction corresponding to the stator (4), comprising the stator windings (13). There is a small air-gap (5) between the rotor (2) and the stator (4), and the corresponding air-gap (6) on the other side of the rotor. The rotor frame plate (8) is machined of work-hardened, rolled sheet of suitable aluminium alloy.

When two stators and two air-gaps in the motor are used as is shown in Fig. 1.11, the bearing requirement in the machine is simplified. The magnetic flux is not allowed to flow tangentially in the rotor disc; otherwise a precondition for this kind of force balance is lost. In practice, the magnetic flux flows very directly through the rotor, yet being tangentially almost non-ferromagnetic. In the rotor, there are only ferromagnetic pieces guiding the magnetic flux in the axial direction through the rotor from one stator to another.

1.3 Scope of the work

AFIMs do not compete with conventional motors for general usage, because they have properties which are advantageous in certain special applications. AFIMs have some notable advantages when compared with the conventional RF machines. For example, the rotor of the AF motor can be entirely supported by the load to be driven by the motor. The load machinery may inherently have strong enough bearings that are capable of compensating the attractive forces between the stator and the rotor in a single-stator-single-rotor motor type. Thus, the motor itself does not need to contain the bearings and associated parts required in a conventional RF machine. Another example is small pump motors, in which the stator is separated from the rotor and the impeller by a membrane. This removes the need for a leak-proof seal around a rotating shaft. Figure 1.12 shows two examples of applications in which the AFIM studied can be used. On the left-hand figure, a screw compressor is integrated on

the shaft of the AF motor, and on the right-hand figure, the centrifugal pump is integrated on the shaft of the AF motor. The AF motors in these specific applications use the inherently strong bearings of the regulated units.

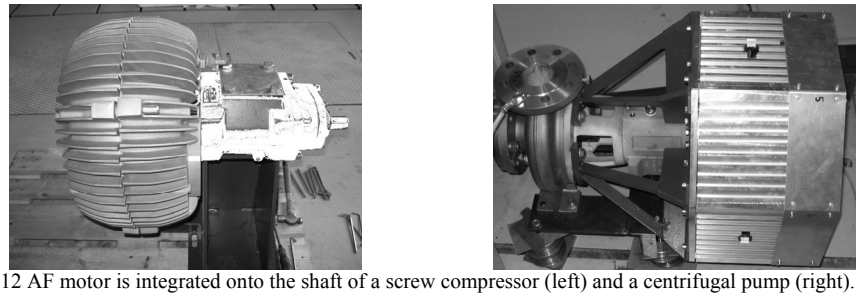

Fig. 1.12 AF motor is integrated onto the shaft of a screw compressor (left) and a centrifugal pump (right).

AF induction motors have not, so far, been commercially successful. This is believed to at least partly result from the fact that such AF motors have incorporated some of the disadvantages and restrictive features of the conventional radial-flux machines. Motors constructed using the single-stator-single-rotor construction experience a strong magnetic pull between the stator and rotor and therefore, the sandwich configuration appears much more viable from this point of view. In the sandwich configuration, several other benefits of the motor type are lost. For instance the constructional degrees of freedom are greatly limited when two stators are applied. The improvements of manufacturing processes, materials and frequency converters are opening up opportunities for AF induction motors to be commercially successful in the future.

The main objective of this thesis is to define the performance characteristics of the one-rotor one-stator AFIM configuration by numerous measurements and FEM calculations. The rotor is fabricated from solid steel, which is a disadvantageous solution from the electromagnetic point of view. The construction is of special interest because in this rotor construction, for instance a blower blade or pump blade can be fixed directly to the rotating rotor yoke, thus producing a fully integrated machine solution. The solid-rotor-core makes it possible to use the motor type also in medium- and in some cases even in high-speed applications. For example, if a single-sided AF rotor is directly integrated into a turbo blower, no extra large friction surfaces are present in the rotor, since the backside of the turbo blower is simply covered by the AF rotor. In such a case, an AFIM might be an attractive solution also at high speeds. As a stand-alone high-speed motor, however, an AF motor is not attractive because two large diameter rotor surfaces are just creating large friction losses. Also the constructional reasons do not favour the use of AFIMs at high speeds, since a high-speed motor should be long and narrow rather than short and thick because of the large disintegrating centrifugal forces of high-speed machines.

The motor construction studied in this thesis should be electromagnetically evaluated using numerical 3D time-stepping field calculations. Computation of the numerical field in 3D gives accurate results, but it is very cumbersome and too expensive for present-day personal computers, and cannot therefore be used in machine design optimization. That is why only some guidelines for designing the AF solid-rotor-core induction motor are given. Most of the results from numerical calculations are however confirmed with measurements.

1.4 Scientific contributions of the work and relevant publications

The thesis introduces an AFIM, which is simple and compact, which endures also high rotation speeds, and which can be conveniently integrated with various moderate-speed power tools. There are no earlier publications related to the structure of the AFIM studied in this thesis. The performance analysis of AFIMs is complicated because of their disc-shape geometry and the saturation effect. A three-dimensional field computation is generally too expensive to predict the performance of AFIMs with high accuracy. However, a few time-harmonic calculations based on 3D FEM were made to find out the flux density distribution in the solid-rotor-core. Additionally, 2D time-stepping FEM was used to study the effects of different parameters on the performance of this type of a motor. The simulation results were compared with the measurement results.

When there is a solid-steel active part in the motor, as there is the solid-rotor-core in the case of the studied AFIM, special attention has to be paid to preventing the penetration of the air-gap harmonic fields into the rotor. These air-gap harmonics generate eddy current losses on the rotor, as is illustrated in Figs. 1.7 and 1.8. The more distorted the air-gap flux density waveform is, the more rotor eddy current losses are created on the rotor. This phenomenon is of significance at high rotational speeds. To prevent the eddy current losses on the rotor, the spatial air-gap flux density distribution should vary as sinusoidally as possible.

In the literature on radial-flux machines, numerous methods have been presented for reducing the harmonic content of the air-gap flux density waveform measured just above the rotor surface. For example, this can be reached by selecting the air-gap length and the number of the stator and the rotor slot combination appropriately. The harmonics contents of the air-gap flux density can also be reduced by the utilization of semi-magnetic slot wedges or special slot opening constructions. Sharma et al. (1996) and Pyrhönen et al. (2002) have provided comprehensive studies of various high-speed solid-rotor designs for radial-flux machines. Peesel (1958) used experimental methods, Chalmers and Woolley (1972) and Pyrhönen (1991a) analytical methods and Saari (1998) and Lähteenmäki (2002) numerical methods in the analysis of the RFIMs equipped with different types of solid-rotor. Eddy current losses can also be reduced with suitable rotor coating. In that case, the rotor will be coated with a layer of electrically well-conducting, non-ferromagnetic material or a ferromagnetic material having a higher resistivity than the rotor core material. Chalmers and Hamdi (1982) and Aho et al. (2006) have studied the effect of the ferromagnetic coating on the rotor surface losses. In this work, these methods have been utilized in the axial-flux motor. The results obtained using these methods on the performance of the AFIM are presented in this work.

The target was to design and build a high-performance AFIM, which can be integrated directly to the working machine. However, a solid-rotor-core AFIM naturally suffers from a low power factor, which leads to large resistive stator losses. Additionally, air-gap harmonics generate eddy current losses in the solid-rotor-core. In this study, the disadvantages of the AFIM were analyzed by numerous laboratory measurements and numerical calculations. It was found out that in addition to the power factor value the length of the air-gap has a significant influence on the power factor value and the rotor eddy current losses of the machine. Because the rotor eddy current losses are the most dominating loss component in the machine, the performance of the one rotor-one stator AFIM can be degraded by selecting too short or long an air-gap length.

The harmonic content on the rotor surface can be decreased effectively by increasing the air-gap length. This causes, however, a low power factor value. The efficiency of the AFIM was increased by decreasing the permeance and winding harmonics by using short-pitch windings in the stator, semi-magnetic slot wedges in the stator slot opening and high-resistivity rotor coating materials. Additionally, the effect of the well-conducting, non-ferromagnetic rotor coating material on the performance of the AFIM was numerically studied. In order to define the influence of these actions on the performance of the AFIM, comprehensive laboratory measurements were carried out. When the same air-gap length was used the efficiency of the prototype machine varied between 0.85 and 0.94 at the nominal point of the motor. The lowest efficiency 0.85 was achieved, when there were no coating on the rotor, the stator slots were open and full-pitch windings were used.

The scientific contribution of the work by the author can be summarized as follows:

- Main design considerations of single-rotor-single-stator AFIM are presented.
- The effects of the air-gap length on the rotor losses and on the performance of an AFIM are analyzed.
- The effects of the rotor teeth and yoke depths on the performance of an AFIM are evaluated.
- The effects of the rotor coating thickness, resistivity, and permeability on the rotor losses and on the performance of an AFIM are analyzed.
- The best possible slotting on the performance of an AFIM is defined.
- A 45 kW prototype motor was manufactured to verify the computations.
- The accuracy of numerical methods in the analysis of an AFIM is verified.

The most relevant publications related to the thesis are:

1. Valtonen, M., Pyrhönen, J., 2005. *Axial-flux solid-rotor induction motor*. Proc. of EEMODS, Heidelberd, Germany, 5-8 September 2005, on CD-ROM.
2. Valtonen, M., Pyrhönen, J., 2005. *Axial-flux solid-rotor induction motor*. Proc. of ISEF, Vigo, Spain, 15-17 September 2005, on CD-ROM.
3. Valtonen, M., Parviainen, A., Pyrhönen, J., 2006. *Electromagnetic field analysis of 3D structure of axial-flux solid-rotor-core induction motor*. Proc. of SPEEDAM, Taormina, Italy, 23-26 May 2006, on CD-ROM.
4. Valtonen, M., Parviainen, A., Pyrhönen, J., 2006. *2D-FEM modelling of an axial-flux solid-rotor-core induction motor*. Proc. of ICEM, Chania, Greece, 2-5 September 2006, on CD-ROM.
5. Valtonen, M., Parviainen, A., Pyrhönen, J., 2006. *Determination of the rotor losses in an inverter supplied axial-flux solid-rotor-core induction motor by using 2D FEM*. Proc. of ICEMS, Nagasaki, Japan, 20-23 November 2006, on CD-ROM.
6. Valtonen, M., Parviainen, A., Pyrhönen, J., 2007. *Inverter switching frequency effects on the rotor losses of an axial-flux solid-rotor-core induction motor*. Proc. of POWERENG, Setúbal, Portugal, 12-14 April 2007, on CD-ROM.
7. Valtonen, M., Parviainen, A., Pyrhönen, J., 2007. *The effects of the number of rotor slots on the performance characteristics of axial-flux solid-rotor-core induction motor*. Proc. of IEMDC. Antalya, Turkey, 3-5 May 2007, on CD-ROM.
8. Parviainen, A., Valtonen, M., 2007. *Influence of stator slot opening configuration to a performance of axial-flux induction motor*. Proc. of ISEF, Prague, Czech Republic, 13-15 September 2007, on CD-ROM.

2. Harmonic losses and numerical modelling of an AF solid-rotor-core IM

The power losses in an electrical machine are divided into mechanical and electrical losses. The mechanical losses include the friction and cooling losses. The electrical losses are divided into fundamental frequency losses, which are winding ohmic losses and core losses, and the harmonic losses. The harmonics – which can vary either in time or in space – in the air-gap flux density, produce deviations in the flux density wave at higher frequencies than the fundamental frequency. The time-dependent harmonics are caused by a non-sinusoidal power supply, while the spatial harmonics are created by the discrete mechanical structure of the machine. In medium- and high-speed solid-rotor-core induction machine applications, rotor losses generated by the induced eddy currents may constitute a majority of the total losses. The harmonic deviation in the air-gap flux density wave causes losses in the solid-rotor-core of the motor; this is because the harmonic waves penetrate into the conducting material and cause eddy currents, which produce ohmic losses in the steel. Figure 2.1 shows the air-gap flux density distribution at the nominal point (T_n = 75 Nm, s_n = 1.0 per cent) of the motor studied. Time-harmonic 3D FEM was applied in the calculations. Thus, the air-gap flux does not include the harmonic components caused by the rotation of the rotor. The Figure clearly illustrates the fact the traditional calculation methods based on the geometric mean radii of the motor will not be very accurate. The flux density distribution in the air-gap is intensified at both ends of the stator. There seems to be a minimum at the average radius of the stator. Such a result emphasizes the importance of three-dimensional analysis of AF motors. In radial-flux solid-rotor machines a similar phenomenon was seen e.g. in the analytical calculation results of Pyrhönen (1991a).

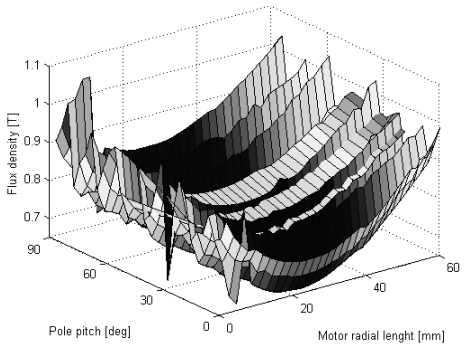

Fig. 2.1 Flux density distribution in the air-gap under load conditions obtained from 3D FEM. The air-gap length of the motor was set at 0.9 mm. The flux density distribution in the air-gap is intensified at inner an outer radii of the stator.

The more complicated geometries and machines, such as AF machines with non-linear magnetic materials, make the use of numerical evaluation techniques unavoidable. Analytical methods are based on many assumptions, although it is possible to improve also them to a certain degree. However, the finite element analysis (FEA) allows modelling of complicated geometries, nonlinearities of the steel, in 2D and in 3D, and gives accurate results without standing on a number of restricting assumptions.

2.1 Development of solution methods of electromagnetic fields in a solid-rotor

Calculation of the magnetic and electric field in the rotor that is manufactured from solid steel is a very demanding process, because the rotor material is magnetically non-linear and the

electromagnetic fields are three-dimensional. The situation is completely different in the case of a conventional laminated squirrel-cage induction motor, in which the magnetic and the electric circuits can be assumed to be separated from each other both in the rotor and in the stator. Thus, the electric circuit is flowing through the coils, and the magnetic circuit is flowing mainly through the steel parts and the air-gap of the machine. The examination of the traditional induction motor can be done in two dimensions because the magnetic circuit is made of laminated electric sheets. Additionally, the non-dominant end effects caused by well-conducting end rings, which are included in the squirrel cage can be studied separately. The standard linear methods that are used in the analysis of conventional induction machines, in which only lumped parameters are considered, cannot be used in the analysis of solid-rotor induction motor. That is because in rotors that are fabricated from solid steel, the steel forms a path for the magnetic flux and for the electric current. Thus, the three-dimensional effects and non-linearity have to be taken into consideration.

It is a demanding task to solve the magnetic and electric fields in a solid-rotor fast and accurately. In theory, it is possible that the rotor field solution can be solved by the 3D FEM calculation; however, it is very time consuming and takes too much time to be used in the practical motor design. Therefore, three-dimensional analytical solution processes have been developed for the rotor fields. It has to be noticed that these analytical calculation methods have been developed for radial-flux machines, and the methods cannot be used directly in the analytical calculations of axial-flux machines. The ultimate simplification, but still a very complicated method, is to solve Maxwell's field equations assuming a smooth rotor and a magnetically linear rotor material.

The research on solid-rotor RFIMs has been intensive from the 1960s to the mid-1980s. Most of the published articles have concentrated on the analytical electromagnetic modelling of the solid-rotor RFIM. For example, Bergmann (1982), Chalmers and Hamdi (1982), and Yee and Wilson (1972) have published very significant results on the analytical modelling. Plenty of research has been done in the field of solid-rotor RFIMs to be able to determine the motor performance with equivalent circuit parameters. Next, it is presented how the development of the analytical methods in the design of solid-rotor RFIM has taken place. However, as was mentioned earlier, these methods cannot be used directly in the analytical design of solid-rotor-core AFIMs.

In the articles, the solid-rotor is supposed to be infinitely long and the rotor material has an ideal rectangular *BH* curve. The assumption of an infinitely long rotor results in a two-dimensional analysis. However, to achieve good accuracy, the end effects have to be taken into consideration. Another assumption is that the rotor material is assumed to be magnetically linear, thus a constant value of 45° is given to the phase angle of the rotor impedance despite the fact that many experimental results have shown that the phase angle of solid steel rotors is far less than 45°.

MacLean (1954), McConnell and Sverdrup (1955), Agarwal (1959), Kesavamurthy and Rajagopalan (1959), Wood and Concordia (1960b), Angst (1962), Jamieson (1968), Rajagopalan and Balarama Murty (1969), Yee and Wilson(1972), Liese (1977) and Riepe (1981a) have used the limiting non-linear theory of the flux penetration into the solid-rotor material. In this theory, it is assumed that the flux density within the material may exist only at the magnitude of the saturation level. Most of these theories, especially Agarwal's theory, seem to be still valid in many analyses, while utilizing the substitute parameters in the

equivalent circuit. Maclean (1954), Chalmers and Woolley (1972), and Yee and Wilson (1972) have applied the assumption of magnetically linear rotor material, that is, the rectangular *BH* curve. This rectangular approximation to the *BH* curve is appropriated only at very high levels of magnetization. This theory gives a constant value of 26.6° for the rotor impedance phase angle. However, based on the experimental results, the rotor impedance is between the values given by the linear and the limiting non-linear theory. The equivalent circuit approach was used by McConnell (1953), Wood and Concordia (1960a), Angst (1962), Dorairaj and Krishnamurthy (1967), Freeman (1968), Sarna and Soni (1972), Chalmers and Saleh (1984), and Sharma et al. (1996). Cullen and Barton (1958) used the concept of wave impedance. Pillai (1969) concluded that the rotor impedance phase angle varies between 35.3° and 45°, while Chalmers and Saleh claimed (1984) that the angle is 30°.

Pipes (1956) presented a transfer-matrix technique for determining the strength of the magnetic and electric field and the current density, which are produced by an external impressed alternating magnetic field in plane-conducting metal plates having a constant permeability. This method was later generalized by Greig and Freeman (1967). This transfer matrix technique calculates the magnetic and electric field strength of the following plane from the values of the previous plane using prevailing material constant. The method is called multi-layer transfer-matrix method (MLTM method). The method was later developed by Freeman and Smith (1970). Freeman published a new version on the technique used in a polar coordinate system. Riepe (1981b), Yamada (1970), Chalmers and Hamdi (1982), and Bergmann (1982) used the MLTM method in the Cartesian coordinate system.

Pyrhönen (1991a) applied the MLTM method in the field calculations of the smooth solid-rotor. The smooth solid-rotor geometry was subdivided into smaller layers in the radial direction and the rotor was also divided axially in slices. The tangential magnetic field strength and the normal magnetic flux density were calculated at the boundary of every region. After the electromagnetic properties were calculated in each layer, they were used as an initial value for the calculation of the following upper layer. Huppunen (2004) developed the MLTM to achieve more accurate calculation results for the solid-rotor machines, especially in the case of axially slotted solid-rotor RFIMs.

2.2 Basic design consideration of the AF solid-rotor-core IM

In the following, some details for designing the one rotor–one stator AF solid-rotor-core induction motor are presented in order to find a proper AF solid-rotor-core construction. The dimensioning is carried out only from the electromagnetic point of view. The mechanical constraints are not taken into account. Figure 2.2 shows the cross-sections of the AFIM studied. In the analytical design of the motor, only the axial component (z-axis is shown in Fig. 2.2) of the flux density is considered. This component, however, is the most effective flux component that affects in the motor.

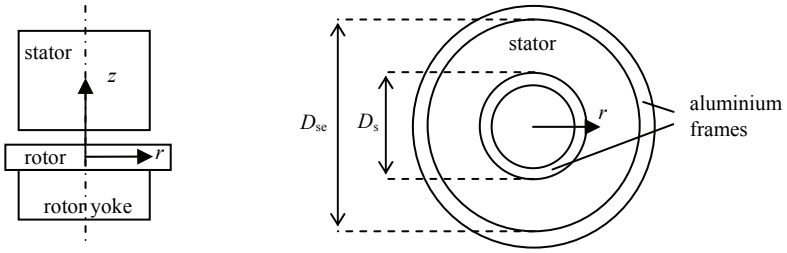

Fig. 2.2 2D views of the motor studied. D_{se} and D_s are the outer and inner diameters of the stator lamination. Also the inner and outer peripheries of the aluminium frame forming the rotor winding end rings are illustrated.

In the dimensioning of the AFIM, the ratio between the inner and outer diameters D_s and D_{se} of the stator is selected as is shown in Fig. 2.2. The ratio can be calculated with

$$K_D = \frac{D_s}{D_{se}}. \tag{2.1}$$

According to Campbell (1974), the optimal diameter ratio for the idealized AFPM machine is 0.58. That value is also used in the design of AFIMs. Also the area of the air-gap S_r (torque producing area) and the length of the stator stack l_e (active length of the motor) can be calculated with the selected diameter values D_{se} and D_s.

The correct rotor size for the torque production can easily be estimated with the tangential tension σ_{tan}. The machine constant C that expresses the magnitude of the internal apparent power S or the power P given by the rotor volume of the machine is an alternative to the tangential stress of the air-gap. According to Vogt (1996) the machine constant can be written for asynchronous machines in the form

$$C = \frac{\pi^2}{\sqrt{2}} k_{w1} A \hat{B}_\delta, \tag{2.2}$$

where A is the linear current density, $\hat{B}_\delta$ is the air-gap peak flux density, and k_{w1} is the winding factor of the fundamental harmonic.

In the case of AF machines, the machine constant (Vogt, 1996) can be written as a function of tangential tension in the form

$$C = \sqrt{2}\sigma_{tan}\pi^2 k_{w1}. \tag{2.3}$$

According to Eqs. (2.2) and (2.3), the tangential tension in the AF machines can be written in the form

$$\sigma_{tan} = A\hat{B}_\delta. \tag{2.4}$$

The next step is to determine the tangential tension value. Vogt (1996) has defined the limiting values for corresponding tangential stress value for asynchronous machine. The tangential tension in the air-gap in the nominal point of the motor can be calculated with

$$\sigma_{\tan} = \frac{T}{R_{\text{av}} S_{\text{r}}}, \tag{2.5}$$

where R_{av} is the geometric mean radius of the motor, S_{r} is the rotor surface facing the air-gap, and T is the torque.

The tangential force $F_{\tan}$ can be calculated with

$$F_{\tan} = \sigma_{\tan} S_{\text{r}}. \tag{2.6}$$

The length of the air-gap δ has to be selected with a special care. When the air-gap length is increased, the stator copper losses will increase, and the eddy current losses on the rotor will decrease. The loss minimum is found between the rising stator copper losses and the diminishing rotor harmonic eddy current losses. Additionally, the air-gap lengthening reduces also the power factor. When a high performance solid-rotor-core AFIM is designed, high air-gap flux density peak values should be used. The high air-gap flux density is a result of a high stator flux density value. The high air-gap flux density should be used to attain the maximum torque.

To get acceptable results by the analytical design calculations, the rotor and the stator cores are divided into a number of concentric circular sub-areas as shown in Fig. 2.3. By this it is assumed that the curve of the machine has no longer an effect on the performance of an individual sub-machine.

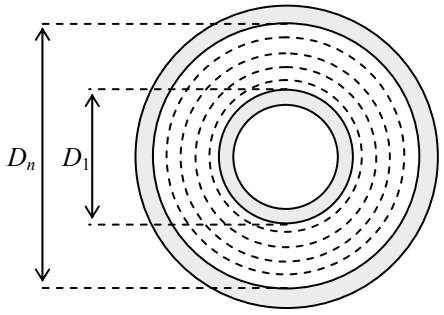

Fig. 2.3 Active region of the motor is divided into concentric areas. D_1 and D_n are the inner and outer diameters of the motor.

The flux density values on the rotor and stator are studied in every area from 1 to n. When the width of the rotor slot b_{r} and rotor slot pitch $\tau_{\text{r}(1\ldots n)}$ are selected, the designer has to take care that the inner parts of the motor will not be saturated. The flux density value on the rotor tooth can be calculated with

$$\hat{B}_{\mathrm{dr}(1\ldots n)} = \frac{\hat{B}_{\delta} \cdot \tau_{\mathrm{r}(1\ldots n)}}{\tau_{\mathrm{r}(1\ldots n)} - b_{\mathrm{r}}}. \tag{2.7}$$

According to Vogt (1996), the permitted flux density of the rotor tooth $\hat{B}_{\mathrm{dr}}$ for radial flux asynchronous machines is 1.5–2.2 T. The same values are used here. The length of the rotor teeth can be calculated by assuming that the teeth of the machine are not saturated, and almost the complete flux of the slot pitch flows along the teeth, and there is no flux in the slots and in the slot insulations

$$w_{\mathrm{dr}} = \frac{\tau_{\mathrm{r}(n)} \cdot \hat{B}_{\delta}}{\hat{B}_{\mathrm{dr}(n)}}. \tag{2.8}$$

With the analytical methods, the depth of the rotor yoke can be calculated with

$$w_{\mathrm{yr}} = \frac{\hat{\Phi}}{2 \cdot \hat{B}_{\mathrm{yr}} \cdot k_{\mathrm{rFe}} \cdot l_{\mathrm{e}}}, \tag{2.9}$$

where $\hat{B}_{\mathrm{yr}}$ is the flux density peak of the rotor yoke, the space coefficient of rotor iron k_{rFe} depends on the relative thickness of the insulation of the electric sheet and on the press fit of the stack, and $\hat{\Phi}$ is the peak value for the main flux penetrating the winding in the stator and in the rotor.

According to Vogt (1996), the permitted flux density of the rotor yoke $\hat{B}_{\mathrm{yr}}$ for radial flux asynchronous machines is 0.4–1.6 T. The mechanical strength of the solid-rotor-core is not a problem contrary to laminated rotors, where the mechanical constraints may thus determine the minimum depth of the rotor yoke.

Correspondingly, Equations (2.7)–(2.9) can also be used for dimensioning the stator core. However, in the case of the studied AF solid-rotor-core induction motor, the flux density values in the stator and in the air-gap should be high to achieve proper characteristics of the motor. Later, it is discussed how to decrease the eddy current losses caused by harmonic components in the air-gap flux density on the rotor surface.

The DC resistance of the stator phase winding at room temperature can be determined by

$$R_{\mathrm{s(DC)}} = \frac{N l_{\mathrm{m}}}{\sigma \cdot a \cdot S_{\mathrm{c}}}, \tag{2.10}$$

where a is the number of parallel conductors, l_{m} is the length of one turn of the winding, N is the number of the turns in series in the stator winding per phase, S_{c} is the cross-section of one conductor, and σ is the conductivity of the winding material.

According Vogt (1996), the length of the coil depends on the stator core length l_e, pole pitch τ_p, chord factor χ which is the ratio between the coil span W to the pole pitch τ_p, and the average distance of the coil turn-end l_{ew}

$$l_m = p \cdot \left(2 \cdot l_e + \chi \tau_{pin} + \chi \tau_{pout} + 2 \cdot l_{ew}\right). \tag{2.11}$$

Equation (2.11) can be used directly, when the length of the coil is determined for an AF machine.

The end winding leakage flux is the result of all the currents flowing in the end windings. An accurate determination of the end winding leakage inductance is very difficult, because the geometry of the end windings is usually difficult to analyze, and further, all the phases of poly-phase machines influence the occurrence of a leakage flux. The end windings are relatively far from the iron parts, and thus the end winding inductances are not very high. Therefore, it is sufficient to employ empirically determined inductance factors λ_E and λ_W. Richter (1954) presents in detail calculated values of inductance factors that are valid for asynchronous machines. In the case of AF machines, the end winding leakage inductances have to be calculated in the outer and inner circumferences. The end winding leakage inductances L_w in the outer and inner circumferences can be calculated as

$$L_{wsin} = \frac{4 \cdot m}{Q_s} q \cdot N^2 \cdot \pi \cdot f \cdot \mu_0 \left(2 \cdot l_{ew} \cdot \lambda_E + \chi \cdot \tau_{pin} \cdot \lambda_W\right), \tag{2.12}$$

$$L_{wsout} = \frac{4 \cdot m}{Q_s} q \cdot N^2 \cdot \pi \cdot f \cdot \mu_0 \left(2 \cdot l_{ew} \cdot \lambda_E + \chi \cdot \tau_{pout} \cdot \lambda_W\right), \tag{2.13}$$

where f is the frequency, q is the number of slots per pole and per phase, and μ_0 is the permeability of vacuum.

The detailed design process of an AFIM is presented in Appendix A. As an example, Appendix B presents the calculated geometric mean radii for a 100 kW AFIM.

2.3 Harmonic losses on a rotor

The harmonics generate remarkable losses in a solid-rotor, as was shown in Fig. 1.7. The air-gap flux density can be distorted even though the supplied phase voltage were sinusoidal, that is, the discrete stator windings and the reduction in the magnetic flux density under the stator slot opening cause harmonics in the air-gap flux density. The major causes of eddy currents can be categorized into the following three groups: winding harmonics are caused by the discrete coil distribution in the periphery of the stator yoke, the permeance harmonics are caused by the slot openings, and finally, if the winding harmonics and the permeance harmonics are of the same order, the particular harmonic is called the slot harmonic. The effects of these harmonics in asynchronous motors have been examined for instance by Gibbs (1947), Agarwal (1960), Stoll and Hammond (1965), Bergmann (1982), Pyrhönen and Kurronen (1994) and Huppunen (2004).

2.3.1 Permeance harmonics

There are two main causes of harmonics in the air-gap flux density distribution of the machine when a sinusoidal supply is used. These are the permeance harmonics and the winding harmonics. When studying the permeance harmonics, we may observe the flux density distribution $B(\alpha)$ on the rotor surface over one slot pitch τ_s as is shown in Fig. 2.4. Under a tooth, the magnetic flux density has a constant value, but the flux density drops under the effective slot width b_{so}'. The effective elongation of the air-gap δ was examined by Carter more than hundred years ago, and its effect is normally taken into account by using the factor k_C (Carter, 1901). The equivalent air-gap δ_e is written as a function of the real air-gap δ

$$\delta_e = k_C \delta . \tag{2.14}$$

Equivalent formulae are given to express the magnetic flux density under one stator slot pitch e.g. by Heller and Hamata (1977). The origin of the co-ordinates is fixed at the midpoint of one tooth, and the Heller-Hamata equations for a stator with Q_s slots and stator bore diameter D_s are

$$\begin{cases} B(\alpha) = B_{max}\left(1-\beta_1-\beta_1\cos\left(\dfrac{\pi D_s}{1.6b_{so}}\left(\alpha-\dfrac{2\pi}{2Q_s}\right)\right)\right), & \dfrac{\pi}{Q_s}-\dfrac{1.6b_{so}}{D_s} < \alpha < \dfrac{\pi}{Q_s}+\dfrac{1.6b_{so}}{D_s} \\ B(\alpha) = B_{max}, & \text{elsewhere} \end{cases} , \tag{2.15}$$

where α is the mechanical angle, which starts in the middle of a stator tooth, varying from $2\pi/Q_s$.

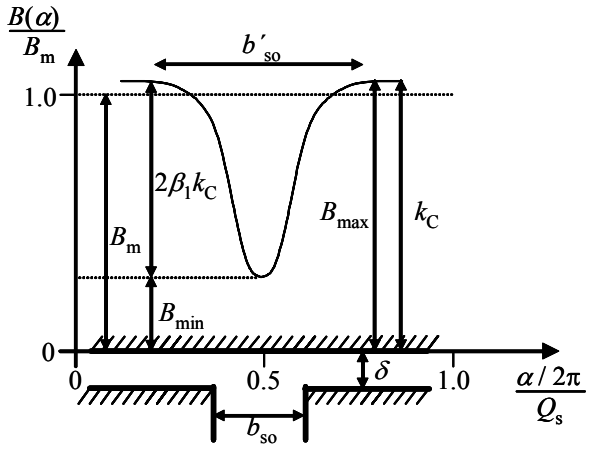

Fig. 2.4 Flux density distribution $B(\alpha)$ on a surface of the rotor above one stator slot.

Equation (2.15) can be replaced with high accuracy by the following Fourier-series representation (Bergmann, 1982)

$$B(\alpha) = B_{\mathrm{m}}\left(1 - \sum_{k=1}^{\infty}(-1)^k \beta_1 k_{\mathrm{C}} a_{1k} \cos(kQ_s\alpha)\right), \tag{2.16}$$

where

$$a_{1k} = \frac{2\sin\left(\frac{k\pi b_{\mathrm{so}}'}{\tau_{\mathrm{s}}}\right)}{k\pi\left(1 - \left(\frac{kb_{\mathrm{so}}'}{\tau_{\mathrm{s}}}\right)^2\right)}, \tag{2.17}$$

$$\beta_1 = \frac{(B_{\max} - B_{\min})}{2B_{\max}} = \frac{1 + u^2 - 2u}{2(1 + u^2)}, \tag{2.18}$$

$$u = \frac{b_{\mathrm{so}}}{2\delta} + \sqrt{1 + \left(\frac{b_{\mathrm{so}}}{2\delta}\right)^2}, \tag{2.19}$$

$$b_{\mathrm{so}}' = \frac{\gamma\delta}{\beta_1}; \qquad \gamma \approx \frac{(b_{\mathrm{so}}/\delta)^2}{5 + (b_{\mathrm{so}}/\delta)}, \tag{2.20}$$

$$k_{\mathrm{C}} = \frac{\tau_{\mathrm{s}}}{\tau_{\mathrm{s}} - \beta\, b_{\mathrm{so}}'} = \frac{B_{\max}}{B_{\mathrm{m}}}. \tag{2.21}$$

Equations (2.17)–(2.21) are given by Richter (1967). These equations are developed for RF machines. In the case of AF machines, the tooth width increases with increasing of the core diameter. Thus, the calculations have to be repeated in every sub-area shown in Fig. 2.3.

Since the harmonics are very much dependent on the flux density variation: according to Equations (2.16)–(2.21), there are several methods for reducing the harmonic amplitudes at the rotor surface. These methods are: making the stator slot opening as small as possible, increasing the air-gap length, modifying the shape of the slot opening, and using a semi-magnetic slot-wedge.

According to Equations (2.18) and (2.19), the increase of the air-gap length reduces flux fluctuations on the rotor surface, but also increases the magnetizing current and simultaneously deteriorates the power factor. In solid-rotor-core induction motors, the air-gap length plays a very important role when the flux harmonics in the surface of the rotor are studied. If the air-gap length is increased, the flux distribution will smoothen on the rotor surface. However, a longer air-gap length increases the magnetizing current of the motor, and thus the stator copper losses will increase. The loss minimum is found between the rising stator copper losses and the diminishing rotor harmonic eddy current losses. The flux distribution can be smoothened by making the stator slot opening as small as possible. The

minimum size of a standard motor slot opening is mainly determined by the winding manufacturing criteria. Another limit is the value of the stator leakage inductance, because too narrow a slot opening somewhat increases it.

Additionally, the modified stator slot opening geometry and a semi-magnetic wedge can be used so that the permeance harmonics in the air-gap flux are minimized. Flux plots under a traditional stator slot opening and a modified slot opening (¼ part of a circle nodule on both sides of the slot opening) are presented by Pyrhönen and Kurronen (1991b). It is shown that the magnetic flux density distribution under one slot pitch is far more uniform with the modified stator slot compared with that of the normal slot opening. These nodules guide the flux under the slot opening and thus reduce the flux dip depth. The shape of the little nodes on both sides of the slot opening in a modified slot has to be quite accurate and would probably be very difficult to manufacture mechanically. The magnetically most effective way to eliminate the permeance harmonics is to use a semi-magnetic wedge as a slot lock. The purpose of the slot-wedge is to lead the flux under the slot opening. The semi-magnetic wedge is usually manufactured from the material with a low relative permeability, usually $\mu_r \in [2, 5]$. The power factor of the machine and the harmonic losses on the rotor surface can be optimized by choosing a suitable slot-wedge material and the form of the wedge. Increasing the permeability of the slot-wedge flattens the permeance function, but also increases the slot leakage flux. Pyrhönen and Kurronen (1991b) have shown the effect of the slot-wedges compared with a normal slot opening. The drawback of this method is the manufacturing of a long stick with a rather accurate form. Of course, this is not a problem in the case of AF machines. Also it is possible to employ totally enclosed slot openings, but such a slot configuration is not a practical solution (Parviainen and Valtonen, 2007).

2.3.2 Winding harmonics

In addition to permeance harmonics, there are also winding harmonics, because the windings of induction machines are placed in stator slots and cannot thus be spread smoothly over the stator inner surface. The travelling velocity of the fundamental current linkage wave in the stator surface is faster than the velocities of the harmonic current linkages. The ordinal of the stator harmonic ν for an m_s-phase stator winding is given by Richter (1954)

$$\nu = 2gm_s + 1, \tag{2.22}$$

where g is any positive or negative integer.

The harmonics of positive order (ν is positive) rotate in the same direction as the fundamental wave, and the harmonics of negative order (ν is negative) in the opposite direction with respect to the fundamental current linkage wave. The angular frequency of the harmonic ν with respect to the stator is

$$\omega_{\nu s} = \frac{\omega_s}{\nu}. \tag{2.23}$$

The harmonic field induces voltages in the stator that have the same angular velocity as the fundamental wave. The number of the pole pairs of the harmonics is

$$p_\nu = \nu p \,. \tag{2.24}$$

The pole pitch $\tau_{\mathrm{p}\nu}$ of the harmonic compared to the pole pitch τ_{p} of the fundamental is

$$\tau_{\mathrm{p}\nu} = \frac{\tau_{\mathrm{p}}}{\nu} \,. \tag{2.25}$$

The amplitudes of the current linkages $\hat{\Theta}_\nu$ can be found with the stator winding factor k_{w} (Vogt 1983)

$$\hat{\Theta}_\nu = \hat{\Theta}_1 \frac{k_{\mathrm{w}\nu}}{k_{\mathrm{w}1}\nu} \,, \tag{2.26}$$

where

$$k_{\mathrm{w}\nu} = \frac{2\sin\left(\nu\dfrac{W}{\tau_{\mathrm{p}}}\dfrac{\pi}{2}\right)\sin\dfrac{\nu\pi}{2m_{\mathrm{s}}}}{\dfrac{Q_{\mathrm{s}}}{m_{\mathrm{s}}p}\sin\dfrac{\nu\pi p}{Q_{\mathrm{s}}}} \,, \tag{2.27}$$

where W is the coil span (width).

Figure 2.5 describes the difference between the three different three-phase windings; a single-layer winding, for which $W/\tau_{\mathrm{p}} = 1$ and two two-layer windings, for which $W/\tau_{\mathrm{p}} = 8/9$ and $W/\tau_{\mathrm{p}} = 7/9$. The comparison is made for the four-pole machine studied.

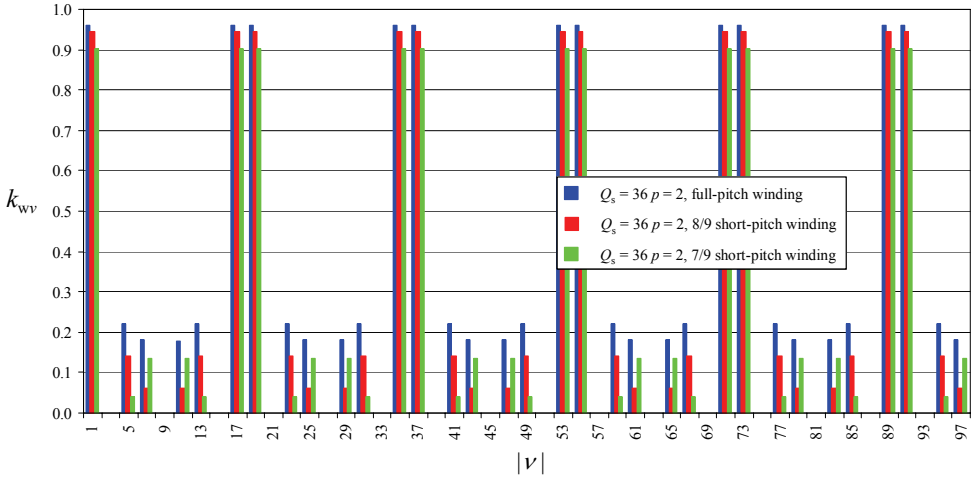

Fig. 2.5 Winding factors with different windings. $Q_{\mathrm{s}} = 36$, $m_{\mathrm{s}} = 3$, $q = 3$.

As it can be seen in Fig. 2.5, using a two-layer winding, for which w_s/τ_p = 8/9 or 7/9 reduces the values of the winding factors of the harmonics and unfortunately also the winding factor of the fundamental. Two-layer windings have not usually been used in small machines, but they could be a good way to reduce the effect of the harmonics, even though they are significantly more laborious to manufacture than single-layer windings. In short-pitch windings the end-winding length is decreased remarkably, and hence, despite of the small weakening of the fundamental winding factor, the material cost of the winding may be decreased, respectively. Actually, the ratio W/τ_p =7/9 happens to be the best one in this case, since it gives the minimum value for the leakage factor (Vogt, 1983) that is determined by

$$\sigma_\delta = \sum_{\nu \neq 1} \left(\frac{k_{w\nu}}{\nu k_{w1}} \right)^2 . \tag{2.28}$$

Both the permeance harmonic losses and the winding harmonic losses can also be reduced by decreasing the effects of the air-gap harmonics on the conducting medium. By increasing the air-gap length, the effects of the winding harmonics on the rotor surface can be reduced to an acceptable level. Another method to decrease the eddy current in a conducting medium is to use high resistivity or high conductivity materials on the surface of the conducting medium. The effects of the high resistivity rotor coating material and the air-gap length on the performance of the studied AFIM are presented in Chapters 3 and 4. The design of the stator slot opening, however, is also of significant importance.

2.3.3 Frequency converter induced rotor losses

The converter supply causes, however, some new problems. The supply voltage is strongly non-sinusoidal causing additional losses in the conductors and the iron core. The noise level of the motor is increased, and there may be pulsations in the torque. The requirement imposed on a motor by a converter supply should be taken into account in the design, and analysis methods capable of modelling these new effects are needed.

Conventional calculation methods rely on the assumption of sinusoidal time-variation. They are not directly applicable to the analysis of motors supplied by static frequency converters. The development of the numerical methods and the growth of computer capacities have made it possible to solve more and more involved magnetic field problems, and the finite element method, in particular, has proven to be efficient when dealing with complicated geometries.

The solid-rotor-core of the AFIM is very sensitive to the air-gap harmonic contents. To avoid excessive rotor losses, the harmonics of the air-gap flux density should be minimized. The harmonic content of the flux density can be avoided with an accurate motor design; however, the supply current should also be as sinusoidal as possible. Voltage source converters are using pulse width modulation (PWM) technology to produce the supply voltage to the motor. Lähteenmäki (2002) used the square-wave frequency converter output and showed that in direct PWM inverter supply, the frequency modulation index (f_{sw}/f_s) should be at least 21 to achieve a situation in which the motor losses remain lower than in the square-wave supply. Thus, in the 200 Hz motor drive studied, the switching frequency should be at least 4200 Hz to meet this condition. Square-wave inverter output remarkably reduces the converter losses and is, from this point of view, a preferable choice at rated speed operation in pump and fan applications.

Bamuner (2006) has investigated the effects of the inverter switching frequency on the losses of a solid-rotor-core AFIM. The motor was a single-sided four-pole aluminium-cage AFIM, and the nominal power and the rotation speed of the motor were 11 kW and 7200 min^{-1}. The rotor core material was Fe52. The motor was fed by ABB SAMI-GS frequency converter (ACS501). Figure 2.6 shows the rotor losses as a function of switching frequency at no-load.

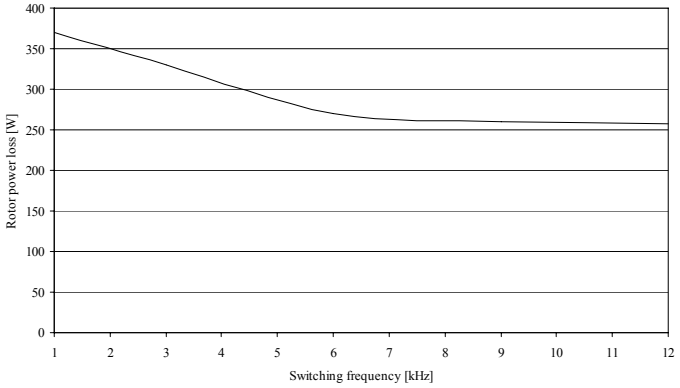

Fig. 2.6 Rotor power loss as a function of switching frequency at no-load. Inverter output frequency was 240 Hz. The switching frequency higher than 5 or 6 kHz the rotor losses can be considered constant with the switching frequency in the case of studied motor (Bamuner, 2006).

The transient inductance of the low-voltage, medium- and high-speed motors is typically lower than in conventional 50 Hz machines, that is, the number of turns per phase in the stator windings of such a motor is very low. The air-gap length and the rotor surface saturation decrease the transient inductance even more. Because of the low-transient inductance, the stator current in the PWM-modulated supply voltage rapidly follows the voltage level changes. Additionally, stator current ripple may be high despite the high frequency modulation index.

The switching frequency range in typical present-day frequency converters may vary between 1.5 kHz and 4.0 kHz without decreasing the rated output power of the converter. When high supply frequencies are needed, and the frequency modulation index is lower than 21, the output voltage of the inverter should be filtered. The inductor inductance value of an *LC* filter is typically selected to be half of the stator leakage inductance value. The capacitor of the *LC* filter is selected to compensate 80 per cent of the no-load current. These values typically produce suitable resonance frequencies for the filter (Huppunen and Pyrhönen, 1997).

The 45 kW, 6000 min^{-1} prototype machines were tested with both a direct inverter supply and with a sine wave filter installed between the inverter and the machine. The filter provides almost sinusoidal waveforms for the motor currents also in an inverter supply. Thus, the characteristics of the test machine may be assumed to be measured at sinusoidal supply. The motor voltage and current waveforms are shown in Figs. 2.7 and 2.8 with an inverter supply using 4 kHz switching frequency without any filtering and with a filtered supply.

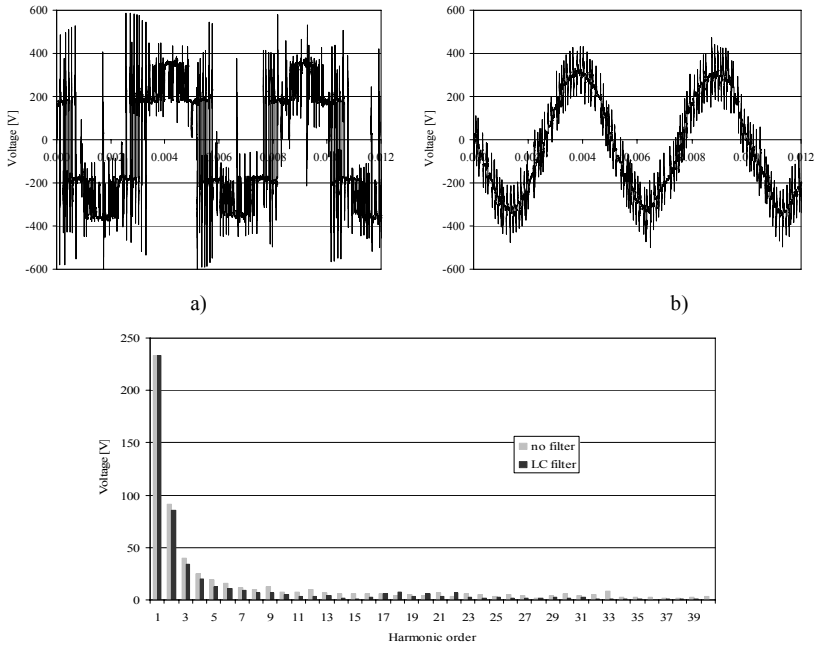

Fig. 2.7 Voltage waveforms of the studied 45 kW, 6000 min^{-1} solid-rotor-core induction motor as a function of time with a) 4.0 kHz switching frequency without filter and b) with a filtered output, at the nominal point 75 Nm of the motor. Figure c) illustrates the fundamental wave and the spectra of the RMS voltage values.

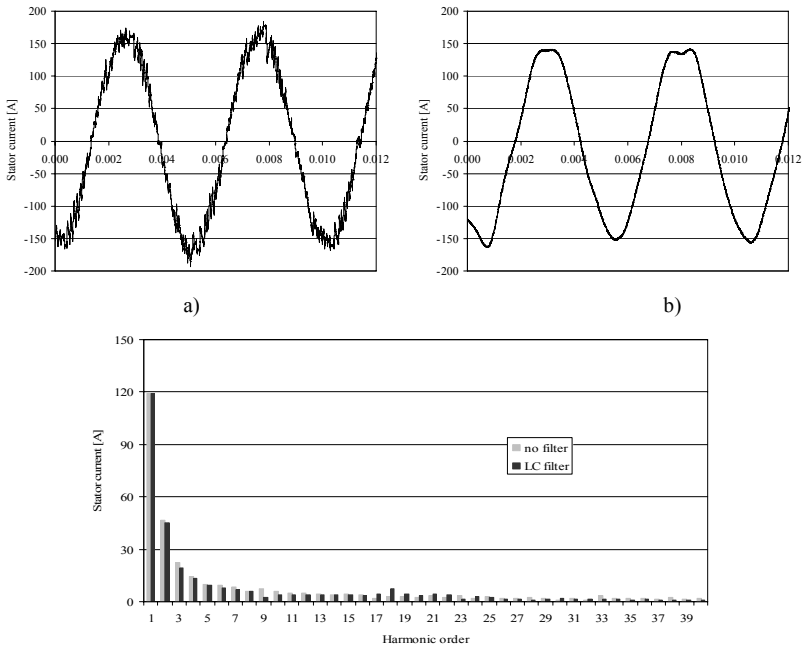

Fig. 2.8 Loaded current waveforms of the studied 45 kW, 6000 min^{-1} solid-rotor-core induction motor as a function of time with a) the switching frequency is 4.0 kHz and b) filtered output current, at the nominal point 75 Nm of the motor. Figure c) illustrates the fundamental wave and the spectra of the stator RMS current values.

Figure 2.9 shows the slip, efficiency, fundamental RMS voltage and fundamental RMS current with an inverter supply using 4.0 kHz switching frequency and with a filtered supply at the nominal point (T = 75 Nm) of the motor.

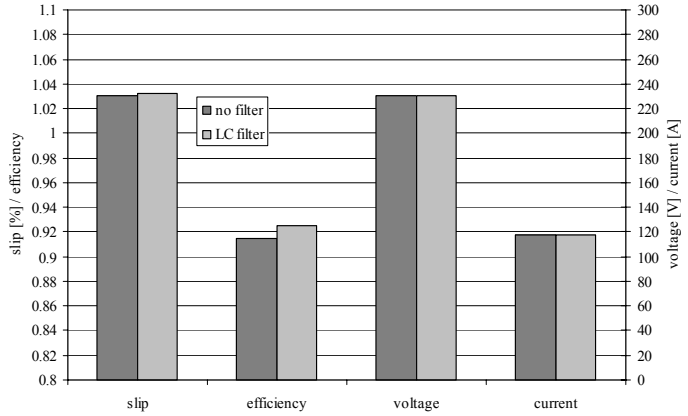

Fig. 2.9 Slip, efficiency, RMS phase voltage and RMS phase current with an inverter supply using 4.0 kHz switching frequency and with a filtered supply at the point of motor nominal torque of 75 Nm.

When a 4.0 kHz switching frequency direct inverter supply and an inverter supply with an *LC* filter are compared, at the nominal point, the efficiency of the motor is approximately one per cent unit higher. There are no considerable differences in the slip, voltage and current when non-filtered and filtered supplies are used. Because the motor additional loss occurs mainly in the surface of the rotor shown in Chapter 3, the inverter supply has a significant effect on the loss performance of the motor.

When the frequency converter supply is used, the voltage contains different harmonic frequencies, because of the power stage switching operation. The harmonic that rotates in the same direction as the main flux creates a positive torque, while the harmonic that rotates in the opposite direction creates a negative torque, and finally, the harmonic that produces non-rotating current linkages has no effect on the torque.

The harmonic frequencies have a disadvantageous effect on the machine losses. The iron losses are increased, because harmonic voltages increase the saturation of the magnetic path. The harmonic frequencies have no significant effect on the stator copper losses, because the skin effect is negligible in a small-diameter round-wire.

2.4 Electromagnetic problem description

Nowadays, the computers are faster than ever and capable of processing a large amount of data. As a result of the development of computer technology, the finite element method has become a common tool, when electrical motors are designed and calculated with steady-state and transient methods. However, the accurate modelling of the motors is still a time-consuming process, especially in cases where a three-dimensional solution is required. That is because the increasing demand for the performance calls for more reliable results, more accurate models, and shorter time steps in dynamic simulation. In the case of radial flux motors, 2D modelling is often accurate enough, especially if the motor is long and the end effects in the motor can be taken into account with a circuit equation. In axial-flux machines, many parameters change as a function of the rotor radius. 3D modelling is needed in the field

calculations of the axial-flux machines, regardless of the fact that the accurate 3D model calculation and modelling require plenty of time. In some occasions, the average torque of an axial-flux machine may, however, be calculated using the simplified 2D model.

The electromagnetic problem description of solid-rotor-core induction motor is based on solving the set of partial differential equations obtained from Maxwell's equation. Usually the problem is assumed to be quasi-static, that is, the displacement current term is neglected. In the case of a quasi-static problem, the electromagnetic radiation and associated wave phenomena are not taken into account. This is a valid assumption, because the dimensions of the modelled induction motor are small compared with the wavelength of the electromagnetic wave.

In non-saturated cases, it is possible to solve eddy current problems with analytical methods, if the geometry of the studied device is simple. In the case of complex geometries, it is not possible to use an analytical solution. In numerical methods, the problems are simplified by describing the magnetic field in terms of differential potential functions. Eddy currents cause the curl of the magnetic field to be non-zero and therefore, a scalar potential serving as a full solution cannot be defined, because there is no scalar field that represents a complete solution. In order to solve the eddy current problem, at least one component of a vector field has to be solved.

Generally, there is an eddy current problem when a metal conductor is inserted in a variable magnetic field, or when a metal conductor is in motion in a constant field. In these cases, as a consequence of the generation of electric currents, there occurs a phenomenon known as eddy currents. Eddy currents have negative effects for instance on the transformer cores. These effects may be reduced by using a thin lamination, which increases the corresponding eddy current resistance thereby limiting the heating by Joule effects of eddy currents. Eddy currents have a positive effect for instance in the induction heating.

The eddy current problem can be described mathematically by using various potential formulations (Steele, 1987). In this work, the electromagnetic problem is described with two different potential formulations, depending on whether the problem is solved in two- or three-dimensions. In 2D, the problem is formulated using a magnetic vector potential $\boldsymbol{A}$ and an electric scalar potential ϕ, while in 3D, the problem is formulated using an electric vector potential $\boldsymbol{T}$ and a magnetic scalar potential ψ.

2.4.1 Model of a 2D eddy current problem

Under time-varying conditions, it is necessary to construct an electromagnetic model, in which the electric field vectors $\boldsymbol{E}$ and $\boldsymbol{D}$ are appropriately related to the magnetic field vectors $\boldsymbol{B}$ and $\boldsymbol{H}$. The connection between the electric field strength $\boldsymbol{E}$ and the magnetic flux density $\boldsymbol{B}$ is determined by Faraday's law

$$\nabla \times \boldsymbol{E} = -\frac{\partial \boldsymbol{B}}{\partial t}. \tag{2.29}$$

Equation (2.29) describes how a changing magnetic flux creates an electric field around it. Ampere's law relates magnetic field strength $\boldsymbol{H}$ with the electrical current density $\boldsymbol{J}$ and the electric flux density

$$\nabla \times \boldsymbol{H} = \boldsymbol{J} + \frac{\partial \boldsymbol{D}}{\partial t}. \tag{2.30}$$

Equation (2.30) indicates that a time-varying electric-field will give rise to a magnetic field, even in the absence of a free current flow. In order to be consistent with the equation of continuity in a time-varying situation, both of the curl equations (2.29) and (2.30) must be generalized.

A divergence relation between the electric field $\boldsymbol{D}$ and the distribution of free charges can be expressed with the equation

$$\nabla \cdot \boldsymbol{D} = \rho . \tag{2.31}$$

Equation (2.31) is known as Gauss's law. Gauss's law for magnetic fields is described with the equation

$$\nabla \cdot \boldsymbol{B} = 0 . \tag{2.32}$$

Equations (2.31) and (2.32) show that the divergence of $\boldsymbol{D}$ is charge density ρ and the divergence of $\boldsymbol{B}$ is zero, i.e. $\boldsymbol{B}$ has no source and $\boldsymbol{D}$ has the source and the drain.

In the eddy current problem, the time variation of the magnetic field induces an electric field, which causes the electric current to flow in the conducting medium. These currents affect the magnetic field. The displacement currents can be neglected in the eddy current problem, which makes the eddy current problem easier to solve than the dynamic problem. It can be shown that for all practical frequencies and for the conductivities of all core metals in rotating electrical machines, the displacement current is notably smaller than the conduction current. That is, the eddy current problems are quasi-static problems.

The latter part of Equation (2.30) representing Maxwell's displacement current can be omitted because the problem is assumed to be quasi-static. The term quasi-static indicates that the frequency of the phenomena is low thus keeping Maxwell's displacement current insignificant. The quasi-static case differs from the fully dynamic case only by neglecting of the displacement current. The phenomena occurring in electric machines meet well the quasi-static requirement, since, in practice, considerable Maxwell's displacement currents appear only at radio frequencies and in devices, such as capacitors, optimized for displacement currents.

In addition, the material equations are needed. By applying permittivity ε, permeability μ and conductivity σ, materials can be describe with the equations

$$\boldsymbol{D} = \varepsilon \boldsymbol{E} , \tag{2.33}$$

$$\boldsymbol{B} = \mu \boldsymbol{H} , \tag{2.34}$$

$$\boldsymbol{J} = \sigma \boldsymbol{E} . \tag{2.35}$$

The magnetic field of electric machines can often be treated as a two-dimensional case, and thus the magnetic vector potential is employed in the numerical solution of the field. However, in many cases, the fields of the machine are clearly three-dimensional, and thus a two-dimensional solution is always an approximate. A two-dimensional eddy current problem can be formulated in terms of magnetic vector potential $\boldsymbol{A}$, from which all other field variables of interests can be derived. The magnetic vector potential is defined as a vector such that the magnetic flux density $\boldsymbol{B}$ is its curl

$$\boldsymbol{B} = \nabla \times \boldsymbol{A} . \tag{2.36}$$

Equation (2.36) does not define the magnetic vector potential, because the curl of the gradient of any function is equal to zero. This means that any arbitrary gradient of a scalar function can be added to the magnetic vector potential, Equation (2.36) still being correct. The uniqueness of Equation (2.36) is ensured by using Coulomb's gauge, stating that the divergence of the magnetic vector potential is zero everywhere in the space studied (Bîrô and Preis, 1989)

$$\nabla \cdot \boldsymbol{A} = 0 . \tag{2.37}$$

Substituting the definition for magnetic vector potential (2.36) to the induction law (2.29) yields

$$\nabla \times \boldsymbol{E} = -\nabla \times \frac{\partial}{\partial t} \boldsymbol{A} . \tag{2.38}$$

Writing Faraday's law in terms of $\boldsymbol{A}$ and solving $\boldsymbol{E}$ yields

$$\boldsymbol{E} = -\frac{\partial \boldsymbol{A}}{\partial t} - \nabla \phi , \tag{2.39}$$

where ϕ is the electric scalar potential.

Adding a scalar potential causes no problems with the induction law, because $\nabla \times \nabla \phi \equiv 0$. The equation shows that the electric field strength vector consists of two parts. The reduced scalar potential ϕ describes the non-rotational part of the electric field strength, and the non-rotational part is due to electric charge and polarization of dielectric material.

Current density depends on the electric field strength

$$\boldsymbol{J} = \sigma \boldsymbol{E} = -\sigma \frac{\partial \boldsymbol{A}}{\partial t} - \sigma \nabla \phi . \tag{2.40}$$

Ampere's law and the determination of the vector potential give

$$\nabla \times \left(\frac{1}{\mu} \nabla \times \boldsymbol{A} \right) = \boldsymbol{J} . \tag{2.41}$$

Substituting (2.40) and (2.41) gives

$$\nabla \times \left(\frac{1}{\mu} \nabla \times \boldsymbol{A} \right) + \sigma \frac{\partial \boldsymbol{A}}{\partial t} + \sigma \nabla \phi = 0 \,. \tag{2.42}$$

Equation (2.42) is valid at eddy current regions, whereas Equation (2.41) is valid in areas with the source currents $\boldsymbol{J} = \boldsymbol{J}_s$, that is, the winding currents, and in the regions with no current densities at all $\boldsymbol{J} = 0$.

In two-dimensional cases, the solution may be based on a single component of a vector potential $\boldsymbol{A}$, where the field is computed in the Cartesian xy plane. The field solution ($\boldsymbol{B}$, $\boldsymbol{H}$) is found at xy plane, while $\boldsymbol{J}$, $\boldsymbol{A}$ and $\boldsymbol{E}$ are all in z-direction. Since $\boldsymbol{J}$ and $\boldsymbol{A}$ are in z-direction, the gradient $\nabla \phi$ has only a z-component, and (2.40) is valid. The scalar potential is thus independent of the x- and y-components. ϕ could be a linear function of the z-coordinate, since a two-dimensional field solution is independent of z. The assumption of two-dimensionality is not valid if potential differences caused by electric charges or by the polarization of insulators exist. In two-dimensional eddy current problems, the scalar potential must be set zero $\phi = 0$ (Silvester and Ferrari, 1990).

In a two-dimensional case (2.42) becomes

$$-\nabla \times \left(\frac{1}{\mu} \nabla A_z \right) + \sigma \frac{\partial A_z}{\partial t} = 0 \,. \tag{2.43}$$

Outside eddy currents regions the following is valid

$$-\nabla \cdot \left(\frac{1}{\mu} \nabla A_z \right) = J_z \,. \tag{2.44}$$

In these cases, the source current density is sinusoidal in time with an angular frequency ω. If the material is linear, also the magnetic vector potential varies sinusoidally in time in steady-state conditions. In that case, the solution can be greatly simplified. However, this is not the case in the studied motor, because the stator and rotor are manufactured from ferromagnetic materials.

2.4.2 Model of a 3D eddy current problem

In three-dimensional eddy current problems, the fields in conducting regions must be represented by a vector, such as $\boldsymbol{E}$ and $\boldsymbol{H}$. In non-conducting regions, however, the electromagnetic field can be represented by a scalar variable. This is more efficient than to use vectors everywhere (Webb and Forghani, 1990). In this work, the $\boldsymbol{T}$-ψ method (Webb and Forghani, 1990; Webb and Forghani, 1995) is used to solve the 3D eddy current problem. In the $\boldsymbol{T}$-ψ method, the magnetic field is split into the gradient of a scalar potential ψ and a rotational part $\boldsymbol{T}$ (Carpenter, 1977; Albanese and Rubinacci, 1988). The different equations to be solved, where $\boldsymbol{J}_s$ is the source current density, are

$$-\nabla\times\frac{1}{\sigma}\nabla\times\boldsymbol{H}-\frac{\partial}{\partial t}(\mu\boldsymbol{H})=0\,, \tag{2.45}$$

$$\nabla\times\boldsymbol{H}=\boldsymbol{J}_{\mathrm{s}}\,, \tag{2.46}$$

$$\nabla\cdot\mu\boldsymbol{H}=0\,. \tag{2.47}$$

Equation (2.45) is solved in the conducting regions, while Equations (2.46) and (2.47) are solved in the non-conducting regions. In the conducting region, the current density is written as

$$\boldsymbol{J}=\nabla\times(\boldsymbol{T}+\boldsymbol{T}_0), \tag{2.48}$$

where $\boldsymbol{T}$ is the unknown vector potential and $\boldsymbol{T}_0$ is the impressed vector potential describing an arbitrary current distribution with its net current equal to the prescribed value.

In the conducting and non-conducting regions, the magnetic field strength can be written in the form

$$\boldsymbol{H}=\boldsymbol{T}+\boldsymbol{T}_0-\nabla\psi\,, \tag{2.49}$$

$$\boldsymbol{H}=\boldsymbol{T}_0-\nabla\psi\,. \tag{2.50}$$

By adding Equations (2.49) and (2.50) to Equations (2.45) and (2.47), the following partial differential equations are obtained

$$\nabla\times\left(\frac{1}{\sigma}\nabla\times\boldsymbol{T}\right)-\nabla\left(\frac{1}{\sigma}\nabla\cdot\boldsymbol{T}\right)+\frac{\partial}{\partial t}(\mu\boldsymbol{T})-\frac{\partial}{\partial t}(\mu\nabla\psi)=-\nabla\times\left(\frac{1}{\sigma}\nabla\times\boldsymbol{T}_0\right)-\frac{\partial}{\partial t}(\mu\boldsymbol{T}_0). \tag{2.51}$$

$$\nabla\cdot(\mu\boldsymbol{T}-\mu\nabla\psi)=-\nabla(\mu\boldsymbol{T}_0). \tag{2.52}$$

$$-\nabla\cdot(\mu\nabla\psi)=-\nabla(\mu\boldsymbol{T}_0). \tag{2.53}$$

Equations (2.51) and (2.52) are solved in the conducting regions, while (2.53) is solved in the non-conducting regions. The term $-\nabla(1/\sigma\nabla\cdot\boldsymbol{T})$ is added to Equation (2.51) in order to enforce Coulomb's gauge (Nerg, 2000).

2.4.3 2D and 3D eddy current problems of the studied motor

In 2D calculations, the magnetic field in the core of the motor is assumed to be two-dimensional. The three-dimensional end-region fields are modelled approximately by constant end-winding impedances in the circuit equations of the windings. The laminated stator iron core is modelled as a non-conducting, magnetically non-linear material, and the rotor steel is treated as a conducting, magnetically non-linear material. The magnetic vector potential $\boldsymbol{A}$ satisfies Equation (2.41), of which can be written with the reluctivity υ of the material

$$\nabla \times \left(\upsilon \nabla \times \boldsymbol{A} \right) = \boldsymbol{J} \,. \tag{2.54}$$

The current density $\boldsymbol{J}$ can be expressed as a function of the vector potential and the electric scalar potential, as shown in Equation (2.40). In 2D model, the vector potential and the current density have only the z-components, and thus the scalar potential ϕ has a constant value on the cross-section of the two-dimensional conductor and it is a linear function of the z-coordinate. The electromagnetic field of studied motor in the Cartesian plane can be described in terms of magnetic vector potential $\boldsymbol{A}$ as

$$\nabla \upsilon \nabla \boldsymbol{A} + \sigma \left(\frac{\partial \boldsymbol{A}}{\partial t} \right) = \boldsymbol{J} \,. \tag{2.55}$$

In order to take the end winding effects in the stator into account, Equation (2.55) is coupled with a circuit equation

$$u = Ri + L_{\mathrm{w}} \frac{\mathrm{d}i}{\mathrm{d}t} + \frac{\mathrm{d}\Psi}{\mathrm{d}t} \,, \tag{2.56}$$

where u is the voltage of the winding, i is the current of the winding, R is the resistance of the winding, Ψ is the flux linkage associated with the 2D modelled magnetic field, and L_{w} is the end-winding inductance, representing the part of flux linkage, which is not included in Ψ.

The circuit equations for the rotor cage are constructed using rotor network. Two adjacent bars in the rotor are connected by the end-ring resistances and inductances at the two end rings as well as by the inter-bar resistances along the axial length of the motor. The details of the construction of the rotor circuit equations are given for instance in Ho et al. (1999).

Using Equations (2.55) and (2.56), the non-linear time-stepping finite element analysis considering the non-linear magnetic characteristic of the core and the movement of the rotor the power loss in the solid-rotor-core is computed as

$$P = \iiint_V \rho \, \boldsymbol{J}^2 \mathrm{d}V \,, \tag{2.57}$$

where ρ is the resistivity of the material.

Flux 3D™ software has three different magnetic formulations that use different scalar potentials: the formulation of total scalar potential, the formulation in reduced scalar potential with respect to the source field $\boldsymbol{H}_{\mathrm{j}}$, and the formulation in reduced potential with respect to the electric vector potential $\boldsymbol{T}$. In the problem solved in this paper, two different scalar potential formulations are used: the total scalar potential to take into account the iron, and the reduced scalar potential with respect to $\boldsymbol{H}_{\mathrm{j}}$ to take into account the non-meshed inductors.

The electromagnetic field is described by joining the different electromagnetic potentials, the reduced potential in the air, the scalar potential in the ferromagnetic materials and magnetic

potentials with electric potential in the area of eddy currents. In scalar potential formulations, the magnetic field $\boldsymbol{H}$ can be written

$$\boldsymbol{H} = \boldsymbol{T} - \nabla\psi \,. \tag{2.58}$$

The term $-\nabla\psi$ is the irrotational part of the field $\boldsymbol{H}$ ($\nabla\times\nabla\psi = 0$). The term $\boldsymbol{T}$ can be rotational or not. In the regions where the currents are not zero, $\nabla\times\boldsymbol{T}$ is not zero. In the regions where $\boldsymbol{J}$ is the source current density, $\nabla\times\boldsymbol{T} = \boldsymbol{J}$.

In the case of current-free regions ($\boldsymbol{J} = 0$), the field $\boldsymbol{H}$ is irrotational ($\nabla \times \boldsymbol{H} = 0$). The magnetic field strength can be expressed as a function of the scalar potential

$$\boldsymbol{H} = -\nabla\psi \,. \tag{2.59}$$

This formulation is used in ferromagnetic regions, in which the eddy currents are neglected. This is the case of the stator that is laminated in order to diminish the losses caused by the eddy currents.

It is assumed that the current density is not zero everywhere. Thus, the field is separated into two parts. Using the reduced scalar potential ψ_{red} with respect to $\boldsymbol{H}_{\text{j}}$ the magnetic field strength can be written as

$$\boldsymbol{H} = \boldsymbol{H}_{\text{j}} - \nabla\psi_{\text{red}} \,, \tag{2.60}$$

where $\boldsymbol{H}_{\text{j}}$ is the source field, which is the field due to the currents of non-meshed coils when they are placed in vacuum.

In 3D eddy current problems, the fields in conducting regions must be represented by a vector. In this work, the electric vector potential $\boldsymbol{T}$ – magnetic scalar potential ψ ($\boldsymbol{T}$-ψ formulation) was used in the areas of eddy currents. The zero divergence of the current density ($\nabla \cdot \boldsymbol{J} = 0$) allows the definition of electric potential $\boldsymbol{T}$ in a solid conductor, from which the current density $\boldsymbol{J}$ can be derived

$$\boldsymbol{J} = \nabla \times \boldsymbol{T} \,. \tag{2.61}$$

Amperè's law ($\nabla \times \boldsymbol{H} = \boldsymbol{J}$) allows finding the expression for the magnetic field strength, which is written by means of the electric potential $\boldsymbol{T}$ and of the total magnetic scalar potential ψ

$$\boldsymbol{H} = \boldsymbol{T} - \nabla\psi \,. \tag{2.62}$$

Because four unknowns per node are necessary in the conducting regions, and three components for the electric vector potential $\boldsymbol{T}$ and one component for the magnetic scalar potential ψ are required, this $\boldsymbol{T}$ - ψ formulation is quite expensive.

In the eddy current problem solved in this paper, 1$^{\text{st}}$-order elements are used. The current density $\boldsymbol{J}$ is derived from the electric vector potential $\boldsymbol{T}$ ($\boldsymbol{J} = \nabla \times \boldsymbol{T}$), in an element of the mesh.

When a 1st-order mesh is used, the current density of the element is constant and the accuracy of $\boldsymbol{J}$ in an element is of average level (Cedrat, 2005).

Because the magnetic field strength $\boldsymbol{H}$ is almost equal to the electric vector potential $\boldsymbol{T}$ ($\boldsymbol{H} = \boldsymbol{T} - \nabla\psi$), the gradient of the magnetic scalar potential ψ is a corrective term. Thus, the variation order of the magnetic field strength $\boldsymbol{H}$ in an element is almost equal to the order of this element. Consequently, the magnetic field strength of the element is almost linear. In the case of this problem, when 1st-order elements are used, the accuracy of $\boldsymbol{H}$ in an element is good (Cedrat, 2005).

2.4.4 Modelling of harmonic eddy currents with 2D FEM

2D and 3D methods that are presented above are used to solve eddy current problems with numerical FE methods. In Chapter 3, the eddy current problem of the studied motor is presented and solved with the time-stepping 2D and time-harmonic 3D FEM.

As was mentioned earlier, the winding arrangement of winding has a significant influence on the winding harmonic that generates eddy currents on the surface of the solid-rotor-core. The use of semi-magnetic wedges as a stator slot lock is magnetically a very effective way to eliminate the permeance harmonics. The material of the semi-magnetic wedge has a low relative permeability μ_r. The relative permeability of the wedge material is usually from two to five. The material data of the slot wedges used in the prototype motor is presented in the product catalogue (Stenbacka Oy, 2006) and in Appendix C. When a low-permeability wedge is formed like a magnetic lens, it guides the flux lines to produce a uniform flux density on the rotor surface (Huppunen, 2004). The drawback of this method is the durability of the wedge material.

In the following, the eddy current distribution of the studied (P_n = 45 kW, n_n = 6000 min^{-1}) solid-rotor-core AFIM is studied with time-stepping 2D FEM using a radial flux approximation of the AFIM. This may be justified by the fact that the surface losses behave analogously in the two motor types and, of course, because no three-dimensional analysis could have been performed. The parameters of the machine can be found in Chapter 3. Figure 2.10 describes the eddy current distribution at one time instant in the rotor core and the coating material a) with a 7/9-short-pitch winding and b) with a full-pitch stator winding, respectively. In these Figures, semi-magnetic slot wedges are applied in the stator slot openings. Figure 2.10 c) illustrates the eddy current distribution at one time instant in the rotor core and the coating material when the 7/9-short-pitch winding and stator slots without semi-magnetic wedges are used.

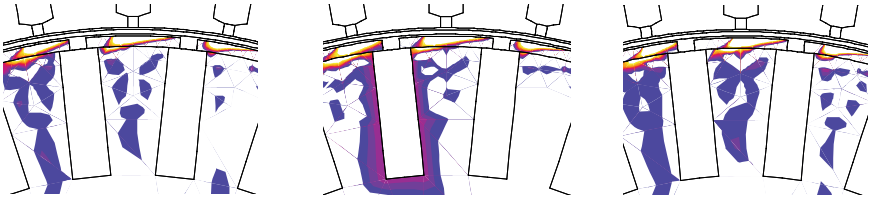

a)
7/9-short-pitch winding +
magnetic wedge

b)
full-pitch winding +
magnetic wedge

c)
7/9-short-pitch winding +
no-wedge

Fig. 2.10 Eddy current density on the rotor core and the rotor coating a) with a 7/9-short-pitch winding and semi-magnetic slot wedges, b) with a full-pitch winding and the semi-magnetic slot wedges, and c) the 7/9-short-pitch winding with open stator slots at the nominal 1.0 per cent slip. The air-gap length was kept at an initial value of 1.4 mm in both calculations. The same rotor-stator construction was used in both measurements. The rotor material Fe52 and the rotor coating material material 1, introduced in Chapter 3, were applied. The thickness of the rotor coating was 2.5 mm. Semi-magnetic slot wedges were used in the stator slot opening. There was a basic stator slot opening in both calculations. The supply voltage and frequency was 400 V and 200 Hz. At the nominal point of the motor, the rotor total losses are approximately 7 per cent higher in b) and approximately 28 per cent higher in c) compared with the a).

It is difficult to distinguish by just trying to see the differences in the Figs 2.10 a, b, and c. which one of the solutions is the best. However, after numerically analyzing the losses in the rotor core and the surface pads it is seen that the 7/9-short pitch winding together with the semi-magnetic slot wedges produces the lowest losses. The rotor total losses are increased by 7 % if a full-pitch winding is used and by 28 % if the semi magnetic slot wedges are left out of the 7/9 short pitch winding.

According to this study it may be concluded that the semi-magnetic slot wedges are the most effective means of minimizing the rotor surface losses but short pitching may also be recommended even though a short pitch winding is a bit difficult to manufacture. The significance of the slot wedges may be understood by the fact that the slot harmonics have as large a winding factor as the fundamental and even semi-closed slot openings produce large flux density dips under the slot openings – so called permeance harmonics. Large rotor surface eddy currents, when trying to eliminate the flux density changes, produce also large amounts of surface losses.

Numerous studies have been published on the minimization of the harmonic eddy current losses in the solid-rotor of the RFIM. It was assumed that by using the same methods (semi-magnetic slot-wedges and double-layer short-pitch windings), in the minimization the harmonic eddy current losses in the solid-rotor-core of the AFIM, the efficiency of the motor can be improved significantly. The calculations presented above verify that assumption. In solid-rotor-core machines, the minimization of the harmonic losses is of vital importance.

3. Electromagnetic design of the rotor construction

It is common knowledge that a pure solid-rotor radial-flux induction motor with a smooth rotor surface has poor electrical properties. This is because the depth of penetration into the rotor is low and the magnetic flux and the torque producing eddy currents are concentrated on the surface layer of the rotor, thus saturating the surface of the rotor. A radial-flux machine may, however, be built using a slitted rotor body and steel rotor end areas. The performance characteristics of this kind of an RFIM will be presented and published by Tuomo Aho in his doctoral thesis (2007). The performance of a solid-rotor radial-flux machine may be satisfactory without non-magnetic end-rings, but an axial-flux machine with a purely solid-rotor is practically impossible. The end effects of an axial-flux solid-rotor machine, especially in the rotor outer end-ring area, form a high rotor resistance thus causing a large slip and a low efficiency for a purely solid-rotor axial-flux machine. Hence, the solid-rotor AFIM must be designed with at least an outer end-ring of non-ferromagnetic material. In practice, a properly designed rotor with a non-ferromagnetic winding should be favoured in AFIMs.

The FEA was selected to evaluate the effects of the rotor slot number, air-gap length, depth of the rotor yoke and rotor teeth, and the thickness and resistivity of the rotor coating material on the performance characteristics of the studied AFIM. In order to find an optimally coated solid-rotor-core AFIM design, the FEM-based analysis was chosen. Analytical methods cannot be used directly, since the model with lumped parameters differs in a considerable way from the real electromagnetic phenomena of the motor. A problem concerned with the electromagnetic field in the induction motor is the influence of saturation, eddy currents and hysteresis on the rotor parameters. These cannot be determined with adequate precision by the traditional analytical methods.

With the FEM analysis it is possible to solve the Maxwell equations of the magnetic field problem numerically in a complicated geometry. It is known that 3D FEA needs considerably more computation time than 2D FEA. Furthermore, 3D model requires more definitions than the corresponding 2D model, and accordingly, more time will be needed to build a 3D FE model. The 3D FEM takes into account the 3D effects appearing in the electromagnetic behaviour of the machine. This makes the 3D model more accurate than 2D, if a proper mesh is used. For example, the leakage fluxes can be defined with the 3D FEA. Table 3.1 presents a comparison of the computation times of different models.

Table 3.1 Comparison of the computation time between the 2D and 3D FE methods.

Method	Number of elements	Computation time	Number of time steps
2D FEA, time-stepping	23584 (2^{nd} order)	Two days	8640
3D FEA, time-harmonic	247460 (1^{st} order)	10 days	

The accurate computation results require a dense mesh in the air-gap regime of the electrical machine, and thus the number of the generated volume elements in the 3D FEM tends to be large. Especially, for large machines with one or two pole pairs, the size of the system matrix becomes unacceptably large. The actual electromagnetic field problem in the case of an axial-flux solid-rotor-core induction motor is a three-dimensional non-linear eddy current problem, which is very complicated to be tackled with analytical calculations. Thus, 3D FEM should be used in order to obtain an accurate model of the electromagnetic fields inside the motor. In this specific 3D problem, the vector potential is to be solved within the whole rotor volume. This extremely increases the number of unknown variables extends the calculation time and makes the problem very demanding.

To accurately solve the behaviour of the magnetic fields in the machine, the use of a time-stepping method is required. This is especially, the case if the time variation of the fields in an electric machine is not sinusoidal, and thus the non-linearity of steel and the rotation of the rotor require the use of the time-stepping method. However, this is a very time-consuming calculation method in the simulation of the steady-state operation, especially in the case of induction motors, which traditionally have relatively long time constants associated with the windings. There are yet some ways to reduce the calculation time of the time-stepping method: an alternative is to use sinusoidal approximation to find an initial state that is closer to the steady state than the zero fields; another way is to assume the fields in the electric machines to be sinusoidal.

The Flux 2D/3D™ software by Cedrat was used in the FEM calculations. The motion of the rotor can be modelled accurately by using the time-stepping method. When the software Flux 2D/3D is used, there are two kinematic modules, imposed speed and coupled load modules, to take the motion of the rotor into account when the time-stepping method is used (Cedrat, 2005). In the imposed speed kinematic module, the rotor is considered to move at a constant velocity with respect to the stator, and in the coupled load kinematic module, the moving part drives an external device that represents the mechanical load of the device studied. If time-harmonic computation with sinusoidal approximation is used, the motion of the rotor can be taken into account by treating the rotor as a quasi- or pseudostationary object. In the pseudostationary approximation, the rotor is fixed and the motion is modelled by multiplying the conductivities of the rotor by slip.

Flux 2D/3D™ software includes a magnetodynamic, that is, time-harmonic solver. The solver allows carrying out a study of devices in a sinusoidal steady-state regime of the electromagnetic field, by taking possible eddy currents into account. The accuracy of the results of a finite element problem is mainly based on the correct discretization of the region considered. The 3D model is built using extrusion- and mapped-based mesh generators in Flux 3D™. The extrusive mesh generator allows generating a surface or volume mesh in layers for domains that may be obtained by extrusion. The meshes are potentially anisotropic and the obtained volume elements are prism or hexahedral shaped, depending on the mesh type of the faces of the base (triangles or rectangles). Figure 3.1 shows the meshes of the stator and the rotor over one pole pitch. The mesh of the faces consists of triangles, while the mesh of the volumes consists of prisms.

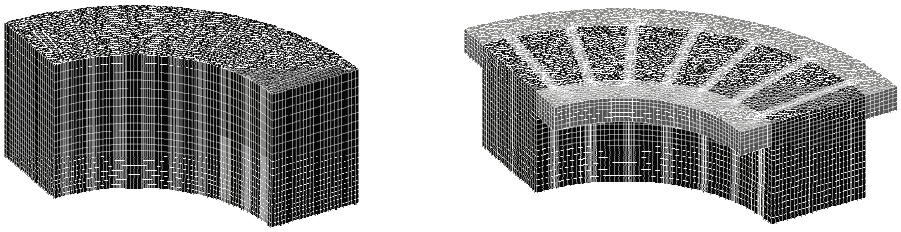

Fig. 3.1 Mesh densities of one pole of the stator (left) and the rotor without rotor coating (right) of the motor.

There are two different kinds of finite elements available in the Flux 3D™ software. These are 1st-order and 2nd-order elements. The accuracy of the computation increases when second-order elements are used. In this work, nodal 1st-order elements are used. That is because the use of 2nd-order elements requires too large an amount of computer memory in the modelling

of an AFIM. When using 1st-order elements, the potentials are approximated linearly and the fields derived from the potentials are constants in an element (Cedrat, 2005).

It is possible to model AF machines in a similar way as with the analytical computation when the 2D FEA is used, that is, by using the geometric mean radii of the machine as a designing plane or by using the quasi-3D computation method. A finite element program enabling the modelling of linear movement is recommended. However, such a tool was not available, and therefore in this work the geometry of the prototype machine was transformed to a normal radial-flux geometry, and the 2D FEM was used in the time-stepping analysis.

In this thesis, when the 2D FEM was used, the magnetic field in the core of the machine was assumed to be two-dimensional. The three-dimensional end-region fields of the stator were modelled approximately by using constant end-winding impedances in the circuit equations of the windings. The laminated stator iron core was modelled as a non-conducting, magnetically non-linear medium. The rotor steel and the rotor coating materials were treated as a conducting, magnetically non-linear material. The hysteresis was neglected in both media, and it was taken into account in the stator only in the post-processing. The rotor hysteresis was neglected.

The computation mechanism of the iron losses is described in the user manual of Cedrat (Cedrat, 2005). The iron losses, computed with 2D, include the hysteresis losses, the classical losses, and the excess losses. The losses depend on the flux density peak value $\hat{B}$, the frequency f, the lamination conductivity σ, and the lamination thickness d. The losses are calculated in the post-processing, which means that the lamination losses do not have an effect on the field solution itself; this of course, is wrong in principle but cannot be avoided with the present software. In the post-processing of the time-harmonic calculation, the iron losses of the stator are defined as

$$P_{\mathrm{Fe}} = \underbrace{k_{\mathrm{Hy}}\hat{B}^2 \cdot f}_{\text{hysteresis losses}} + \underbrace{\pi^2 \frac{\sigma d^2}{6}\left(\hat{B}f\right)^2}_{\text{the classical losses}} + \underbrace{k_{\mathrm{e}}\left(\hat{B}f\right)^{1.5} \cdot 8.67}_{\text{excess losses}}. \tag{3.1}$$

In the post-processing of the time-stepping calculation, the iron losses of the stator over one complete period T are defined as

$$\frac{1}{T}\int_0^T P_{\mathrm{Fe}}(t)\mathrm{d}t = k_{\mathrm{Hy}}\hat{B}^2 \cdot f \cdot k_{\mathrm{Fe}} + \frac{1}{T}\int_0^T k_{\mathrm{Fe}}\left[\sigma\frac{d^2}{12}\left(\frac{\mathrm{d}B(t)}{\mathrm{d}t}\right)^2 + k_{\mathrm{e}}\left(\frac{\mathrm{d}B(t)}{\mathrm{d}t}\right)^{1.5}\right]\mathrm{d}t, \tag{3.2}$$

where k_{e} is the coefficient of the excess losses, k_{Fe} the space factor, and k_{Hy} the coefficient of the hysteresis losses. To compute the iron losses of the stator, the user has to supply the coefficients k_{e}, k_{Fe}, and k_{Hy}. These factors depend on the steel material used.

The performance characteristics of the motor studied were evaluated by 2D, non-linear time-stepping finite-element analysis of the magnetic field (the coupled load module was used, thereby the shaft power of the motor being constant), that is, magnetic saturation, skin effect and the movement of the rotor with respect of the stator were taken into account. The circuit equations were used both to model the sinusoidal power supply and to take of the stator end

fields into account in the calculations. The circuit equations and the electromagnetic fields were solved together. The electromagnetic fields of the motor in the Cartesian plane can be described in terms of magnetic vector potential $\boldsymbol{A}$ as shown in Eq. (2.55). According to measurements and Huppunen (2004), the temperature of the solid-rotor at a typical high-speed application is approximately 150 °C; this temperature which was used in the rotor core and winding material resistivity correction.

In the 3D FE calculations, the time-harmonic analysis was used, and because of symmetry, two poles of the motor were modelled. In the 3D FE analysis, sinusoidal approximation was used. The motion of the rotor was taken into account by treating the rotor as a pseudo-stationary object, in other words, the rotor and the rotor coating materials were fixed and the motion was modelled by dividing the resistivities of the rotor and rotor the coating material by slip. Additionally, as was the situation with the 2D FEA, the 150 °C temperature of the rotor was used in the rotor core resistivity correction. The formulations of the 3D eddy current problem for the motor model were shown in Chapter 2.

3.1 Magnetic voltages

To determine the magnetizing current of the machine, the magnetomotive force (mmf) of the magnetic path of the machine has to be calculated. This magnetomotive force is the line integral of the magnetic field strengths in different parts of the machine. Thus, when a magnetic circuit of the electrical machine is designed, the analysis of the magnetic flux density $\boldsymbol{B}$ and the magnetic field strength $\boldsymbol{H}$ in different parts of the machine has to be studied. In the design of a magnetizing winding, which is considered a source of a current linkage, an induction machine is observed when running at no-load. In an induction machine, the magnetizing of the machine is carried out by the stator armature windings.

Essential for the design of magnetic circuit is the definition of the current linkage that is capable of creating the desired flux density, and the corresponding magnetizing current. The mmf per pole pair is solved by calculating the closed line integral of the field strength along a suitable integration path

$$F_{\mathrm{m}} = \oint \boldsymbol{H} \cdot \mathrm{d}\boldsymbol{l} = \sum i = \Theta , \tag{3.3}$$

where $\boldsymbol{l}$ is the unit vector parallel to the integration path. Figure 3.2 shows the integration path of the magnetomotive force.

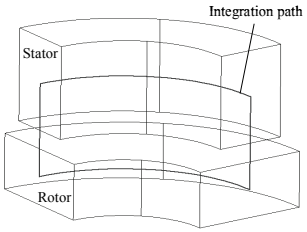

Fig. 3.2 One pole of the AFIM studied. Also the integration path over one pole is presented.

The length of the air-gap affects significantly the total magnetic voltage. The length of the air-gap in 3D FE analysis was set to be 0.9 mm. The sum of the magnetic voltages has to be

covered by the current linkage produced by the windings of an induction machine. By using the total magnetomotive force F_m calculated with 3D FEM, the magnetizing current of the stator winding is

$$I_m = \frac{F_m \cdot \pi \cdot p}{m \cdot k_{w1} \cdot N \cdot 2\sqrt{2}}. \quad (3.4)$$

According to Equation (3.4), the required magnetizing current of the test machine is about 36 A.

3.2 Effects of the number of rotor slots

In the cage-rotor induction machines, the selection of the stator and rotor combinations has to be done carefully in order to avoid poor performance of the machine. The current linkages of the stator and the rotor together create the air-gap magnetic flux density distribution that varies in time and space. The magnitudes of the harmonic fields influencing in the air-gap region depend highly on the ratio of the slot numbers of the stator and the rotor. The disturbances caused by asynchronous and synchronous torques and the vibration of an induction motor can be avoided by selecting the rotor slot number correctly. Proper stator-rotor slot combinations for the AFIM studied are selected by using the following conditions, which are presented by Richter (1954).

The selection of the rotor slot number in the case the AFIM with $p = 2$ and 36 stator slots is presented. For practical rotor manufacturing reasons the analysis is limited between the rotor slot numbers of 24 and 42. To reduce the asynchronous harmonic torques, the slot number of the rotor has to be as small as possible. It is generally recommended that $Q_r < 1.25Q_s$. In the case of 36 stator slots, the number of rotor slots should, hence, be smaller than 45.

Only machines with three-phase windings are studied. A three-phase winding creates harmonics of odd ordinals except those divisible by 3. The slot number of the rotor has to meet the condition $Q_r \neq 6pg$ in order to limit the synchronous torques when the motor is at stall. g may be may be any positive integer. Hence, in the case of the AFIM studied, the rotor slot numbers 12, 24, 36, 48, etc. are not recommended. The frequency converter, however, enables the use of speed controlled, and thus the supply frequency of the motor is increased gradually. The situation where the rotor should be at stall and the stator frequency should have its nominal value cannot exist. Consequently, this condition is not valid.

In order to avoid synchronous torques created by slot harmonics, the selection of the rotor slot number has to meet the conditions: $Q_r \neq Q_s$, $Q_r \neq ½Q_s$, $Q_r \neq 2Q_s$. In the case of the AFIM studied, all of the studied rotor slot numbers meet these conditions, except rotor slot number 36 (18, 72 do not belong to the area studied).

To avoid synchronous torques during running, the rotor slot number $Q_r \neq 6pg \pm 2p$. The + and – sings are valid for positive and negative rotational speeds, respectively. For example, the rotor slot numbers 28 and 40 would create harmful synchronous torques at positive rotation speeds, and the rotor slot number 32 would create harmful synchronous torques at negative rotation speeds. Hence, rotor slot numbers 28 and 40 should be avoided.

To avoid dangerous slot harmonics, the following conditions must be met: $Q_r \neq Q_s \pm 2p$, $Q_r \neq 2Q_s \pm 2p$, $Q_r \neq Q_s \pm p$, $Q_r \neq Q_s/2 \pm p$. For example, the rotor slot numbers 32 and 34 would create dangerous slot harmonics at negative rotation speeds. The rotor is, however, never operating at negative speed and, hence also 32 and 34 rotor slots may be used in this case. However, the rotor slot numbers 38 and 40 would create dangerous slot harmonics at positive rotation speeds, and therefore, these slot numbers should be avoided. Slot numbers 16, 20, 68 and 76 do not belong to the range to be analyzed.

In order to avoid mechanical vibrations $Q_r \neq 6pg \pm 1$, $Q_r \neq 6pg \pm 2p \pm 1$, $Q_r \neq 6pg \pm 2p \mp 1$. It can be observed that all odd rotor slot numbers create mechanical vibrations.

It may also be stated that, in principle, the air-gap flux permeance harmonics have the smallest effect on the losses when the numbers of the stator and rotor slots are as close to each other as possible. This can be explained by the fact that if the slot numbers should be the same (which is not allowed because of the problems with synchronous torques) the air-gap harmonics may not create circulating currents in the rotor cage since all the harmonics-induced voltages are in the same phase in the rotor bars. Therefore, $Q_r = 36$ should, in principle, produce the best efficiency. This may also be seen in Fig. 3.5 which shows that at $Q_r = 36$ the resistive rotor and aluminium cage losses are low.

Although the benefits of the rotor slotting are known, there are relatively few publications on the effects of the rotor slotting on the performance characteristics of the radial-flux solid-rotor induction motor. According to Jinning and Fengli (1987), the optimal number of slots is between 5 and 15 per pole pair in the case of RFIMs. It might be justified to assume that the phenomena associated with the rotor slotting are at least similar enough in RF and AF machines: therefore, the effects of slotting are studied in the following by using a radial flux counterpart of the AF machine studied.

The effects of the number of rotor slots on the performance of the prototype motor were studied with the 2D time-stepping FE analysis. The geometry of the prototype machine was transformed to normal radial-flux geometry by using the geometric average radius of the machine as a designing plane. The rotor core was manufactured using construction steel Fe52, presented in Chapter 4. The solid-rotor was radially slotted, and rotor slot numbers varying from 24 to 42 were analyzed. For practical manufacturing reasons, the shape of the rotor slot was selected to be rectangular in all calculations. The depth of the rotor slot and the amount of the aluminium of the squirrel-cage were equal in all calculations. Changing the rotor tooth width suitably in different versions means that the amount of steel conducting the magnetic flux to the rotor is equal in each calculation. The rotor was coated with the low-conductivity material 2 that is introduced in Chapter 4. The thickness of the coating was 2.5 mm. The dimensions of the rotor slot are not a result of any special optimization procedure. In order to obtain comparable results, the same stator with an identical mesh was used in all the calculations. The cross-section of the prototype motor RF counterpart construction is illustrated in Fig. 3.3.

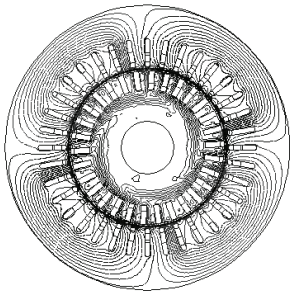

Fig. 3.3 Cross-sectional geometry of the RF counterpart motor used in analyzing the effects of slotting. The rotor bars are modelled from aluminium. The flux lines are drawn using 30 rotor slots, and the motor is operating at its nominal torque. The behaviour of the flux lines in the solid-rotor-core show that there are significant eddy currents in the core despite the low slip of the machine.

The effects of the rotor slot number on the rotor coating losses of the studied solid-rotor-core AFIM are shown in Fig. 3.4. The rotor was coated using the resistive coating material number 2. The Figure shows that decreasing the slot pitch, and thereby, the width of the coating pads, decreases the rotor coating pad losses in the slot number range studied in the calculations. This may be an expected result, because the smaller the pads are, the less space there is for eddy currents in the pads and the less losses we have.

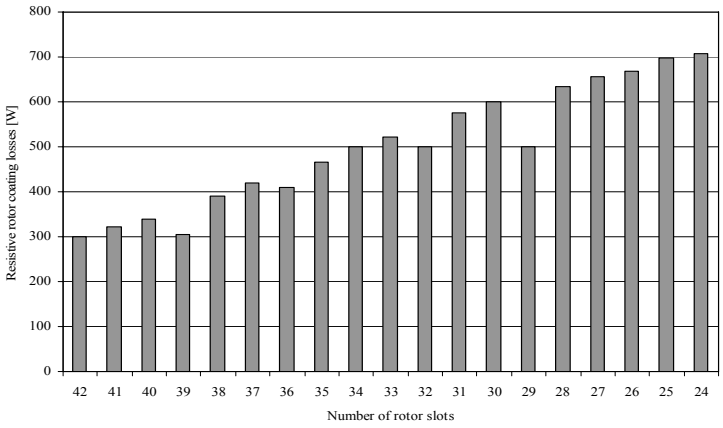

Fig. 3.4 Effects of the rotor slot number on the rotor coating losses when the torque of the motor was kept at the nominal values in all the calculations. Calculations were performed by the 2D FEM, and the time-stepping calculation method was used. The supply voltage and frequency were 400 V and 200 Hz. The rotor core and coating materials were Fe52 and the material 2, which are introduced in Chapter 4. The thickness of the coating was 2.5 mm and the length of the air-gap 1.4 mm. In the stator, there were double-layer 8/9-short pitch windings and semi-magnetic slot wedges. According to Richter (1954), in a four-pole 36-stator-slot motor, suitable rotor bar numbers are 26, 30, 32, 34 and 42 when positive rotation speeds are used. 24 and 36 slots produce unwanted synchronous torques at zero speed, while 28, 38 and 40 produce harmful torques at positive speeds, and all uneven slot numbers produce harmful mechanical vibrations. The waveforms of the electromagnetic torques in the case of 30 and 36 rotor slots are presented in Appendix C. In an inverter drive, such a rotor bar number may nevertheless be considered, since the conditions used by Richter (1954) are not valid. The sudden variations in the calculation results may be due to numerical errors in the calculations. The result is obvious. The smaller the pads are, the lower the eddy current losses will be.

Fig. 3.5 illustrates the effects of the rotor slot number on the rotor core and aluminium cage resistive losses. Only small variations as a function of rotor slot number may be seen as the amount of rotor cage material is kept the same.

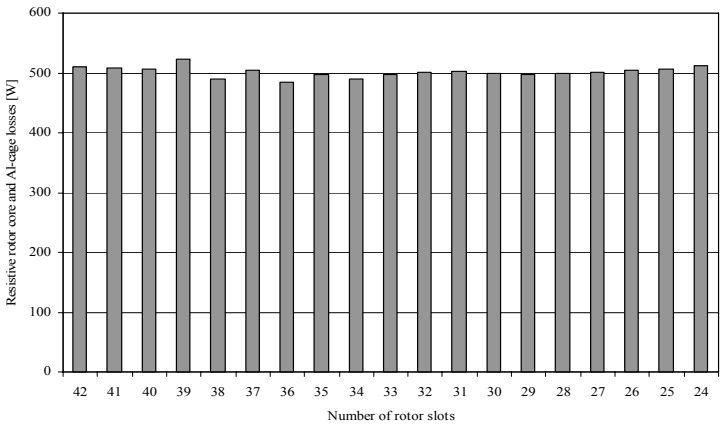

Fig. 3.5 Effects of the rotor slot number on the rotor core and aluminium cage resistive losses when the torque of the motor was kept at nominal values in all calculations. The calculation parameters are presented in the caption of previous Figure. The amount of the aluminium in the squirrel-cage is equal in every calculations. When using slot numbers close to the stator slot numbers (34 and 38) produce the small losses. The smallest losses are found at Q_r = 36, which is according to the reasoning above. This rotor slot number must, however, be avoided for several reasons e.g. magnetic or gas pulsation noise.

The effect of the rotor slot number on the efficiency, power factor and slip of the studied prototype motor are given in Fig. 3.6.

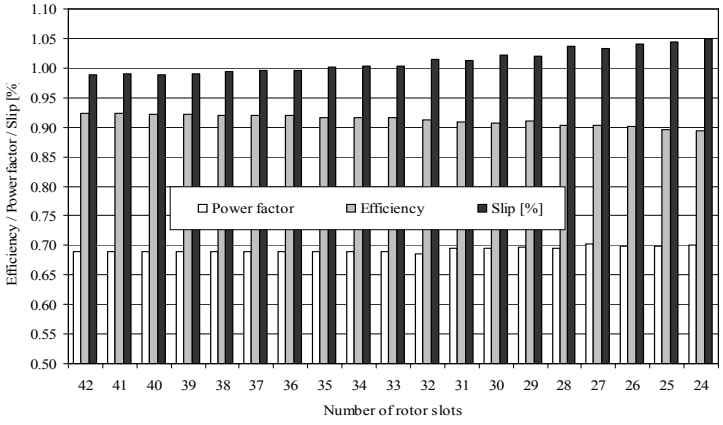

Fig. 3.6 Effects of the rotor slot number on the efficiency, power factor and slip of the 36 slot stator motor. The calculation parameters are presented in the caption of Figure 3.4. The efficiency value increases when the rotor slot number is increased, because the rotor coating losses are the most dominating loss component; the higher the rotor slot number is, the less losses there are in the pads, as it is shown in Fig. 3.4.

Finally, Fig. 3.7 studies the no-load losses in different rotors.

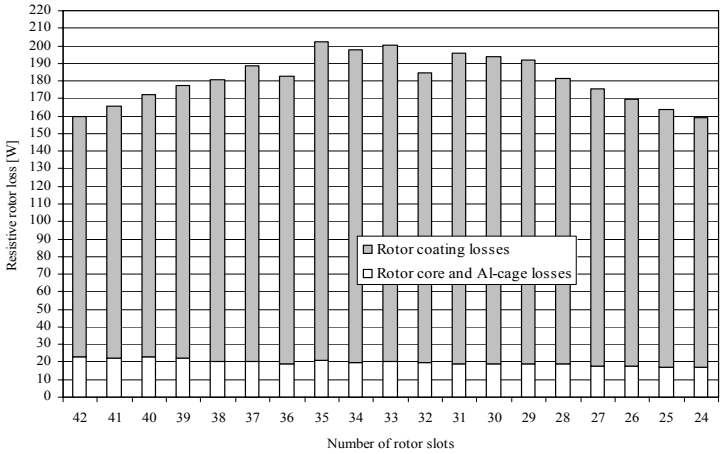

Fig. 3.7 Effects of the rotor slot number on the rotor coating and rotor core and aluminium cage resistive losses at no-load. Calculations were performed by the 2D FEM and the time-stepping calculation method was used. The calculation parameters are presented in the caption of Fig. 3.4. At no-load, the rotor surface loss is the dominating loss component. At no-load, the rotor coating loss seems to be small when the rotor slot number is high or low. There are no significant differences in the rotor core and aluminium cage losses between different rotor slot numbers.

The effects of the number of the rotor slots on the performance of the prototype motor were studied numerically with the time-stepping 2D FEM. In all cases, except in the no-load calculations, the shaft power of the motor was kept at the nominal value. It is also shown that the rotor and surface losses of the rotor do not vary evenly as a function of the number of rotor slots, and there are quite large changes from one slot number to the other. This is due to the difference in the air-gap harmonic content and the corresponding rotor surface losses between difference rotor slot numbers. The rated slip of the prototype motor decreases and the efficiency increases as the number of rotor slots is increased. This happens because the rotor surface losses form a significant part of the losses and this loss component decreases as the rotor coating pads become smaller. Because of the reduced losses, the power factor slightly decreases as the number of slots is increased.

The low rotor core and aluminium cage losses are achieved when the rotor slot number $Q_r = Q_s \pm p$. If the rotor slot numbers were equal $Q_r = Q_s$, the slot harmonics should not produce voltages of different phases to the aluminium cage. Thus, there should be no induced currents in the aluminium cage and the losses should be small. $Q_r = Q_s$ may, however, not be used because of large torque ripple in the motor as is shown in Appendix C, and because of a high noise level, which is caused when all the rotor slots travel simultaneously across the stator teeth or slot openings. When the rotor slot number $Q_r \geq Q_s + 2p$ or $Q_r \leq Q_s - 2p$, the rotor core and aluminium cage losses are increasing compared with the case where $Q_r = Q_s \pm p$. This is natural, since in such cases the harmonic voltages induced in the rotor bars are of different phases, and harmonic currents causing losses flow in circles formed by the adjacent bars and the corresponding end-ring areas. The calculation results confirm this – the losses are the lowest when the rotor bar numbers are near by close to the stator slot number.

3.3 Effects of the length of the air-gap

The length of the air-gap of a machine has a significant influence on the characteristics of an electric machine. In the machines that are designed for speeds above 3000 min^{-1} (which can be

reached with the 50 Hz network), the air-gap has to be increased considerably from the value obtained for a standard electric motor. Especially if the motor is equipped with a solid-rotor-core, the air-gap has to be designed with special care. The winding harmonic losses and the permeance harmonic losses can be reduced by decreasing the effects of the air-gap harmonics on the conducting medium.

The air-gap length plays a very important role when the flux harmonics on the surface of the rotor are studied. When the air-gap length is increased, the flux density distribution will smoothen on the rotor surface. A longer air-gap length increases the magnetizing current of the motor, and thus also the stator copper losses will increase. The loss minimum can be found between the rising stator copper losses and the diminishing rotor harmonic eddy current losses. The air-gap lengthening also reduces the power factor.

The effects of three-different air-gap lengths 0.9, 1.4, and 1.9 mm on the performance of the RF counterpart prototype motor were studied with the 2D time-stepping FEM. The rotor was coated with a low-conductivity material 2. The thickness of the coating was 2.5 mm. The other dimensions of the rotor and the stator were kept at their initial values in all the calculations. Figure 3.8 shows the efficiency, power factor, slip, and rotor losses as a function of length of the air-gap.

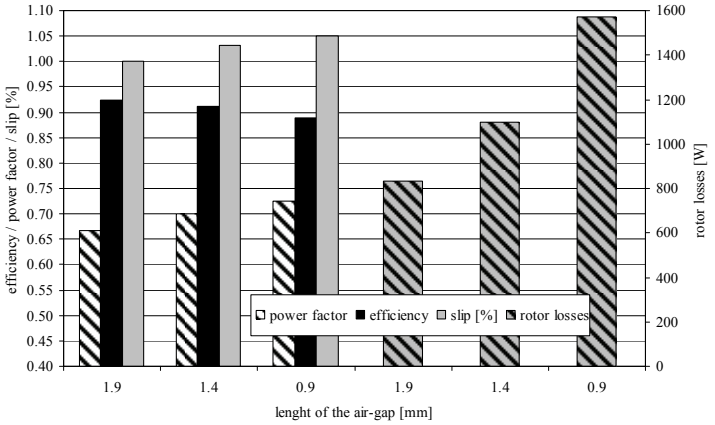

Fig. 3.8 Effects of the air-gap length on the efficiency, power factor, slip and rotor losses. In the calculations, the time-stepping 2D FEM was applied and the torque of the motor was kept at the nominal value in all the calculations. The supply voltage and the frequency were 400 V and 200 Hz. The rotor core and coating materials were Fe52 and the material 2, which are presented in Chapter 4. The thickness of the coating was 2.5 mm. In the stator, there were double-layer 7/9-short pitch windings and semi-magnetic slot wedges. As can be seen, the rotor losses are highly dependent on the air-gap length, and decreasing the air-gap from 1.9 mm to 0.9 mm almost doubles the rotor losses. The power factor at a small air-gap is increased mainly by the increased losses. The length of the air-gap varies between 0.9 and 1.9 mm and the highest efficiency value 0.94 is achieved when the thickness of the air-gap is 1.9 mm.

Figure 3.9 shows the spectra of the air-gap flux density normal components just above the rotor surface for the coated rotor when the lengths of the air-gap are 0.9, 1.4, and 1.9 mm. These harmonics show clearly the effect of the air-gap length on the performance of the rotor losses. When a thin air-gap is used, the rotor losses are higher compared with the losses at a longer air-gap.

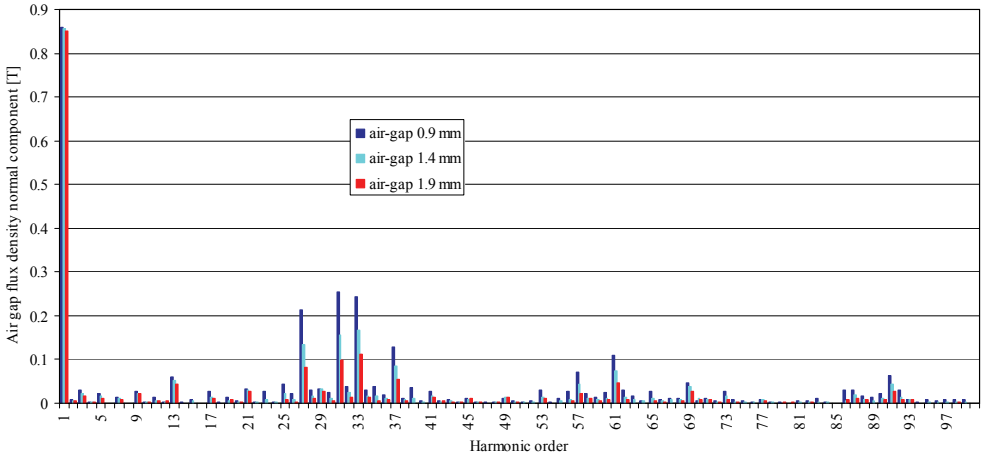

Fig. 3.9 Spectra of the flux densities on the rotor surface with 2.5 mm coating (material 2 was used as a coating material) at the nominal point with different air-gap lengths. In the calculations, the time-stepping 2D FEM was applied. The supply voltage was 400 V and the supply frequency 200 Hz. In the stator, double-layer 7/9-short pitch windings and semi-magnetic slot wedges were used. Spectra of the flux densities indicate that the best efficiency is achieved when the length of the air-gap is 1.9 mm as was shown in the previous Figure.

When the air-gap length is decreasing the power factor, the slip and the rotor loss values increase. As a result, the efficiency decreases. It can be seen that the losses at the surface of a solid-rotor decrease radically when the air-gap is increased, whereas the increase in the magnetizing current in the stator leads to a smaller increase in the losses. The efficiency value decreases from 0.93 per cent to 0.89, the power factor values increase from 0.67 to 0.73, and the slip value increases from 1.00 to 1.05 when the length of the air-gap decreases from 1.9 to 0.9 mm.

3.4 Effects of the depth of the rotor teeth

With the analytical methods, the depth of the rotor tooth can be calculated by assuming that the teeth of the machine are not saturated, and almost the complete flux of the slot pitch flows along the teeth, and there is no flux in the slots and in the slot insulations. By neglecting the slot opening and taking the space coefficient k_{Fe} of iron into account, the minimum depth of the tooth is obtained by Eq. (2.8)

The effects of the depth of the rotor tooth on the performance characteristics of the prototype machine were determined with the time-harmonic 3D FEA. The nominal point calculations of the motor were carried out, and the motion of the rotor (s = 1.0 per cent) was modelled by dividing the resistivities of the rotor and the rotor coating by slip. The rotor coating material was the material 2 described in Chapter 4 and the thickness of the rotor coating was 2.5 mm. Two different rotor tooth depths, 20 mm and 15 mm, were used as is shown in Fig. 3.10. With these calculations, the current and flux density distributions on the surface of the rotor tooth are determined.

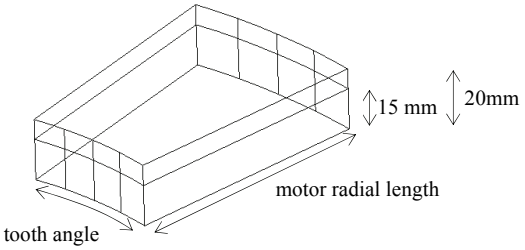

Fig. 3.10 Two different rotor tooth depths, 20 mm and 15 mm, were used.

Figures 3.11 and 3.12 show the flux and current density distributions on the surface of the rotor tooth as a function of rotor tooth angle and motor length, when the depths of the rotor teeth were 20 and 15 mm.

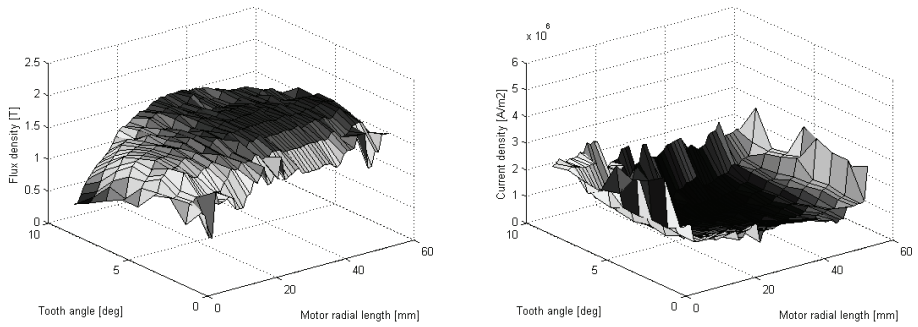

a) b)

Fig. 3.11 a) Flux and b) current density distributions on the top of the rotor tooth, when the rotor tooth depth was 20 mm. In the calculations, the time-harmonic 3D FEM was applied. The conductivities of the rotor core and coating materials were multiplied by 1.0 per cent slip, i.e., the nominal point of the motor was performed in the calculation. The rotor core material Fe52 and the rotor coating material 2 were applied in the calculations. The supply voltage was 400 V and the supply frequency 200 Hz. The length of the air-gap was 1.4 mm and the thickness of the rotor coating material 2.5 mm. In the stator, double-layer 8/9-short pitch windings and semi-magnetic slot wedges were used.

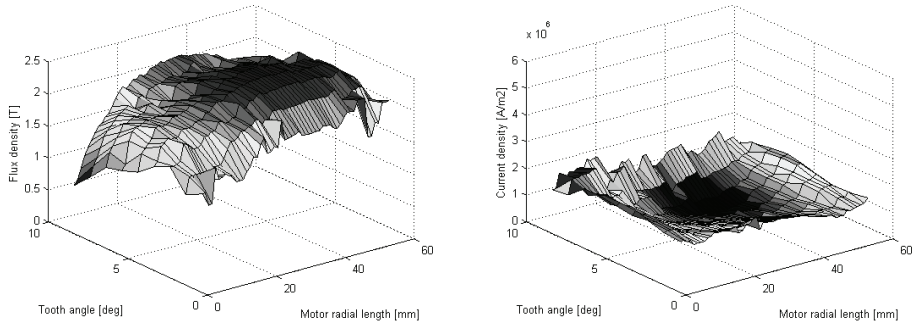

a) b)

Fig. 3.12 a) Flux and b) current density distributions on top of the rotor tooth, when the rotor tooth depth was 15 mm. In the calculations, the time-harmonic 3D FEM was applied. The conductivities of the rotor core and coating materials were multiplied by 1.0 per cent slip, i.e., the nominal point of the motor was performed in the calculation. The rotor core and rotor coating materials were Fe52 and material 2. The supply voltage was 400 V and the supply frequency 200 Hz. The length of the air-gap and the thickness of the rotor coating material were 1.4 mm and 2.5 mm. In the stator, double-layer 8/9-short pitch windings and semi-magnetic slot wedges were used. The figures clearly indicate the three-dimensional behaviour of the flux and the currents. By looking at the Figures, it is obvious that the RF counterpart motor cannot accurately describe the AF motor.

The results of these time-harmonic calculations are not very accurate, because the effects of the slot harmonics are not included in the analysis. In an accurate FEM analysis, time-stepping calculations would be needed, but the limited calculation capabilities do not allow such an option. Some conclusions can nevertheless be made from the flux and current density distributions calculated by the time-harmonic solver. According to Vogt (1996), the permitted flux density of the rotor tooth for asynchronous machine should be between 1.5 T and 2.2 T. The results of the calculations show that the flux density values are between these flux density values. Additionally, it can be seen that the distributions of the flux and current densities have differences on the surface of the rotor teeth, when the depth of the rotor teeth is changed.

3.5 Effects of the depth of the rotor yoke

With the analytical methods, the depth of the rotor yoke can be calculated with Eq. (2.9). According to Vogt (1996), the permitted flux density of the rotor yoke for an asynchronous machine is 0.4–1.6 T. The mechanical strength of the solid-rotor-core is not a problem contrary to laminated rotors, where mechanical constraints may determine the minimum thickness of the rotor yoke. The prototype AF machine was modelled and the electromagnetic field analysis was carried out by the 3D FEM. The time-harmonic calculation was used in the field analysis of the AF prototype machine. Rotor yoke depths, 20, 25, 30, 35, 40, 45, and 50 mm were used, as is shown in Fig. 3.13. Figure 3.14 shows the flux density distribution on the rotor yoke as a function of rotor tooth angle and active length of the motor.

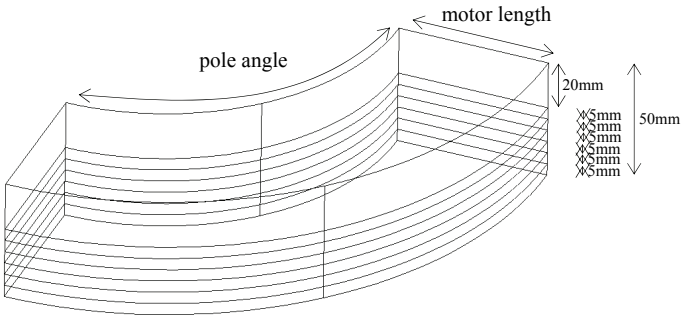

Fig. 3.13 Seven different rotor yoke depths 20, 25, 30, 35, 40, 45, and 50 mm were used.

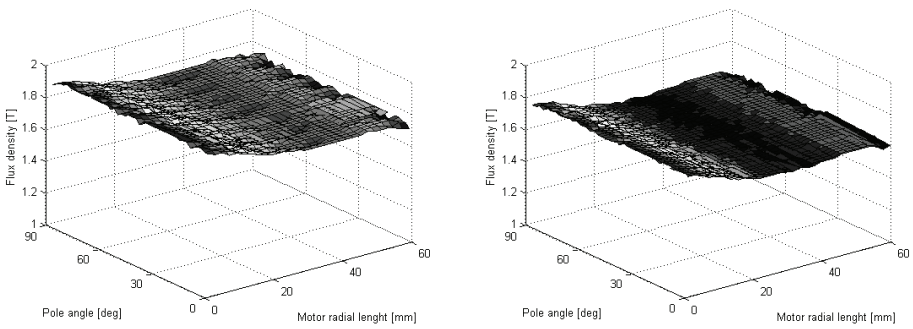

(a) (b)

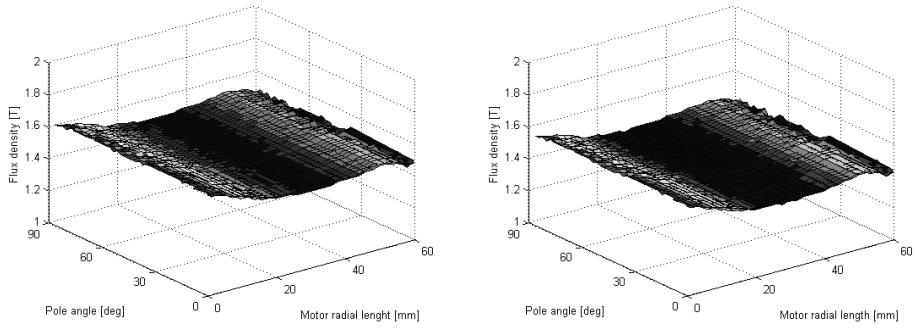

(c) (d)

Fig. 3.14 Flux density distributions on the bottom of the rotor yoke, when the rotor yoke depth was a) 20, b) 30, c) 40, and d) 50 mm. In the calculations, the time-harmonic 3D FEM was applied. The calculations were performed at the nominal point of the motor, i.e., the conductivities of the rotor core and coating materials were multiplied by the slip. The supply voltage was 400 V and the frequency was 200 Hz. The rotor core material was Fe52 and the rotor coating pads were made of the material 2. The length of the air-gap, the thickness of the rotor coating material, and the depth of the rotor teeth were 1.4, 2.5, and 15 mm. In the stator, double-layer 8/9-short pitch windings and semi-magnetic slot wedges were used. It can be seen that the flux density on the rotor yoke increases, when the depth of the yoke decreases. We can also see that the inner radius of the rotor is more sensitive to the changes in the depth of the rotor yoke.

When the flux density values from the numerical calculations are compared with the flux density limits given by Vogt (1996), it is obvious that the rotor yoke depth should be at least 40 mm. If a thinner rotor yoke is used, the rotor yoke may be saturated, which causes iron losses in the rotor core. However, again, the time-harmonic 3D FEM calculations are not absolutely accurate, but numerical results indicate that the flux density values in the inner radius of the rotor are too high if the depth of the rotor yoke is less than 40 mm.

3.6 Effects of the coating thickness and resistivity

The coating pads and rings presented in Fig. 4.2 are used to attenuate the high-frequency harmonics before they penetrate into the rotor core material. The eddy current losses in the solid-rotor-core can be reduced for instance by coating the rotor surface. The coating smoothens the flux density distribution, and hence, attenuates high-frequency flux harmonics before they penetrate into the rotor core material. In high-speed and medium-speed machines, copper is often used as a coating material. The AF induction rotor studied is coated with the coating pads that are fabricated from three different high-resistive materials, Fe52, material 1, and material 2, which are presented in Chapter 4. Additionally, the coating rings manufactured from copper and material 2 were used. The copper ring on the surface of the rotor core acts as a mirror for the high-frequency air-gap harmonics thus preventing them to penetrate into the solid-rotor-core. When the coating is made of a ferromagnetic material having a high resistivity, the surface impedance of the rotor increases and the induced eddy currents will decrease. In a magnetically linear substance, the surface impedance $\underline{Z}_s$ is defined as

$$\underline{Z}_s = \frac{\underline{E}}{\underline{H}} = \frac{1+\mathrm{j}}{\sigma\sqrt{2}}\sqrt{\omega\sigma\mu} = \frac{1+\mathrm{j}}{\sqrt{2}}\sqrt{\omega\mu\rho}\,. \tag{3.5}$$

In a saturable medium, no exact equation for the depth of penetration can be given, yet we may still use (3.5) as a guideline for reasoning. According to Pyrhönen (1991a), the highest

value of the surface impedance is obtained when the coating material has a high permeability and a high electrical resistivity. Another method to decrease the losses in the rotor surface is to minimize the rotor surface impedance by using a well-conducting coating layer, such as copper. Copper mirrors the harmonics and does not let them to penetrate deep into the rotor. This mirroring effect, however, results in, large eddy currents in copper, and eddy current losses are created.

The current and flux density distributions on the surface of the rotor tooth have been determined with the time-harmonic 3D FEM and do not, hence, contain information about the rotor movement. In the 3D FE calculations, the nominal point of the motor was carried out. To find out the effects of the rotor surface pad thickness on the motor performance, the thickness of the rotor surface pad material was varied and the resistivity of the rotor coating material was kept at the initial values. The rotor coating material was Fe52 and the thicknesses of the surface pad were 1.5, 2.0, 2.5, and 3.0 mm. Additionally, when the effects of the rotor coating resistivity on the motor performance characteristics were studied, the thickness of the rotor coating was kept at the initial value of 2.5 mm and the rotor surface pad resistivity was varied by using three different coating materials, Fe52, material 1, and material 2.

Flux penetration into the conducting rotor material causes eddy currents, which tend to prevent the flux penetration. The penetration depth in a ferromagnetic, conducting material is low, and thus the flux concentrates near the surface of the rotor tooth. When the rotor is radially slotted, the slots increase the reluctance on the tangential flux path and the flux has to penetrate deeper on its way to the other magnetic pole. Figure 3.15 describes the flux and current density distribution at a time instant on a rotor tooth with 2.5 mm thick rotor surface pads at 1.0 per cent slip.

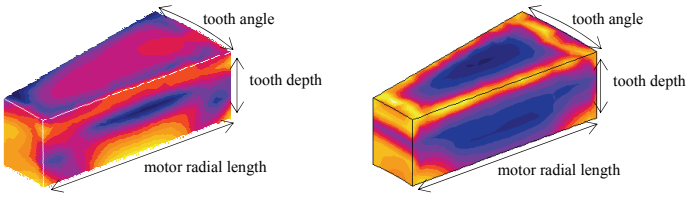

Fig. 3.15 Flux density distribution of the rotor tooth is shown on the left and the eddy current density distribution of the rotor tooth is shown on the right. The flux and current density distributions of the rotor tooth are illustrated at a peak value of the flux density. In the calculations, the time-harmonic 3D FEM was applied. The calculations were performed at the nominal point of the motor, i.e., the conductivities of the rotor core and coating materials were multiplied with 1.0 per cent slip. The supply voltage 400 V and frequency 200 Hz were used. The coating pads fabricated from material 2 were used as a coating material, and the coating pads were placed on top of the rotor teeth as was shown in Fig. 4.2. The thickness of the coating pad was 2.5 mm. The material of the rotor core was Fe52 and the depth of the rotor teeth were 20 mm. The length of the air-gap was 1.4 mm.

In the case, where the coating and the rotor core are manufactured from the same material, the surface impedance of the rotor does not change and the high-frequency air-gap harmonics that are not attenuated smoothen before they penetrate into the rotor core material. The current penetration into the rotor material depends on the flux penetration. Figure 3.16 describes the current and flux density distributions at a time instant on a surface of the rotor with a 1.5, 2.0, 2.5 and 3.0 mm thick rotor surface pads. Fe52 material was used as a rotor coating material.

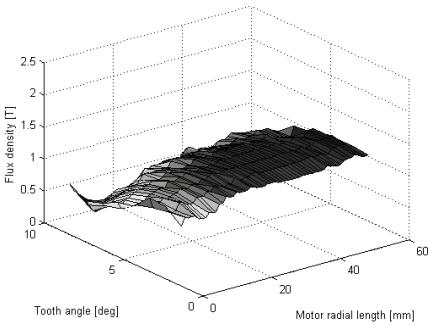
Flux density [T]
Tooth angle [deg]
Motor radial length [mm]

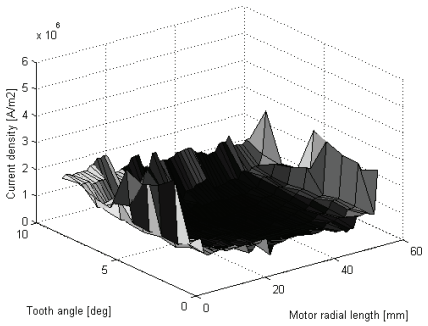
x 10^6
Current density [A/m2]
Tooth angle [deg]
Motor radial length [mm]

(a)

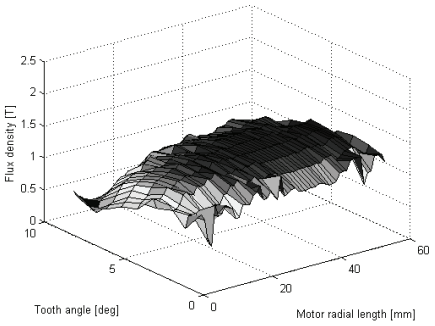
Flux density [T]
Tooth angle [deg]
Motor radial length [mm]

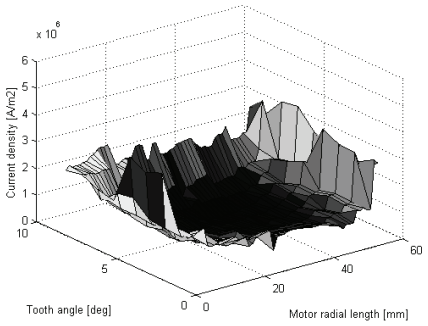
x 10^6
Current density [A/m2]
Tooth angle [deg]
Motor radial length [mm]

(b)

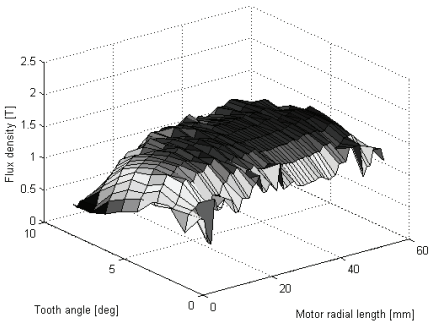
Flux density [T]
Tooth angle [deg]
Motor radial length [mm]

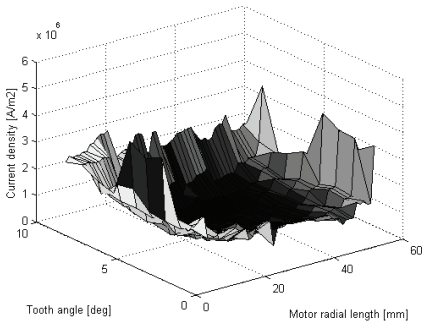
x 10^6
Current density [A/m2]
Tooth angle [deg]
Motor radial length [mm]

(c)

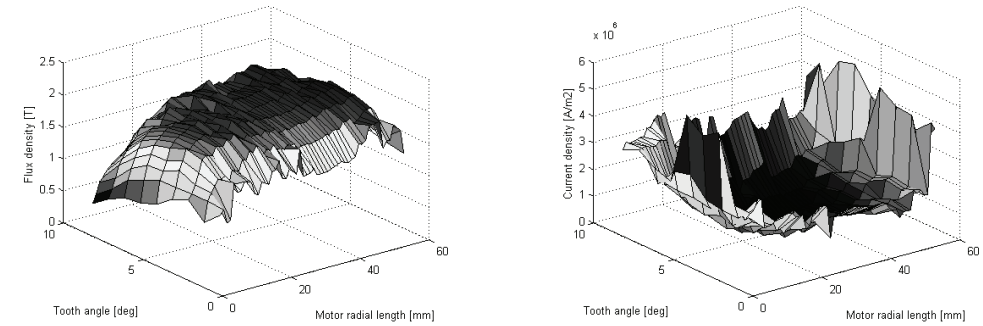

(d)

Fig. 3.16 Flux and current density distributions on the surface of the rotor tooth, when the thicknesses of the coating pad were a) 1.5, b) 2.0, c) 2.5, and d) 3.0 mm. The rotor core and coating material was Fe52. The coating pads were placed on the surface of the rotor teeth as is shown in Fig. 4.2. In the calculations, the time-harmonic 3D FEM was applied. The calculations were performed at the nominal point of the motor, i.e., the conductivities of the rotor core and coating materials were multiplied by 1.0 per cent slip. The supply voltage 400 V and frequency 200 Hz were used. The depth of the rotor teeth was 20 mm and the length of the air-gap was 1.4 mm.

Figure 3.17 illustrates the current and flux density distributions at an instant of time on a surface of the rotor with 2.5 mm thick rotor surface pads. Materials Fe52, material 1 and material 2 were used as a rotor coating material.

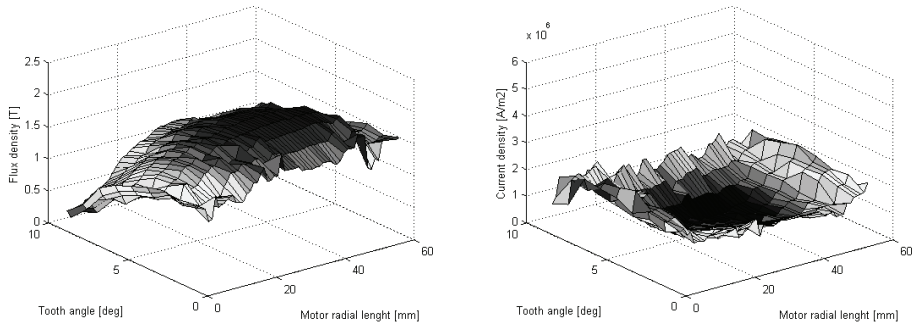

(a)

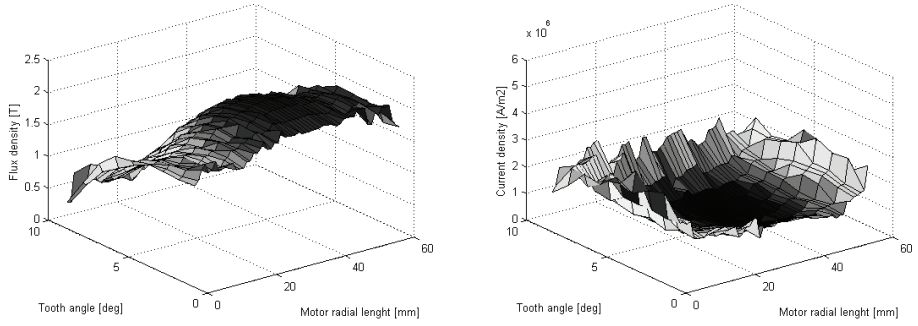

(b)

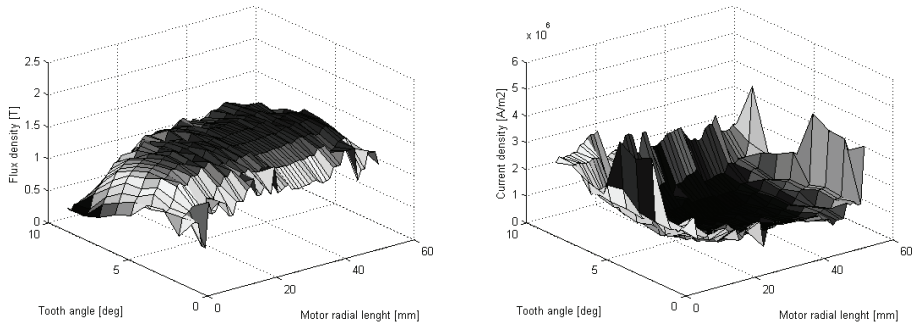

(c)

Fig. 3.17 Flux and current density distributions on the surface of the rotor tooth. The calculations were performed at the nominal point of the motor. The material used in the coating pads were a) the material 2, b) the material 1, and c) Fe52. The thickness of the coating pads was 2.5 mm. The coating pads were placed on the surface of the rotor teeth as is shown in Fig. 4.2. In the calculations, the time-harmonic 3D FEM was applied. The calculations were performed at the nominal point of the motor, i.e., the conductivities of the rotor core and coating materials were multiplied by 1.0 per cent slip. The supply voltage 400 V and frequency 200 Hz were used. The rotor core material was Fe52. The depth of the rotor teeth was 20 mm and the length of the air-gap 1.4 mm.

The rotor coating pads were made of a material with a high resistivity, and thus the surface impedance of the rotor increased, as was shown by Eq. (3.5). By using the high-resistivity rotor coating material, the high-frequency air-gap harmonics are attenuated and smoothened before they penetrate into the rotor core material. Therefore, the eddy current losses caused by the permeance harmonics decrease and the rotor surface losses are reduced as it is illustrated in Fig. 3.18. As different authors, for instance Lähteenmäki (2002), have reported, good results are obtained when using copper coating in high-speed radial-flux motors. A copper coating ring was also evaluated in this study. For comparison, a ring made of the material 2 was also calculated. The effects of the 0.5, 1.5, and 2.5 mm thick copper ring, the 2.5 mm thick material 2 coating ring, and 1.5, 2.0, 2.5, and 3.0 mm thick ferromagnetic coating pads on the performance of the rotor core losses are presented in Fig. 3.18. The copper coating also increases the rotor fundamental current conductivity so that the slip becomes smaller. With the mirroring function, the copper coating protects well the rotor core against eddy current losses.

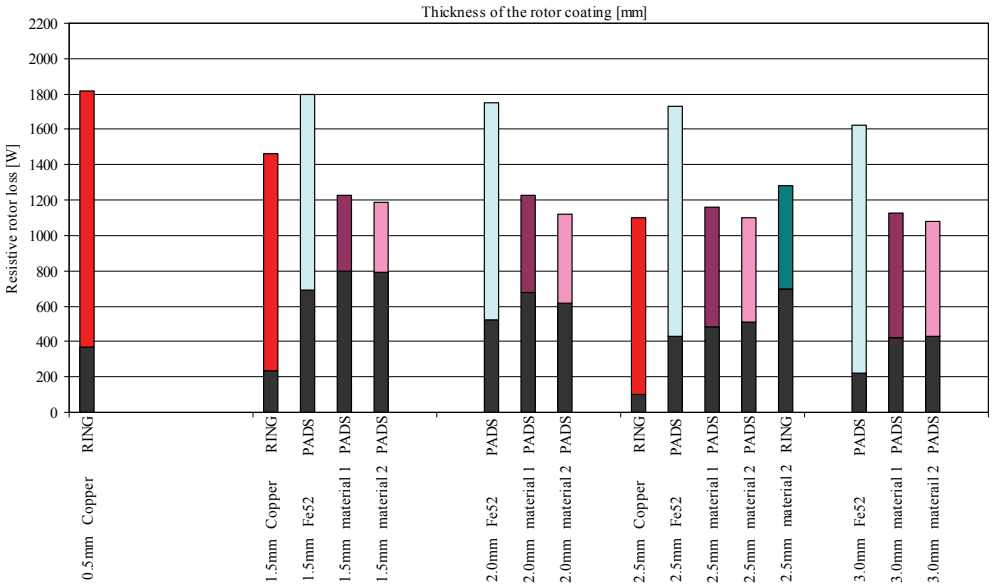

Fig. 3.18 Losses of the rotor core and rotor coating are shown as a function of rotor coating material thickness. In the calculations, the time-stepping 2D FEM was applied and the calculations were performed at the nominal point of the motor. Ferromagnetic rotor coating materials Fe52, material 1, and material 2 and coating material thicknesses 1.5, 2.0, 2.5, and 3.0 mm were applied. Additionally, 0.5, 1.5, and 2.5 mm thick uniform copper rings were used as a coating on the whole rotor surface. The losses in the rotor core and in the different coating materials are presented separately. A supply voltage of 400 V and a frequency of 200 Hz were used. The rotor core material was Fe52. The depth of the rotor teeth was 20 mm and the length of the air-gap 1.4 mm. The slip values for the 2.5 mm thick coating pads made of Fe52, material 1 and material 2 are: 0.95, 1.00, and 1.02 per cent, respectively. The slip values for the 2.5 mm thick coating ring of the material 2 is 1.18 per cent and the slip values for 0.5, 1.5, and 2.5 mm copper rings 1.02, 0.91, and 0.80 per cent, respectively. The power factor values for the pads made of Fe52, material 1, and material 2 were 0.72, 0.70, and 0.70, when 2.5 mm coating pads were used. The power factor values were 0.64, 0.66, and 0.68 for the 2.5, 1.5, and 0.5 mm thick copper rings.

It can be seen in Fig. 3.18 that if the ratio of the sleeve and the rotor core resistivities is more than 1.0, which is the case, when the materials 1 and 2 are used as a coating material, the rotor surface losses become smaller. When a 2.5 mm thick copper ring is used, the losses in the rotor core are lower (100 W) but the eddy current losses in the copper ring are notable (1000 W). The rotor total losses are equal when 2.5 mm thick coating pads made of the material 2 and 2.5 mm thick copper rings are used as a rotor coating. Additionally, it can be noticed that when the thickness of the rotor ferromagnetic coating is increased, the losses generated in the rotor core decrease and the losses generated in rotor coating material increase. However, when the thickness of the copper ring is increased, the losses in the rotor core and the copper ring decrease because the slip-dependent Joule losses decrease.

The effect of the rotor coating on the air-gap harmonic content was studied by observing the flux density along a path through the middle of the air-gap for every time step during one cycle. The normal component of the air-gap flux density was taken over the 360 mechanical degrees, and the values of the harmonics were obtained from a 2D FE solution with 720 sampling points along the path through the middle of the air-gap. The strongest harmonic components are caused by the stator and rotor slotting, besides the fundamental magnetic flux density component. In the studied AF motor, harmonics created by the stator and the rotor

slots generate eddy currents that cause surface losses. These harmonic components caused by the rotor and stator slotting can be clearly seen in Figs. 3.18 and 3.19.

Figure 3.19 shows the spectra of the air-gap flux density normal component for the coated and uncoated rotors ($Q_s = 36$, $Q_r = 30$). The rotor coating pads fabricated from the material 2 and the rotor coating ring fabricated from copper and was used. Determination of the harmonic components caused by the rotor and stator slotting, the stator winding, and the saturation of the iron cores are presented in Appendix D. The doubler layer winding causes the 5^{th}, 7^{th}, 11^{th}, 13^{th}, etc. harmonic components. The slot harmonics 29^{th}, 31^{st}, 61^{st}, and 91^{st} are caused by the rotor slotting. The slot harmonics 35^{th}, 37^{th}, and 91^{st} are caused by the stator slotting. The saturation of the solid-rotor-core generates the 27^{th}, 33^{rd}, and 61^{st} harmonic components.

The 29^{th}, 31^{st}, 61^{st}, and 91^{st} harmonic components on the rotor surface are attenuated by 7.1, 9.1, 11.0, and 13.0 per cent when the rotor is coated with the material 2 pads and 80.0, 41.5, 68.2, and 92.2 per cent when the rotor is coated with a copper ring. It is shown that the most effective harmonic components are attenuated when pads made of the material 2 or a copper ring is used. In general, the higher harmonics are attenuated more effectively than the lower harmonics when a high-resistive rotor coating material is applied. This phenomenon is explained by the increase in the rotor surface impedance. When the rotor surface impedance is increased, the high-frequency air-gap harmonics are attenuated.

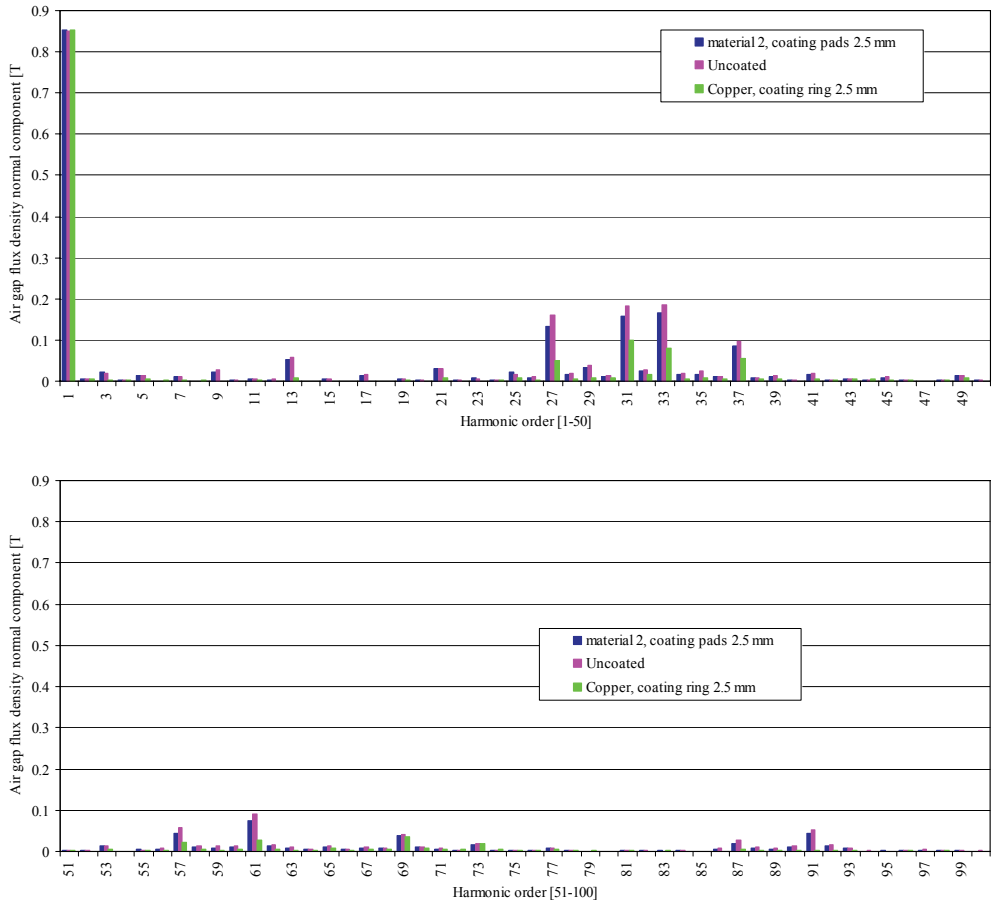

Fig. 3.19 Spectra of the flux densities on the rotor surface with a 2.5 mm coating (pads and ring) and without coating at the nominal point of the motor. In the calculations, the time-stepping 2D FEM was applied. The material 2 and copper were used as a coating material and rotor core material was Fe52. The supply voltage was 400 V and the supply frequency 200 Hz. The length of the air-gap was 1.4 mm. In the stator, double-layer 7/9-short pitch windings and semi-magnetic slot wedges were used.

In order to find out the effect of the coating resistivity on the rotor losses, the coating resistivity was varied, and the flux density harmonic components in the air-gap were observed. Two different coating materials presented in Chapter 4 were used. Calculation results indicate that when the materials 2 pads are used as a coating material, relatively small changes in the low-frequency air-gap harmonics can be observed when compared with the coating material Fe52. However, somewhat larger changes are observed in the case of high-frequency harmonics. Figure 3.20 illustrates the spectrum of the air-gap flux density normal component when Fe52, material 1 and material 2 were used as a rotor coating material.

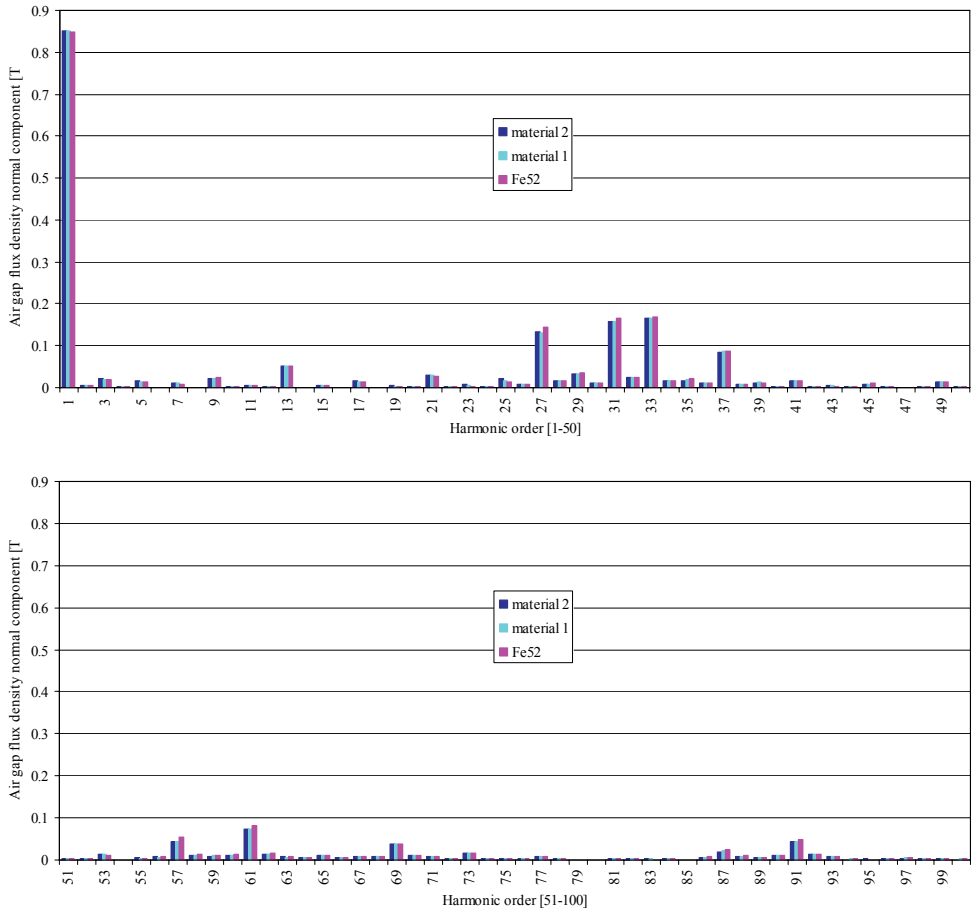

Fig. 3.20 Spectra of the air-gap flux densities for a coated motor. In the calculations, the time-stepping 2D FEM was applied. The supply voltage was 400 V and the supply frequency 200 Hz. The coating pads were manufactured from materials Fe52, material 1, and material 2. The thickness of the coating was 2.5 mm and the length of the air-gap 1.4 mm. In the stator, double-layer 7/9-short pitch windings and semi-magnetic slot wedges were used.

.

It can be seen in Fig. 3.20 that, the harmonics components are slightly attenuated when the rotor coating material resistivity is increased. Because of the high-resistivity coating material, the rotor surface losses caused by the air-gap harmonics decrease. However, the copper ring seems to decrease the harmonic losses on the rotor core most effectively as it is shown in Fig. 3.19.

3.7 Summary

To determine the magnetizing current of the motor, the magnetomotive force of the magnetic path of the motor was calculated. Generally, the power factor values of the solid-rotor-core motors are quite low, approximately 0.7. This is mainly caused by the large air-gap length and the large phase angle of the conducting and magnetically non-linear solid-rotor materials. In the case of the motor studied, for practical reasons, the pole pair number is two instead of one, which, by decreasing the magnetizing inductance, degrades the power factor value even more.

The effect of the rotor slot number on the resistive rotor losses at the nominal operation point was studied. It was shown that the rotor resistive losses decrease as a function of the rotor slot number. Additionally, there were large changes from one slot number to the other. In the practical work by Richter (1954), certain stator-rotor slot combinations produce unwanted harmonic field contents in the air-gap flux, which can cause mechanical vibrations. The rotor slot number 30 of the motor studied was selected based on Richter's recommendations and the numerical calculations, which indicated that the rotor losses increase with small rotor slot numbers.

The depth of a rotor tooth has a significant effect on the motor performance. It was shown with the time-harmonic 3D FEM that the flux and current densities have a different distribution on the surface of the rotor tooth and on the bottom of the rotor yoke when the depths of the rotor teeth and rotor yoke are changed. Additionally, the depth of the rotor yoke should be sufficient, and consequently, there is enough space to allow the flowing of the magnetic flux to the other pole. The time-harmonic 3D FEM does not give results that are absolutely accurate. With these 3D calculations, it is nevertheless possible to predict the flux density and current density distributions of the rotor teeth and rotor yoke. From the cost point of view, the rotor should be as thin as possible; however, the flux and current densities in the different parts of the rotor core define the limits for the depth of the rotor teeth and yoke. An objective of the 3D FEM calculations was to confirm that the flux and current density distribution are in an acceptable level, that is, inside the limits that Vogt (1996) has given for an asynchronous motor. According to the numerical calculations, the depth of the rotor teeth should be 20 mm and the depth of the rotor yoke at least 40 mm.

The 2D FEM calculation indicates that the harmonics cause a remarkable part of the rotor losses of the AFIM studied. The losses on the rotor surface were reduced by coating the rotor with suitable coating pads and a ring made of a material that forms a high surface impedance $\underline{Z}_s$. Three commercially available ferromagnetic materials with a poor conductivity were chosen. A low conductivity increases the depth of penetration, but a poorly conducting coating gives the same effect as the increasing of the air-gap – it smoothens the flux density distribution before the flux penetrates into the rotor core material. Another method to decrease the losses in the rotor surface is to reduce the rotor surface impedance by using a well-conducting coating layer. The well conducting coating layer studied with the 2D FEM was a copper ring. The thicknesses of the copper ring studied were 0.5, 1.5 and 2.5 mm.

The comparison of the effects of the copper coating ring and the ferromagnetic coating pads or rings on the rotor eddy current losses and the spectra of the flux densities on the rotor surface are presented in Figs. 3.18 and 3.19. The resistivity and permeability of the coating material are not equal to the corresponding values of the rotor core material. Thus, the torque produced by the fundamental flux wave tends to attenuate slightly, and the slip is increased in order to get the rated torque. The lowest slip and the slip-dependent rotor Joule losses are achieved when a copper-coated rotor is used. With the copper coating the harmonic losses in the rotor core are lower than in the case when the high-resistivity ferromagnetic material is used.

In solid-rotor-core induction motors, the minimization of the harmonics effects in the air-gap of the motor is a very significant means to reduce the additional losses. The flux distribution will be smoothened, and the losses in the stator and rotor cores decrease if the slot opening is narrowed. In all cases however, a longer air-gap and a narrowed slot opening may not be enough. The coated rotor is very capable of operating at higher rotation speeds, because the coating reduces the effects caused by the air-gap harmonics. The coating material may be

either electrically conducting or low-conducting. It is also desirable that the coating materials have a high value of thermal conductivity. In the case of the motor studied, the coating was fabricated from a material having a high resistivity. In that case, the surface impedance of the rotor increases, thus making the high-frequency air-gap harmonics to attenuate and smoothen before they penetrate into the rotor core material. Therefore, the eddy current losses caused by the permeance harmonics decrease and the rotor surface losses reduce as it was shown. It was also discovered that when the thickness of the coating material was increased, the rotor core losses decreased, and the rotor coating losses increased. To sum up, the lowest rotor total losses are achieved, when the thickness of the coating is 2.5 mm and the material 2 pads or copper ring is used.

4. Prototype machine and measurements

The results of the thesis are largely based on the extensive laboratory tests reported in this chapter. The practical measurements are in this case extremely important since the electromagnetic behaviour of the machine type cannot be evaluated accurately enough with the present tools. The results obtained by the design methods discussed here are compared with the measurement results. It is seen that the design principles introduced earlier are valid for finding the best performance for a solid-rotor-core axial-flux induction machine.

This chapter introduces the results of the laboratory measurements. The electromagnetic properties of the prototype motor were measured in the laboratory applying the IEEE 112 standard B method for sinusoidally fed poly-phase induction motors. In order to achieve as comparable results as possible between the measured and numerically calculated values, the motor should to be supplied directly from a sinusoidal voltage 200 Hz network. However, the motor has to be supplied with a frequency converter instead of a 200 Hz sinusoidal supply. Because there are no standards for frequency-converter-supplied induction motors, the IEEE 122 standard B method was also adopted in the measurements of the frequency-converter-supplied motor. With the load tests, the effects of the air-gap length, coating material resistivity, coating material thickness, the depths of the rotor yoke and the rotor teeth on the performance characteristics of the prototype motor were studied.

The prototype is not a result of any accurate optimization process, but its dimensions are based on the practical knowledge of AXCO-Motors Oy. The prototype machine represents an AF solid-rotor-core induction motor one-rotor-one-stator configuration. The stator windings are connected in star. The nominal power of the machine is 45 kW and the nominal no-load rotational speed 6000 min^{-1}. The motor has a 7/9 or 8/9-short-pitch double-layer stator winding. The parameters of the test motor are given in Table 4.1. More detailed data of the prototype AFIM are presented in Appendix C.

Table 4.1 Main parameters of the prototype motor.

parameter	explanation	value
P_n	nominal power	45 kW
n_n	nominal speed	6000 min^{-1}
s_n	nominal slip	1.0 per cent
T_n	nominal torque	75 Nm
U_n	nominal (line-to-line) voltage	400 V
I_{ph}	nominal phase current	115 A
w_{pad}	thickness of coating pad	1.5, 2.0, 2.5, 3.0 mm
δ	length of the air-gap	0.9, 1.4, 1.9 mm
w_{dr}	depth of the rotor tooth	15, 20 mm
w_{yr}	depth of the rotor yoke	30, 35, 40, 45 mm
Q_s	number of the stator slots	36
Q_r	number of the rotor slots	30
P	number of pole pairs	2
D_{se}	external diameter of the stator stack	310 mm
D_s	internal diameter of the stator stack	190 mm
N	number of coil turns in series per phase	36

The prototype machine mechanics was designed particularly for laboratory test use. The constructed motor frame allows changing the rotors, the stators and the air-gap length without any special equipment or machining of the parts. The rotor may be changed without changing the shaft, because the rotor disc is fixed to the shaft via a bolt joint.

The material of the stator core is fully processed electrical steel sheet M270-35A (Cogent power Ltd 2003) and the material of the rotor core is low-carbon steel Fe52. The material properties of the stator and the rotor materials are given later in this work. The stator strip of the prototype machine was manufactured of electrical steel sheet using by die-cutting method. The strip was then wound without any joints as a spiral to form the stator core with slots. The stator core is fixed to the frame by bolt joints. The stator lamination stacking-factor obtained with the fabrication process was as high as 0.98.

In the stator winding, the number of coils per pole and phase is three. Each of the phase coils includes six turns and the total number of phase turns is the 36. Both ends of the phase windings of the stator are available in a connection box. The rotor and the stator of the prototype are shown in Fig. 4.1 after winding.

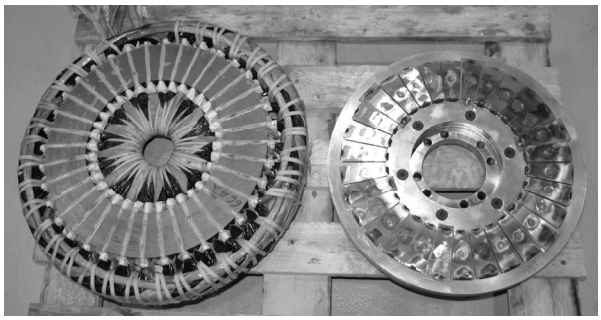

Fig. 4.1 Rotor and stator of the prototype motor after winding.

Four different commercially available rotor coating materials were studied to find out the influence of the rotor coating on the rotor eddy current loss. The coating arrangement on the surface of the rotor core is illustrated in Fig. 4.2. The aluminium winding is not included in the Figure. The material properties of the rotor coating materials are given later in this work.

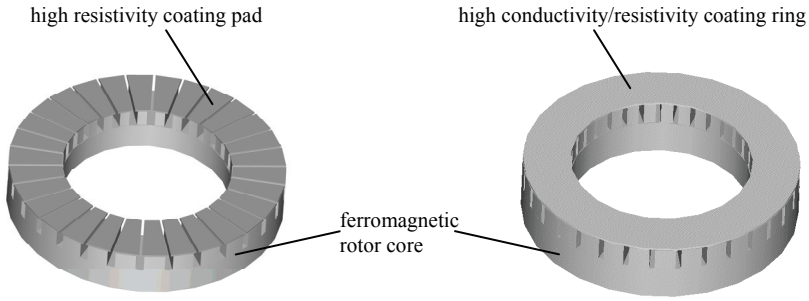

Fig. 4.2 Structures of a solid-rotor-core of the AFIM studied. Also the coating pads and rings are illustrated.

4.1 Measurement set-up

The measurement test set-up is described in Figs. 4.3 and 4.4. The prototype machine was fed by a variable-speed frequency converter (ABB ACS600 DTC converter in scalar mode) and loaded with a 1000 kW, 12000 min^{-1} solid-rotor induction machine. The main parameters of the frequency converter are given in Table 4.3. The shaft torque was measured by a torque transducer and the electrical power by a power analyzer, and the temperature was registered in three points by Pt-100 temperature sensors. The temperature values are stored up in a PC by a reading unit FlukeHydra. The torque transducer is connected via a reading unit Vibrometer to

a power analyzer Yokogawa PZ4000. PC collects the data from Yokogawa and from FlukeHydra. Table 4.2 shows the accuracies of the measurement devices. The GPI bus transfers and the computer handles the data in digital mode, in which the error should be negligible.

Table 4.2 Accuracies of the employed measurement devices.

Device	Accuracy [%]
Torque transducer: Vibrometer: TORQUEMASTER TM-214	0.2
Current transformer: GSA 120 A 50	0.2
Power analyser: Yokogawa PZ4000	0.1

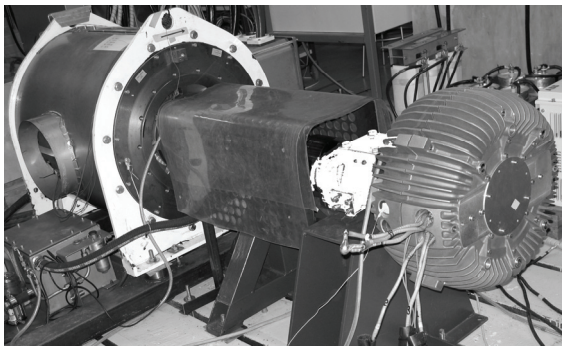

Fig. 4.3 Prototype machine in the test bench.

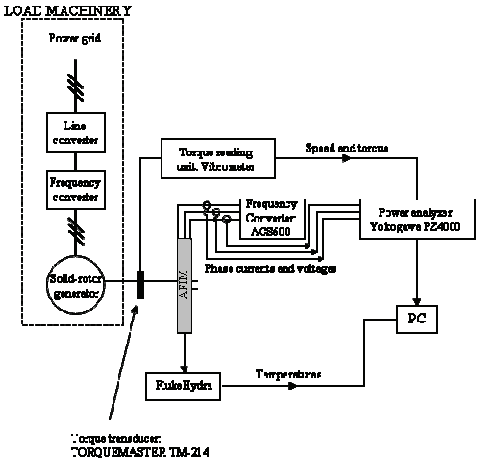

Fig. 4.4 Load test arrangement for the solid-rotor-core AFIM. The measured prototype motor was supplied by a frequency converter or alternatively directly from the 50 Hz network. The torque and the rotating speed were measured with a VIBRO METER TG-20 torque transducer. A YOKOGAWA PZ4000 power analyzer equipped with three current transformers measured the electric power. The waveforms of the supply are analyzed with YOKOGAWA PZ4000. One thermo-element was mounted in the stator windings, one was placed on the surface of the stator slot, and one on top of the stator tooth for temperature analyses. A FLUKE HYDRA 2620A measured the temperatures.

Table 4.3 Main parameters of the prototype motor.

Parameter	Value
Motor nominal line-to-line voltage	400 V
Motor nominal current	115 A
Motor nominal speed	5940 min^{-1}
Motor nominal frequency	200 Hz
Inverter switching frequency	4.0 kHz

4.2 Rotor and rotor coating pad materials

Carbon steel, such as Fe52, is a metal alloy containing some amount of carbon. The carbon content is harmful when considering the electromagnetic properties of the material. Nevertheless, Fe52 seems to be one of the most common types of steel used as a solid-rotor-core material. In fact, this is a conventional structure steel used widely in industry and constructions. Carbon is added to iron, because even with a low doping rate, it significantly improves the mechanic properties of the alloy. However, carbon increases the resistivity and decreases the saturation flux density of the material rather rapidly, yet low amount of carbon does not harm the *BH* curve too much for this purpose. In any case, the carbon content must be rather low (in the range of 0.2 %) to maintain decent electromagnetic properties.

The mechanical strength of Fe52 is high enough for medium-speed applications, and thus it can be used also in the prototype motor. Its drawback is the resistivity, which is quite high, thereby resulting in a relatively large slip of a purely solid-rotor motor, which in turn increases the fundamental rotor losses. In the case of the solid-rotor-core AFIM, the high resistivity, however, may be a benefit since the aluminium winding of the rotor constitutes the main current-carrying material of the rotor. The high core resistivity damps the eddy current losses in the core. In fact, a non-conducting ferromagnetic material should be ideal from this point of view. Such materials, however, are not available as steels. Pyrhönen (1991a) has analytically and experimentally studied the effects of the solid-rotor materials on the performance of a high-speed radial-flux smooth solid-rotor motor. The results obtained indicated that the highest torque may be reached with a material having a high saturation magnetic flux density and a good electrical conductivity. In this case, where the rotor current-carrying part and the core are manufactured as separate parts of different materials and where the rotor core is not the main current-carrying material, it could be stated that such a combination (steel and aluminium) satisfies well the desire of getting a high saturation and a good conductivity for the material.

The rotor core of the prototype motor studied in this work was manufactured by using low-carbon steel Fe52. The room temperature resistivity of the Fe52 is about 26.0 μΩcm and the temperature coefficient about 0.012 1/K. The virgin *BH* curve of Fe52 steel is shown in Fig. 4.5.

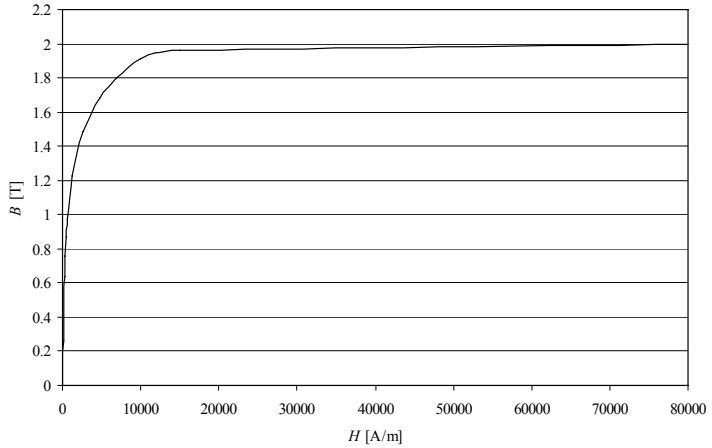

Fig. 4.5 Virgin *BH* curve of the ferromagnetic rotor material Fe52.

Four different materials were used as a rotor active surface coating material. One of these was the same low carbon steel Fe52. Other ferromagnetic materials, material 1 and material 2, were also commercially available ferromagnetic materials. The effects of the copper coating ring on the motor performance were also studied with the numerical calculations. Table 4.4 shows the ratios of the resistivities of the materials

Table 4.4 Ratios of the coating materials and the material Fe52.

material	ρ	$\rho_{\text{core}} / \rho_{\text{coating}}$
Fe52	0.26 μΩm	1
material 1	0.80 μΩm	3.08
material 2	1.20 μΩm	4.60
copper	0.018 μΩm	0.07

The magnetic properties of the coating materials, the material 1 and material 2, are shown in Figs. 4.6 and 4.7.

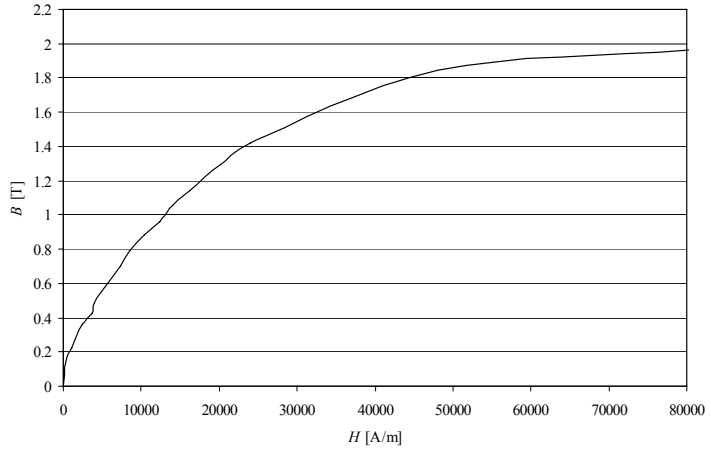

Fig. 4.6 Virgin *BH* curve of the ferromagnetic rotor coating material 1.

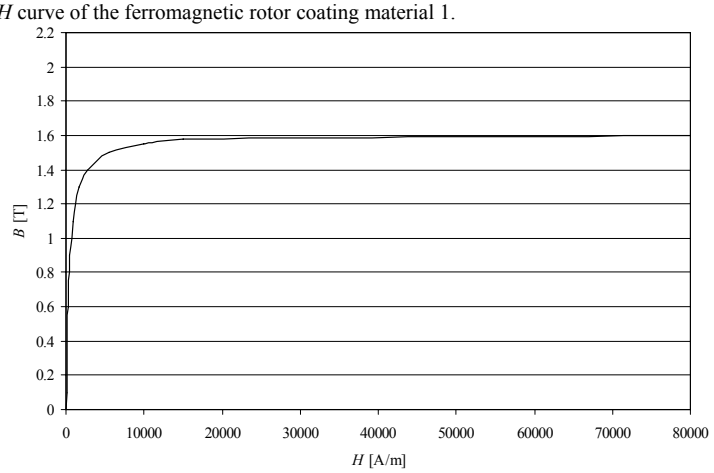

Fig. 4.7 Virgin *BH* curve of the ferromagnetic rotor coating material 2.

The material 1 is a special steel, which is extremely hard but may also be quite brittle. The electrical resistivity of the material 1 is relatively high. Its initial permeability is low but the

saturation flux density is high. The material 2 is a steel that is stronger and harder than most steels. The material 2 has a high resistivity and somewhat lower saturation flux density than the other materials mentioned. Its initial permeability is also far higher than that of the material 1.

At no-load, the air-gap flux penetrates the rotor normal to the surface. Since the maximum sinusoidal air-gap flux densities of AFIMs may be in the range of 1 T, one might assume that the saturation flux density of the coating pad material could be satisfactory when being larger than 1 T. During high torque, however, part of the flux penetrates the rotor surface tangentially and the sum flux densities might be locally remarkably higher than the no-load maxima. Keeping these in mind, the materials 1 and 2 should well fulfil the coating function. The low initial permeability of the material 1 somewhat increases the no-load magnetizing current. The high initial permeability and satisfactorily high saturation flux density of the material 2 should be a desirable property combined with the very high resistivity of the material.

Pads manufactured of the above mentioned materials were attached onto the rotor core after inserting the rotor aluminium winding. The rotor winding was manufactured by punching high yield strength aluminium "cages" of aluminium plate having about 80 % of the conductivity of pure aluminium.

4.3 No-load test

The no-load tests were performed using both sinusoidal network and frequency converter supplies. The no-load test using sinusoidal 50 Hz voltage was performed to evaluate the iron loss and the mechanical loss in no-load conditions. In this method of evaluating the iron loss values the harmonic losses caused by the inverter supply are not considered. The ambient temperature in the laboratory was kept constant, and thus the no-load tests were carried out in each case with a cold motor. The input power is equal to the sum of the no-load motor losses. Subtracting the stator ohmic loss from the input gives the sum of the friction, aluminium cage and core losses. In the test the motor air-gap length was selected to be δ = 1.4 mm. Figure 4.8 shows the measured values for the AFIM studied.

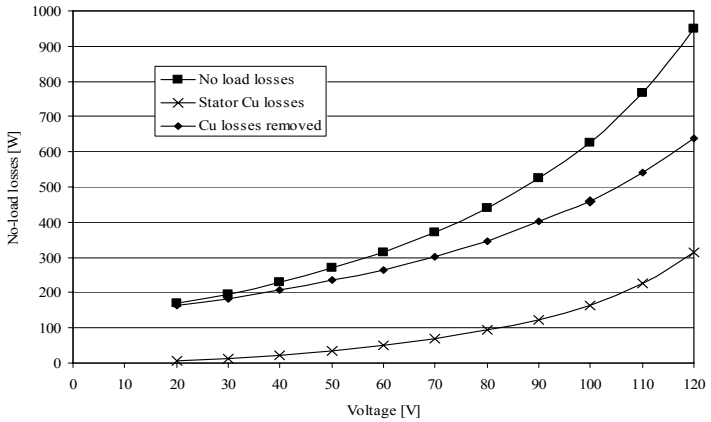

Fig. 4.8 Measured no-load loss values as a function of line-to-line voltage using sinusoidal 50 Hz voltage. The rotor core material was Fe52 and the coating material was the material 1. The thickness of the coating was 2.5 mm and the air-gap length 1.4 mm. The motor rated flux is reached at 100 V at 40 A no-load current.

Since the harmonics caused by a frequency converter produce a great amount of eddy current losses on the solid-rotor steel and the aluminium cage, the no-load test was performed also using frequency converter supply (50 Hz, 100 V): the test shows the influence of the frequency converter PWM pattern on the iron losses. Figure 4.9 shows the no-load losses as a function of supply voltage.

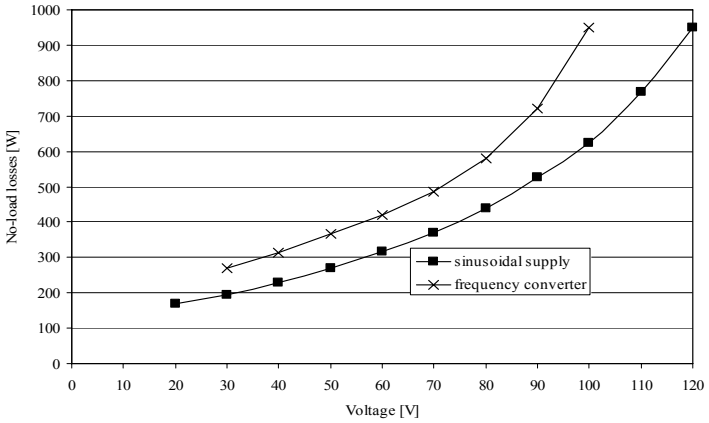

Fig. 4.9 Measured no-load loss values as a function of line-to-line voltage using sinusoidal voltage and frequency converter supplies. The material 1 was used as the rotor coating material and the rotor core material was Fe52. The thicknesses of the air-gap and the rotor coating were 2.5 and 1.4 mm, respectively. The parameters of the frequency converter were: motor nominal voltage (0.2–1.0) · U_n/4, supply fundamental frequency 50 Hz.

The mechanical losses in sinusoidal voltage supply at the nominal flux point of the motor 1500 min^{-1} (50 Hz) 100 V (line-to-line voltage) are about 100 W, the core losses 460 W, and the stator Cu losses 170 W. The frequency converter PWM supply increases the losses of the motor. At the nominal flux point (50 Hz, 100 V), there are about 350 W more no-load losses compared with the sinusoidal voltage supply when using the rotor coating material 1 with 1.4 mm air-gap.

At the rated voltage inverter supply (200 Hz, 400 V, 6000 min^{-1}) the no-load losses of the same 45 kW motor configuration were 1832 W, which was divided in friction 390 W, copper 212 W and iron losses 1230 W.

4.4 Effects of the air-gap length

The length of the air-gap of a motor has a significant influence on the characteristics of an electrical machine. For instance, the air-gap length plays an important role when the flux harmonics on the surface of the rotor are studied. In the case of the prototype motor, the constructed motor frame allows changing the air-gap length without a need for excessive machinery. Three-different air-gap lengths: 0.9, 1.4 and 1.9 mm were studied. The same rotor-stator constructions were used in all measurements. The rotor was coated with a high-resistivity material, the material 1, introduced earlier in this chapter. The thickness of the coating layer was 2.5 mm. There were semi-closed slots in the stator.

The prototype motor was supplied with a frequency converter, giving the motor a supply voltage of 400 V and a supply frequency 200 Hz, and with a sinusoidal 50 Hz network supply. To keep the air-gap flux at a constant rated value while the supply frequency was reduced from 200 Hz to 50 Hz, the supplied voltage was reduced from 400 V to 100 V (line-to-line

voltage). Figure 4.10 shows the efficiency, power factor, and slip of the motor as a function of torque when 200 Hz frequency converter supply was used.

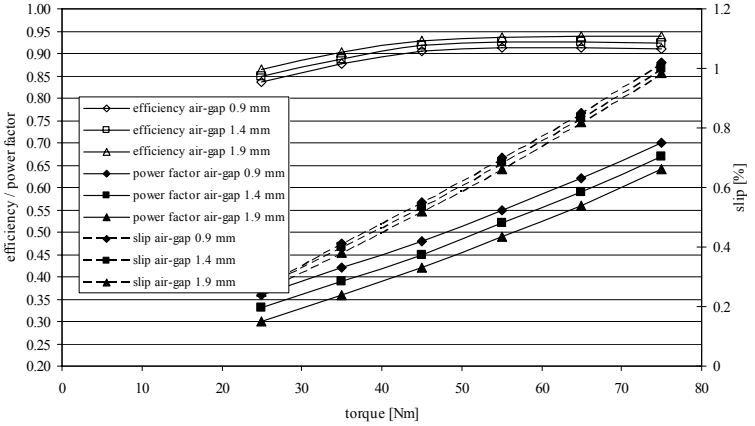

Fig. 4.10 Efficiency, power factor, and slip as a function of motor torque. The length of the air-gap was set to be 0.9, 1.4, and 1.9 mm. The load test was performed by using a frequency converter supply (U_n = 400 V, f_n = 200 Hz, f_{sw} = 4 kHz). The rotor coating material 1 and rotor core material Fe52 was applied. The thickness of the coating pad was 2.5 mm. In the stator, semi-magnetic slot wedges and double-layer 7/9-short pitch windings were used.

The effects of the air-gap length on the efficiency, power factor, slip, and stator current of the motor characteristics at the nominal torque 75 Nm of the motor are illustrated in Fig. 4.11. Both frequency converter and sinusoidal 50 Hz network supplies were used.

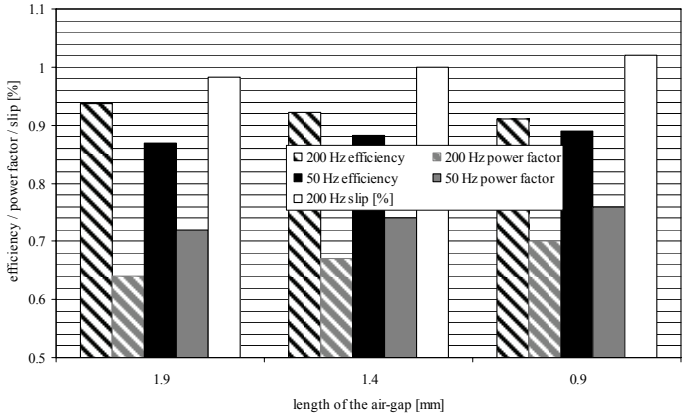

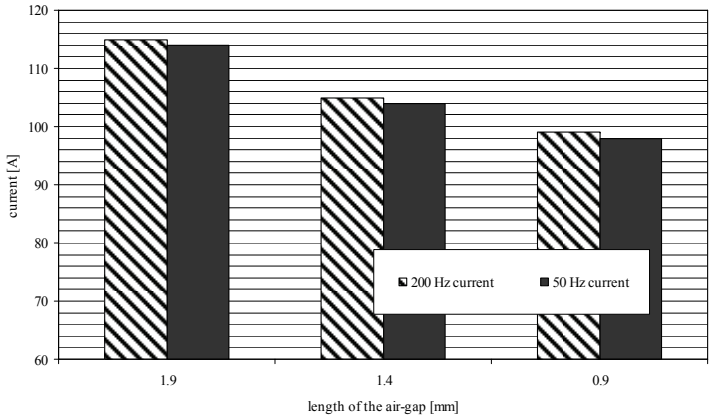

Fig. 4.11 Efficiency, power factor, slip, and stator current as a function of air-gap length at the point of motor nominal torque 75 Nm. The load test was performed by using a frequency converter supply (U_n = 400 V, f_n = 200 Hz, f_{sw} = 4 kHz) and sinusoidal 50 Hz and 100 V (line-to-line) voltage supply. 1.9, 1.4 and 0.9 mm air-gap lengths were used in the measurements. The rotor core material Fe52 and coating material 1 was applied. The thickness of the rotor coating pads were 2.5 mm. Semi-magnetic slot wedges and double-layer 7/9-short pitch windings were used. When sinusoidal 50 Hz voltage supply was applied and the length of the air-gap was decreased from 1.9, 1.4, and 0.9 mm, the slip values were 3.7, 3.7, and 3.8 per cent, respectively. The fundamental RMS current values are presented in the illustration; the fundamental phase voltage RMS value was approximately 230 V (400 V line-to-line) in the case of the frequency converter 200 Hz supply.

An efficient method to reduce the effects of the permeance harmonics that are mainly caused by the stator slotting on the rotor surface is to increase the air-gap length. A long air-gap smoothens the flux density distribution on the rotor surface, but also increases the magnetizing current of the motor and leads to larger stator copper losses. When the frequency converter supply was used and the length of the air-gap was decreased from 1.9 to 0.9 mm, the efficiency decreased from 94 to 91 per cent, the power factor increased from 0.64 to 0.70, and the magnetizing current and thus the stator copper losses also decreased, as was illustrated in Fig. 4.11. In the case of 50 Hz sinusoidal supply, the efficiency was increased from 87.0 per cent to 89.0 per cent, the power factor increased from 0.72 to 0.76, and the stator copper losses were also approximately decreased as was shown in Fig. 4.11 when the length of the air-gap was decreased from 1.9 to 0.9 mm.

The winding harmonic and the permeance harmonic losses can be reduced by decreasing the effects of the air-gap harmonic on the rotor surface. By increasing the air-gap length, the effects of these harmonics can be reduced effectively. This is clearly demonstrated by the measurement results. When 50 Hz sinusoidal supply was used, the efficiency of the motor was mainly depended on the stator copper losses, and of course the larger slip caused losses. However, when the frequency converter supply was used and the length of the air-gap was increased, the efficiency of the motor was increased despite the fact that the stator copper losses increased. This shows that the efficiency of the motor is dependent on the rotor eddy current losses when higher rotation speeds are used. These eddy current losses on the rotor can be reduced effectively by increasing the air-gap length.

4.5 Effect of the depth of the rotor teeth

The effects of the depth of the rotor teeth on the motor characteristics have been analyzed by load tests. The axial length of the rotor was shortened by cutting the rotor teeth. Two-different rotor teeth depths, 20 and 15 mm, were used. The same stator was used in all measurements.

The material 2, presented earlier in this chapter, was used as a rotor coating material. The thickness of the rotor coating pad was 2.5 mm. The stator slots were closed with semi-magnetic slot wedges.

The targeted air-gap length was 1.4 mm in both measurements. Unfortunately, because of mechanical reasons, it was not possible to keep the air-gap length exactly the same after the rotor was shortened. When the depth of the rotor teeth was 20 mm, the air-gap length was set at 1.4 mm. After the rotor was shortened by cutting the rotor teeth from 20 mm to 15 mm, the length of the air-gap was somewhat longer, approximately 1.7 mm. This disadvantageous is deplorable, and causes inaccuracy in the comparison of the depth of the rotor teeth on the motor performance characteristics, in particular because the air-gap length has a significant influence on the performance of the studied motor, as it was shown before.

The prototype motor was supplied with a frequency converter having a supply voltage of 400 V and a supply frequency of 200 Hz, and also with sinusoidal 50 Hz network supply. The purpose was to determine the efficiency, fundamental power factor and slip as a function of motor torque. Figure 4.12 shows the efficiency, power factor, and slip of the motor as a function of torque when the frequency converter supply was used.

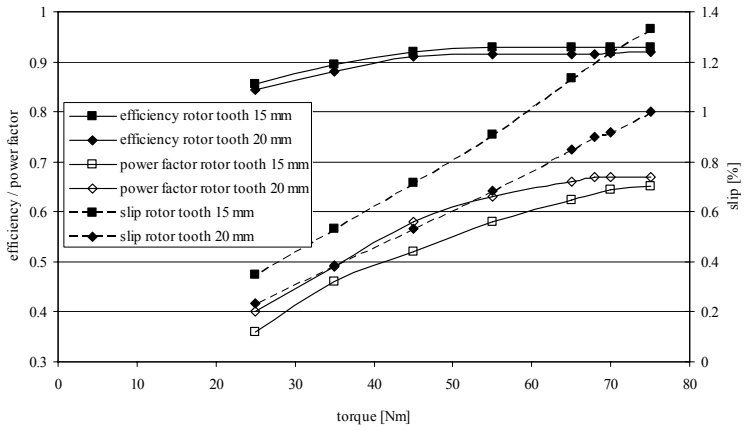

Fig. 4.12 Efficiency, power factor, and slip of the motor as a function of the torque. The depth of the rotor teeth was set to be 20 and 15 mm. The load test was performed by using a frequency converter supply (U_n = 400 V, f_n = 200 Hz, f_{sw} = 4 kHz). The rotor core material was Fe52 and coating material was material 2. The thickness of the rotor coating pad was 2.5 mm and the air-gap length 1.4 mm with 20 mm deep rotor bars and 1.7 mm with 15 mm bars. Double-layer 8/9-short pitch windings and semi-magnetic slot wedges were used in the stator.

The effects of the rotor teeth depth on the efficiency, power factor, slip, and stator current of the motor at the nominal torque 75 Nm of the motor are illustrated in Fig. 4.13. Both frequency converter and sinusoidal 50 Hz network supplies were used.

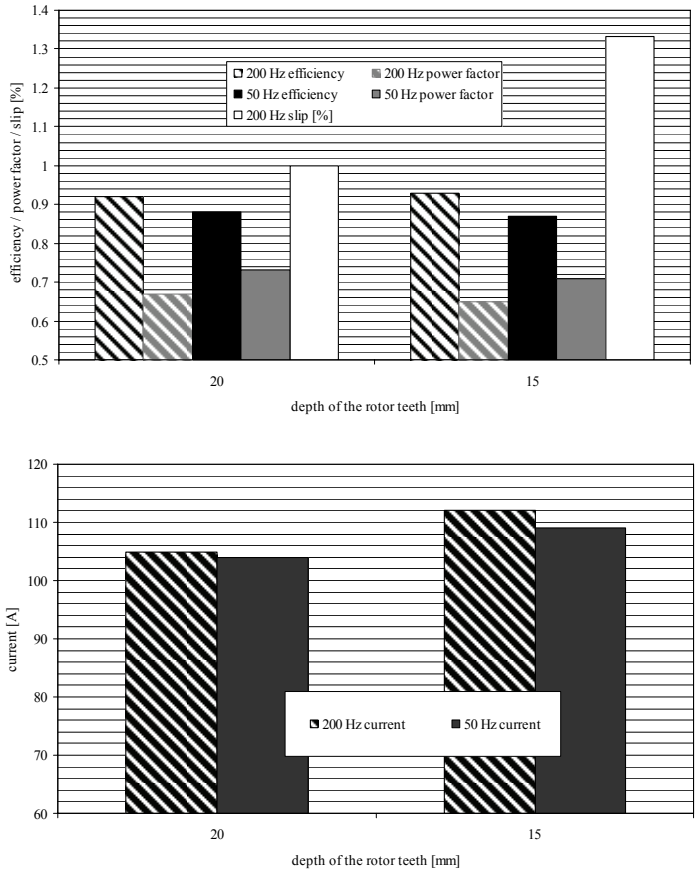

Fig. 4.13 Efficiency, power factor, slip, and stator current as a function of rotor teeth depth at the point of motor nominal torque 75 Nm. The load test was performed by using a frequency converter supply (U_n = 400 V, f_n = 200 Hz, f_{sw} = 4 kHz) and sinusoidal 50 Hz, 100 V (line-to-line) voltage supply. 20 and 15 mm rotor teeth lengths were used. The rotor core material was Fe52 and the rotor coating material 2 was applied. The thickness of the coating pads were 2.5 mm and the air-gap length 1.4 mm with 20 mm deep rotor bars and 1.7 mm with 15 mm bars. In the stator, double-layer 8/9-short pitch windings and semi-magnetic slot wedges were applied. Decreasing the amount of aluminium in the rotor remarkably increases the rotor resistance and the slip. The considerable difference between efficiencies when 50 Hz sinusoidal supply was used can be explained by the higher stator copper losses caused by longer air-gap length and higher slip-dependent rotor Joule losses. When sinusoidal 50 Hz voltage supply was applied and the depth of the rotor teeth was decreased from 20 mm to 15 mm, the slip was increased from 3.8 to 5.9 per cent. The fundamental RMS current values are presented in the illustration; the fundamental phase voltage RMS value was approximately 230 V (400 V line-to-line) when the frequency converter supply was used.

From the cost point of view, the rotor is more expensive, the more aluminium there is in the rotor core. Consequently, it is very interesting to define if it is electromagnetically possible to use shorter rotor teeth. The main target of this measurement was to determine the effects of the rotor teeth depth on the performance of the studied AFIM. It was known that longer rotor teeth give a smaller slip, and thus minor slip-dependent rotor Joule losses. A smaller slip is achieved because there is more aluminium in the rotor, and thereby the rotor resistance is lower. Additionally, the saturation of the rotor teeth is lower with small slip values, and hence the power factor of the motor should be better.

As it was mentioned before, the air-gap length was not exactly the same in the measurements (1.4 mm with 20 mm teeth and 1.7 mm with 15 mm teeth). This causes inaccuracy in the measurement results, especially when the frequency converter supply is used. The efficiency value with 15 mm teeth should have been slightly lower, and the power factor value somewhat higher at the frequency converter supply with the correct 1.4 mm air-gap value. Nevertheless, the change in the slip value at 200 Hz supply is considerable. It is natural that the slip value increases significantly when the rotor resistance increases, as the depth of the rotor teeth decreases. This relates to the quantity of the aluminium in the rotor. The slip-dependent rotor Joule losses increase when the depth of the rotor teeth decreases from 20 to 15 mm. If the length of the air-gap had been the same in both (15mm/20mm teeth) measurements, the 15 mm efficiency could have been somewhat lower, because a 1.4 mm air-gap produces larger harmonic losses on the rotor than a 1.7 mm air-gap.

4.6 Effects of the depth of the rotor yoke

When considering a solid-rotor yoke, the determination of the thickness of the yoke is not a very straightforward task. The slip frequency easily causes eddy currents in the rotor yoke, and the flux distribution is highly slip dependent. Hence, the eddy current behaviour at operating slip values has a major influence on the sensible dimensioning of the yoke. The original 45 mm rotor yoke thickness was selected according to the analytical design process presented in Chapter 2. The 45 mm rotor yoke thickness was selected according to 1.3 T flux density value at the yoke at the geometric average radius of the rotor.

The effects of the depth of the rotor yoke on the motor characteristics have been analyzed by load tests. The axial length of the rotor was shortened by cutting of the rotor yoke. Four different lengths of the rotor yoke were used in the measurements 45, 40, 35 and 30 mm. The depth of the rotor teeth was 15 mm, and the air-gap length was kept at 1.7 mm. The thickness of the rotor coating pad was 2.5 mm and the coating material 2 was used.

The prototype motor was supplied with a frequency converter (U_n = 400 V f_n = 200 Hz) and with a sinusoidal 50 Hz network supply. While the supply frequency was reduced from 200 Hz to 50 Hz, the supplied voltage was reduced from 400 V to 100 V to keep the air-gap flux at a constant rated value. The purpose was to determine the efficiency, fundamental power factor and slip as a function of motor torque. Figure 4.14 shows the efficiency, power factor, and slip of the motor as a function of torque when a frequency converter supply was used.

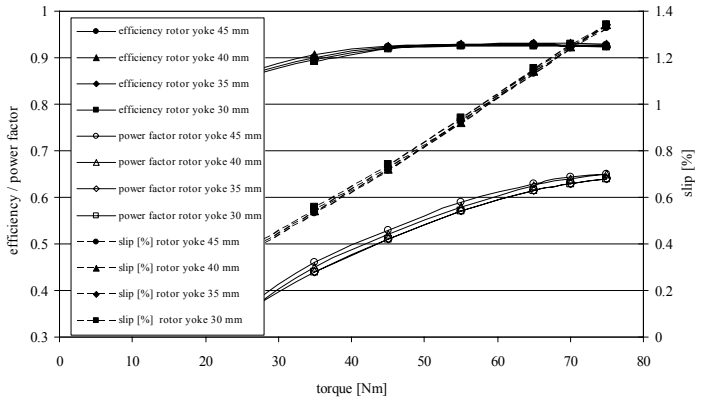

Fig. 4.14 Efficiency, power factor and slip of the motor as a function of motor torque. The depth of the rotor yoke was set at 45, 40, 35 and 30 mm. The load test was performed by using a frequency converter supply (400 V, 200 Hz, f_{sw} = 4 kHz). The depth of the rotor teeth was 15 mm and the rotor coating material number 2 was applied. The rotor core material was Fe52. The length of the air-gap was 1.7 mm and the thickness of the rotor coating pad 2.5 mm. In the stator, double-layer 8/9-short pitch windings and semi-magnetic slot wedges were applied.

Figure 4.15 shows the efficiency, power factor, slip, and stator current as a function of the depth of the rotor yoke at the point of the nominal torque 75 Nm of the motor. The prototype motor was supplied at 200 Hz with the frequency converter and with 50 Hz network.

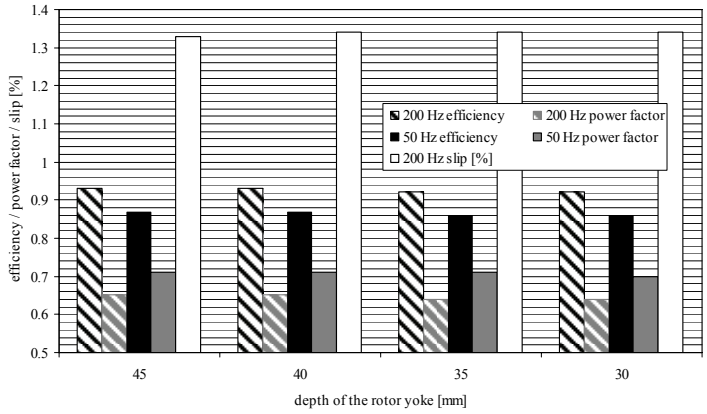

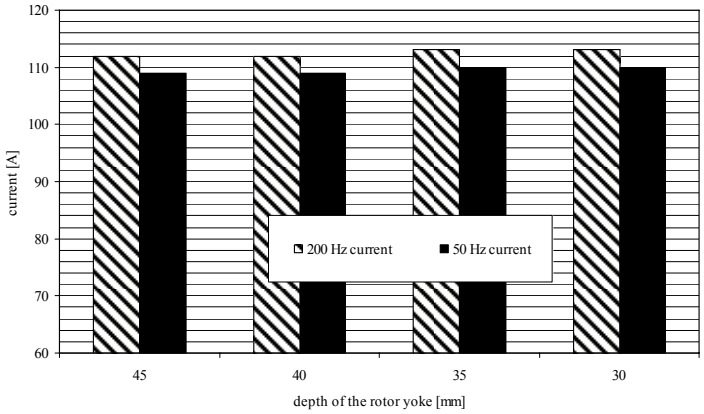

Fig. 4.15 Efficiency, power factor, slip, and stator current of the motor as a function of the depth of the rotor yoke at the point of the nominal torque 75 Nm of the motor. 45, 40, 35 and 30 mm rotor yoke length were used. The load test was performed by using a frequency converter supply (400 V, 200 Hz, f_{sw} = 4 kHz) and a sinusoidal 50 Hz, 100 V (line-to-line) voltage supply. The depth of the rotor teeth was 15 mm and the material 2 was used as a coating material. The rotor core material was Fe52. The length of the air-gap and the thickness of the rotor coating pads were 1.7 and 2.5 mm. In the stator, double-layer 8/9-short pitch windings and semi-magnetic slot wedges were applied. When sinusoidal 50 Hz voltage supply was applied and the depth of the rotor yoke were changed to 45, 40, 35, and 30 mm, the slip was changed by 5.9, 5.9, 6.0, and 6.0 per cent. The fundamental RMS current values are presented in the illustration. The fundamental phase voltage RMS value was approximately 230 V (400 V line-to-line) when the frequency converter supply was used.

When the frequency converter supply was used, the highest efficiency value was achieved when 40 mm rotor yoke depth was used. There were no significant changes in the slip, and the power factor decreased by about 1.5 per cent when the length of the rotor yoke was changed from 45 to 30 mm at the point of motor nominal torque 75 Nm. In the case of 50 Hz network supply, there were no significant differences in the efficiency, power factor, and slip values at the point of motor nominal torque 75 Nm when the depth of the rotor yoke was changed. However, both the efficiency and power factor values decreased.

The measurements indicate that when the depth of the rotor yoke was decreased, the efficiency of the motor also decreased after it had reached its maximum. This effect was detected both with the frequency converter and sinusoidal network supplies. The conclusion is that the saturation of the rotor yoke increases when the depth of the rotor yoke decreases. The optimum efficiency value is achieved when the depth of the rotor yoke is 40 mm. However, the best power factor and the lowest stator current values are achieved when the depth of the rotor yoke is 45 mm.

4.7 Effects of the thickness and the resistivity of the rotor coating pads

A solution for reducing the rotor surface losses is to coat the solid-rotor-core with a proper material with a properly selected coating layer thickness. The prototype machine was coated with materials having three different resistivities. One of the coating materials was Fe52, which is the same material that was used in the rotor core. Two other materials were also commercially available materials, the materials 1 and 2, introduced earlier in this chapter. Additionally, four different coating pad thicknesses 1.5, 2.0, 2.5 and 3.0 mm were used in the measurements. In these load tests, the coating material used was Fe52. The air-gap length was kept at 1.4 mm, and the depths of the rotor teeth and rotor yoke were 20 and 45 mm.

The thickness of the rotor coating pads on the performance of the studied AFIM was analyzed with time-stepping 2D FEM. The flux lines, flux density distributions, and eddy current density distributions shown in Fig. 4.16 are described at the nominal slip of the motor (s_n = 1.0 per cent). Four different coating layer thicknesses a) 1.5, b) 2.0, c) 2.5, and d) 3.0 mm were applied and the coating material 1 pads were used.

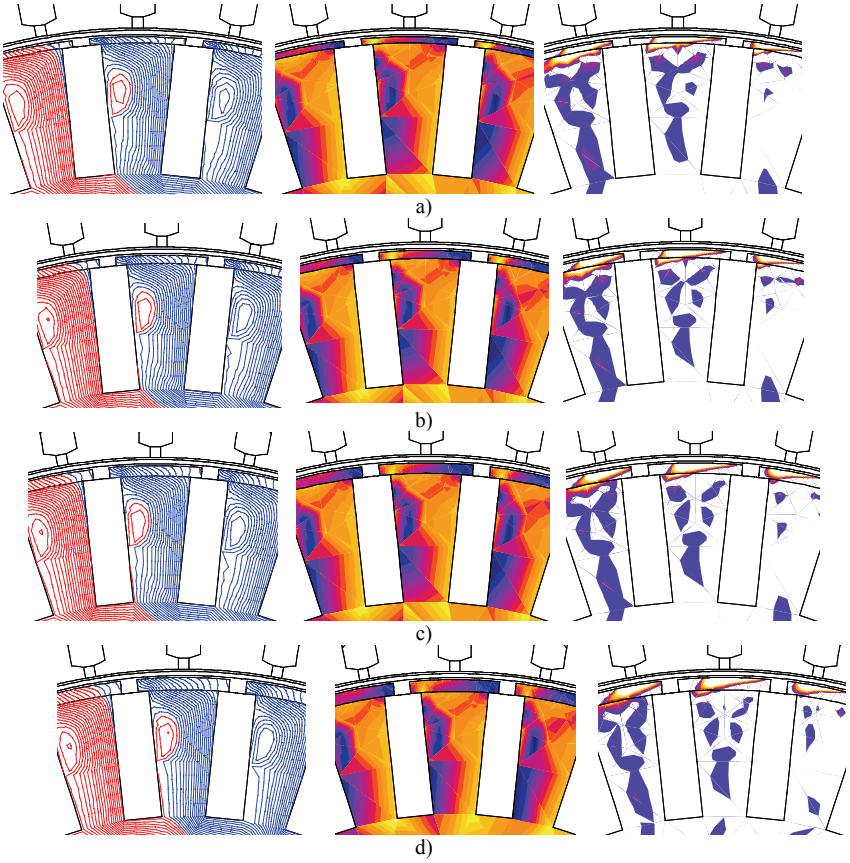

Fig. 4.16 Flux lines, flux density distributions and eddy current density distributions on the rotor core and coating at the nominal slip of the motor were studied with time-stepping 2D FEM. The thicknesses of the rotor coating were a) 1.5, b) 2.0, c) 2.5, and d) 3.0 mm. The material 1 pads were applied as a rotor coating material and the material of the rotor core was Fe52. The air-gap length was 1.4 mm and the depth of the rotor teeth was 20 mm. Semi-magnetic slot wedges and a double-layer 7/9-short-pitch winding were applied in the minimization of the harmonic eddy current losses. The lowest eddy current losses in the rotor were achieved when 3.0 mm thick rotor coating was used. The supply voltage and frequency were 400 V and 200 Hz. At the nominal slip of the motor, rotor losses increased around 3.0, 8.0 and 9.0 per cent units when the thickness of the coating pads were 2.5, 2.0, and 1.5 mm, respectively. The losses in 3.0 mm thick coating material were used as a reference value. The flux densities vary between 0.0 and 2.5 Tesla and the current density varies between 0.0 and 10.0 A/mm^2

The resistivity of rotor coating pads on the performance of the studied AFIM was analyzed with time-stepping 2D FEM. The flux lines, flux density distributions, and eddy current density distributions shown in Fig. 4.17 are described at the nominal slip of the motor (s_n = 1.0 per cent). Coating layers a) Fe52 pads, b) material 1 pads, c) material 2 pads, d) material 2 ring, and e) copper ring were applied and the coating material thickness 2.5 mm was used.

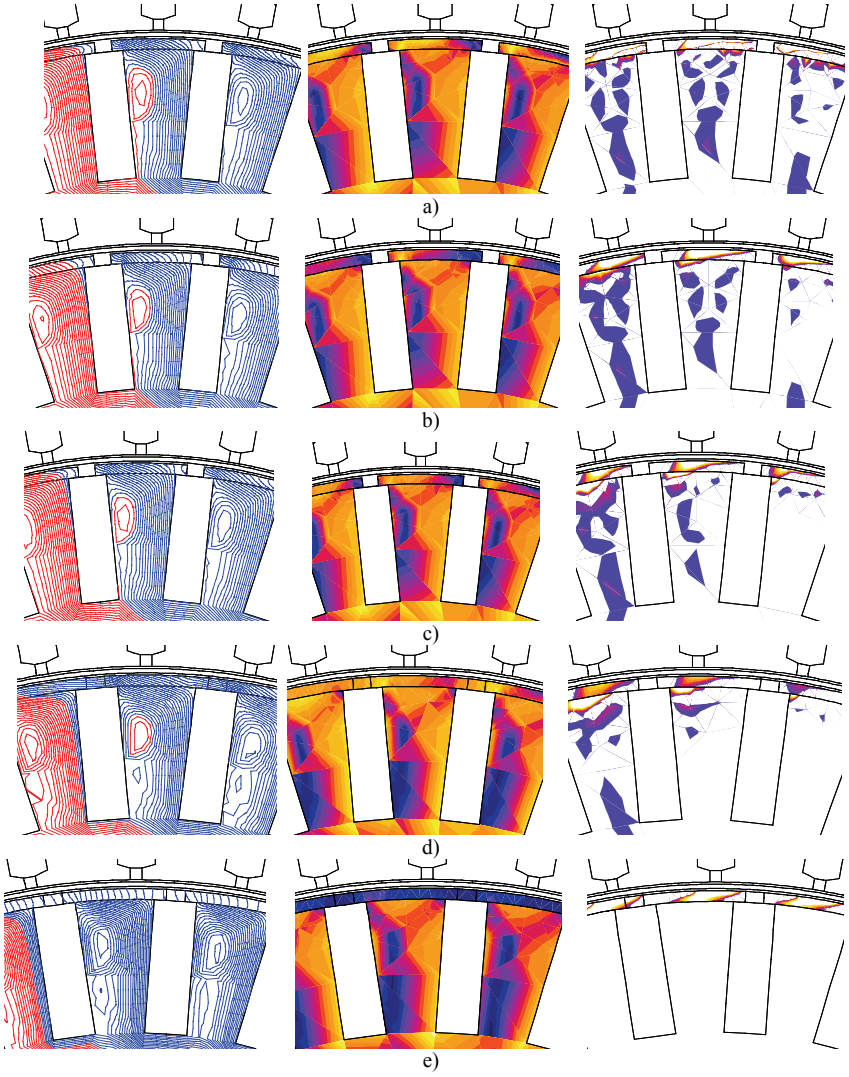

Fig. 4.17 Flux lines, flux density distributions and eddy current densities (from left to right) in the rotor at the nominal slip of the motor. The materials of the rotor coating pads were a) Fe52, b) the material 1, c) the material 2, and the materials of the rotor coating rings were d) the material 2, and e) copper. The rotor core material was Fe52. Rotor coating thickness 2.5 mm was applied. The air-gap length was 1.4 mm and the depth of the rotor teeth was 20 mm. Semi-magnetic slot wedges and a double-layer 7/9-short-pitched winding were applied in the minimization of the harmonic eddy current losses. The supply voltage and frequency were 400 V and 200 Hz. At the nominal slip of the motor, rotor losses increased by around 4.0 and 45.0 per cent units when the coating material was the material 1 and Fe52. Losses in the material 2 were used as a reference value. From a) to e) the flux densities vary between 0.0 and 2.5 Tesla. From a) to d) the current density varies between 0.0 and 10.0 A/mm^2 and in Fig. e) the current density varies between 0.0 and 20.0 A/mm^2. The corresponding loss distribution of the rotor with different coating materials and constructions were presented in Fig. 3.18. Measurements were carried out for the coating pads shown in a), b), and c), but measurements were not carried out for the coating rings shown in d) and e).

The load test was performed by using a frequency converter supply (U_n = 400 V, f_n = 200 Hz) and a 50 Hz sinusoidal network supply. The load tests were carried out to determine the effects of the coating material resistivities and thicknesses on the motor efficiency, power

factor, and slip. Figures 4.18 and 4.19 show the efficiency, power factor and slip of the motor as a function of torque when the frequency converter supply was used.

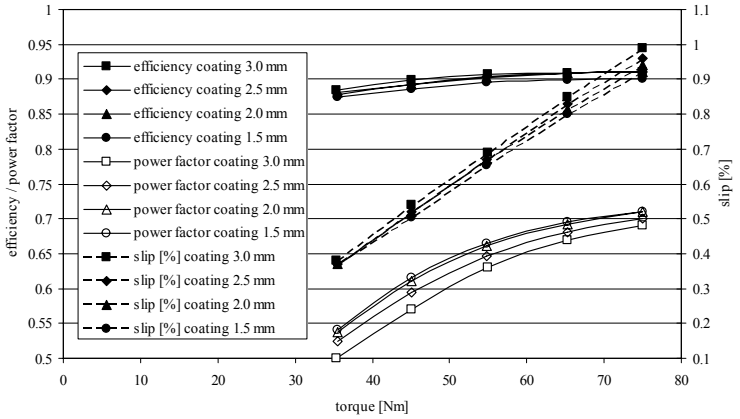

Fig. 4.18 Efficiency, power factor and slip of the motor as a function of motor torque. The rotor core and coating material was Fe52 and the thicknesses of the rotor coating pads were 3.0, 2.5, 2.0 and 1.5 mm. The length of the air-gap and depth of the rotor teeth were 1.4 mm and 20 mm. 7/9-short pitch windings and semi-magnetic slot wedges were used in the stator. The load test was performed by using a frequency converter supply (U_n = 400 V, f_n = 200 Hz, f_{sw} = 4 kHz).

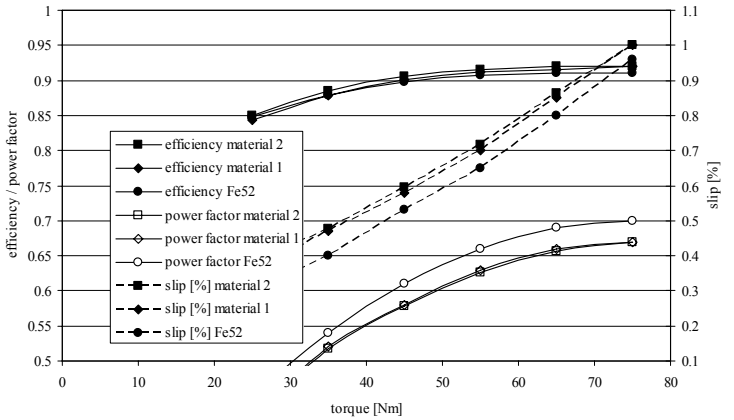

Fig. 4.19 Efficiency, power factor and slip of the motor as a function of motor torque. The thickness of the coating pads were 2.5 mm in all measurements. Three different coating materials Fe52, material 1, and material 2 were used in the measurements. The rotor core material was Fe52. The load test was performed by using a frequency converter supply (U_n = 400 V, f_n = 200 Hz, f_{sw} = 4 kHz). The air-gap length was 1.4 mm, and the depth of the rotor teeth 20 mm. 7/9-short pitch windings and semi-magnetic slot wedges were used in the stator.

The effects of the coating pad thicknesses and resistivities on the efficiency, power factor, slip, and stator current on the motor characteristics at the point of the motor nominal torque are illustrated in Figs. 4.20 and 4.21. Both frequency converter (U_n = 400 V, f_n = 200 Hz, f_{sw} = 4 kHz) and sinusoidal 50 Hz network supplies were used.

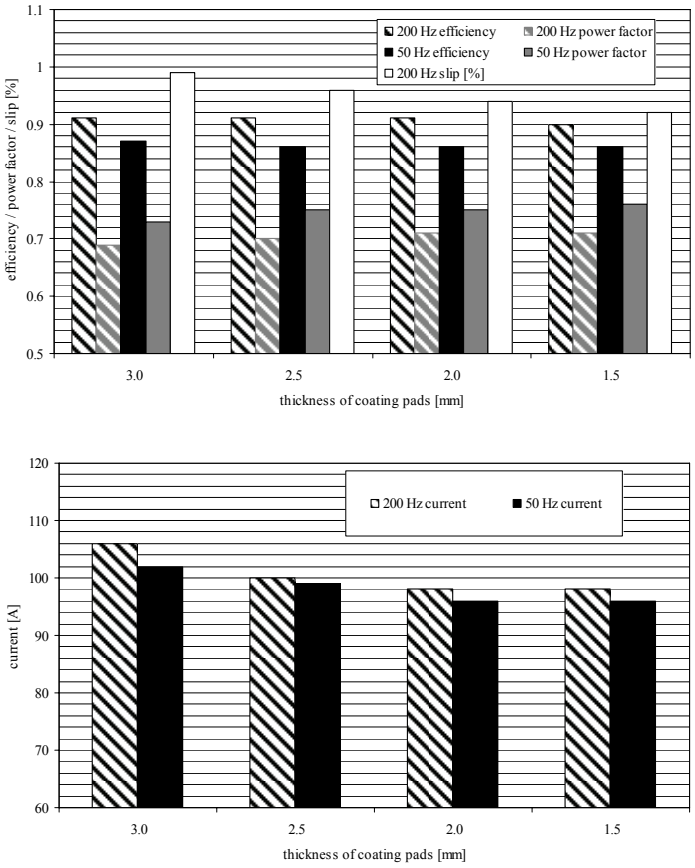

Fig. 4.20 Effects of the rotor coating pad thicknesses on the efficiency, power factor, slip, and stator current at the point of nominal torque of the motor as a function of coating pad thickness. The thicknesses of the rotor coating pads were 3.0, 2.5, 2.0 and 1.5 mm. The coating pad and rotor core material was construction steel Fe52. The air-gap length was 1.4 mm and the depth of the rotor teeth 20 mm. The load test was performed by using a frequency converter supply (400 V, 200 Hz, f_{sw} = 4 kHz) and sinusoidal 50 Hz, 100 V (line-to-line) voltage supply. Double-layer 7/9-short pitch windings and semi-magnetic slot wedges were used in the stator. The fundamental RMS current values are presented in the illustration; the fundamental voltage value in the case of frequency converter supply was approximately 230 V (400 V line-to-line).

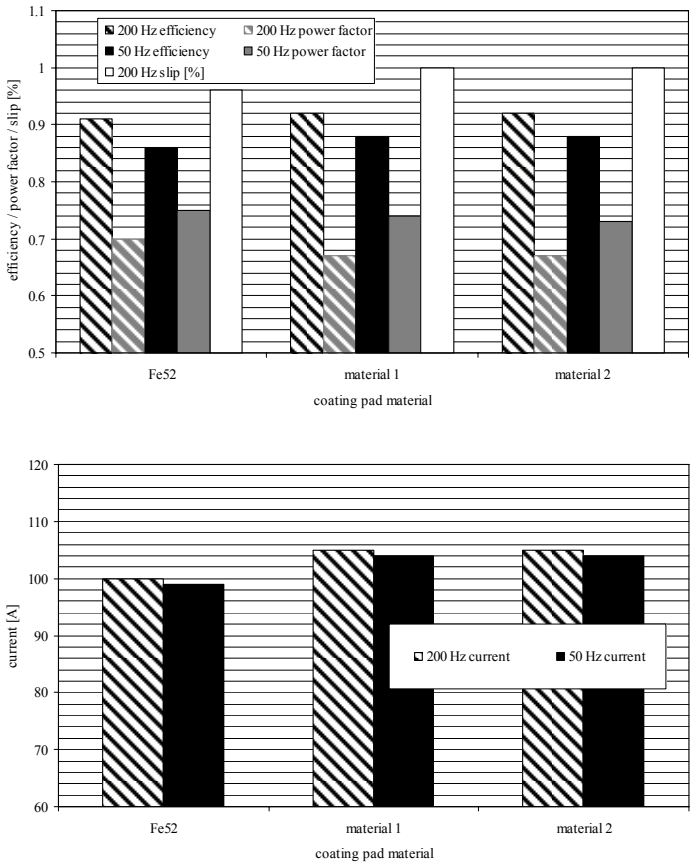

Fig. 4.21 Effects of the rotor coating layer resistivities on the efficiency, power factor, slip, and stator current at the point of the nominal torque of the motor as a function of different coating pad resistivities. Materials Fe52, material 1, and material 2 were used as a coating pad material. The thickness of the coating pad was 2.5 mm in all measurements. The load test was performed by using a frequency converter supply (400 V, 200 Hz, f_{sw} = 4 kHz) and sinusoidal 50 Hz, 100 V (line-to-line) voltage supply. The air-gap length was 1.4 mm and the depth of the rotor teeth 20 mm. Double-layer 7/9-short pitch windings and semi-magnetic slot wedges were used in the stator. The fundamental RMS current values are presented in the illustration; the fundamental phase voltage RMS value was approximately 230 V (400 V line-to-line) when the frequency converter supply was used.

An efficient method to reduce the surface losses is to increase the air-gap length as shown in Figs. 4.10 and 4.11. An additional solution for reducing the surface losses is to coat the solid-rotor air-gap-facing surface with a proper material. A coated rotor is more capable of operating at high speeds because the coating reduces the effects caused by the air-gap harmonics thus improving the electromagnetic performance of the solid-rotor-core.

With the frequency converter supply, the efficiency of the motor was increased from 0.90 to 0.91 when the thickness of the rotor coating pad was increased from 1.5 mm to 3.0 mm, in the point of the nominal torque. However, the power factor of the motor decreased from 0.71 to 0.69 and the slip increased from 0.92 to 0.99 per cent. Hence, it seems that the coating pads made of Fe52 contribute in addition to the rotor surface losses also to the torque of the machine even though a large aluminium cage is used. The permeabilities of the pad materials

1 and 2 are also lower than that of Fe52, which causes some increase in the magnetizing current of the machine.

Approximately an improvement of one per cent in the efficiency of the motor was achieved, the power factor of the motor decreased 4.5 per cent, and the slip increased from 0.96 to 1.00 per cent when the ratio ($\rho_{coating}$ / ρ_{Fe52}) was increased from 1.00 to 4.60. Figure 3.18 shows that the higher the resistivity of the coating material is, the lower the losses of the solid-rotor are. It can be also seen that the slip of the motor increases while the coating is not producing torque as well as the core material.

4.8 Summary

The effects of the air-gap length, rotor teeth depth, rotor yoke depth, rotor coating pad thickness and resistivity on the rotor efficiency, power factor, and slip were studied with measurements. It was shown that all these variables have significant effects on the motor performance. However, when the optimum rotor design is chosen, some compromises have to be made. It is not possible to concurrently reach the highest possible efficiency and power factor values. Because when eddy current losses on the surface of the rotor core decrease, this usually simultaneously – due to the coating material properties – leads to a lower power factor and increases the stator current. According to the measurements, some parameters for all studied variables can be given. A suitable value for the length of the air-gap in this case is 1.4 mm, for the depth of rotor teeth 20 mm, for the depth of rotor yoke 40 mm, for the length of the coating layer 3.00 mm and for the resistivity ratio of the coating 4.62. By these parameters, the efficiency of the motor is approximately 0.93, the power factor 0.67, and the slip 1.0 per cent at 200 Hz supply. This concept produces a competitive AFIM.

Table 4.5 presents the summary of the measurements. The values in Table 4.5 are nominal point values. The fundamental RMS phase voltage was 230 V in all measurements.

Table 4.5 Summary of the measured nominal point values. δ is the air-gap length, w_{dr} is the depth of the rotor teeth, w_{yr} is the depth of the rotor yoke, w_{pad} is the thickness of the coating pad.

					200Hz	200Hz	200Hz	200Hz	50Hz	50Hz	50Hz
δ[mm]	w_{dr} [mm]	w_{yr}[mm]	pad	w_{pad}[mm]	η	cosφ	s [%]	I [A]	η	cosφ	I [A]
1.9	20	45	mat1	2.5	0.94	0.64	0.98	115	0.87	0.72	114
1.4	20	45	mat1	2.5	0.92	0.67	1.00	105	0.88	0.74	104
0.9	20	45	mat1	2.5	0.91	0.70	1.02	99	0.89	0.76	98
1.4	20	45	mat2	2.5	0.92	0.67	1.00	105	0.88	0.73	104
1.7	15	45	mat2	2.5	0.93	0.65	1.33	112	0.87	0.71	109
1.7	15	40	mat2	2.5	0.93	0.65	1.34	112	0.87	0.71	109
1.7	15	35	mat2	2.5	0.92	0.64	1.34	113	0.87	0.71	110
1.7	15	30	mat2	2.5	0.92	0.64	1.34	113	0.86	0.70	110
1.4	20	45	Fe52	3.0	0.91	0.69	0.99	106	0.87	0.73	102
1.4	20	45	Fe52	2.5	0.91	0.70	0.96	100	0.86	0.75	99
1.4	20	45	Fe52	2.0	0.91	0.71	0.94	98	0.86	0.75	96
1.4	20	45	Fe52	1.5	0.90	0.71	0.92	98	0.86	0.76	96

Comparison of the measurement results with the results found by the numerical calculations shows that despite of the inaccuracy of the calculation tools that we have today, it is possible to forecast the trends and compare different design changes. Guidelines for manufacturing a high performance AFIM were determined and confirmed.

4.9 Comparison of the FEM results with the measurements

The air-gap length has a significant influence on the characteristics of the solid-rotor-core AFIM. This is because the motor was designed for high speeds. To avoid excessive iron losses

of the stator and the rotor teeth, the air-gap length has to be increased considerably from the air-gap length value that is used in the motors that take the magnetizing current from the supply network. The rotor core of this motor type is usually fabricated from laminated steel.

In this study, three different air-gap length values 0.9, 1.4, and 1.9 mm were studied. At the nominal point of the motor, according to the measurements, the best efficiency value, approximately 0.94, was achieved when 1.9 mm length air-gap was used. However, by using this 1.9 mm length air-gap, the power factor was the lowest, approximately 0.64. The measured slip value was 0.98 per cent. According to the 2D FE calculation, the efficiency, power factor, and slip values were 0.92, 0.66, and 1.00 per cent, which may be regarded as surprisingly accurate results, especially taking into account the fact that the FEM calculations assume a sinusoidal supply. In the 2D FEM calculations, the geometry of the prototype machine was converted to normal radial-flux geometry, and the time-stepping analysis was applied.

Vogt (1996) has defined the limits for magnetic flux density in the rotor teeth and rotor yoke. The depths of the rotor teeth and yoke affect the flux density according to Eqs. (2.8) and (2.9). Rotor teeth depths: 20 and 15 mm and rotor yoke depths: 20, 25, 30, 35, 40, 45, and 50 mm, were studied. Based on the time-harmonic 3D FEM calculations only, it was impossible to conclude which one of these two rotor teeth depths was the best one. However, the flux densities with both rotor teeth depths were at an acceptable level, according to Vogt (1996). Additionally, based on the time-harmonic 3D FEM, the rotor yoke depth should be at least 40 mm. If the rotor yoke were thinner than 40 mm, the flux density value, according Vogt (1996), would be too high. Of course, time-harmonic calculations are not very accurate, yet some indications can be achieved.

The effects of the depth of the rotor teeth and rotor yoke on the performance characteristics of the studied AF motor were also studied with measurements. According to the measurement at the nominal point of the motor, the better power factor value, approximately 0.67, was achieved when 20 mm deep rotor teeth were used. With the 20-mm-depth of the rotor teeth, the efficiency of approximately 0.92 was lower and both the slip and the slip losses were smaller compared with the thinner rotor teeth. However, as it was mentioned in Chapter 4, the air-gap was somewhat longer, when the load tests were performed for the motor with 15 mm deep rotor teeth. The longer air-gap smoothens the air-gap flux density efficiently and decreases the harmonic losses on the rotor surface. However, according to the measurements, the better power factor and efficiency values were achieved when a 40 mm or thicker rotor yoke was used. The changes in the slip value were smaller when the depth of the rotor yoke was changed.

The elimination of the air-gap harmonic fields increased the electrical efficiency of the motor. This is because the current linkage distribution in the air-gap is smoother, and the rotor losses are thereby decreased. When the total loss in terms of the output power was considered, the effects of the high-resistivity coating pads and well conducting copper ring on the electrical efficiency of the motor was significant. According to the time-stepping 2D FEM calculations, the rotor total losses were decreased approximately by 45 per cent, shown in Fig. 4.18, when the thickness of the coating material was 2.5 mm and the coating material 2 was used instead of the corresponding rotor core material Fe52. Figure 4.22 illustrates the calculated efficiency and power factor.

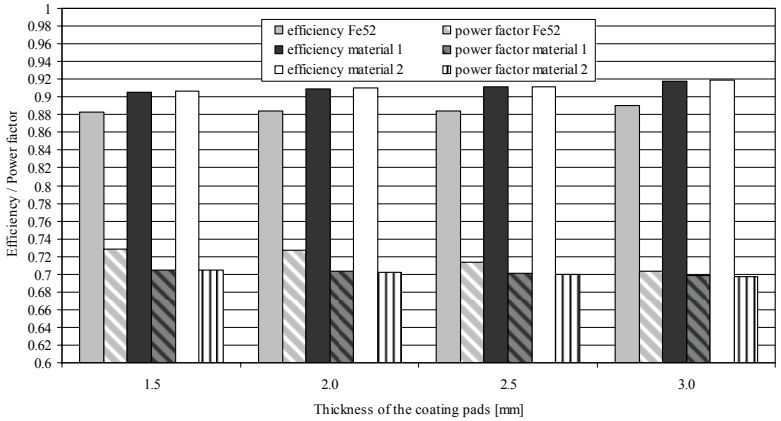

Fig. 4.22 Efficiency and power factor at the nominal point of the motor as a function of coating material thickness. Rotor coating materials Fe52, material 1, and material 2 and coating material thicknesses 1.5, 2.0, 2.5, and 3.0 mm were applied. Calculations were performed with the time-stepping 2D FEM. The line-to-line supply voltage 400 V and frequency 200 Hz was used. The rotor core material was Fe52. The depth of the rotor teeth was 20 mm and the length of the air-gap 1.4 mm. The power factor and efficiency values at the nominal point of the motor are 0.60 and 0.90 per cent respectively when a 2.5 mm thick coating ring of material 2 is used. For comparison: when the 2.5 mm thick copper ring was applied the efficiency and power factor were 0.64 and 0.91.

Based on the numerical calculations, the best efficiency value was achieved of about 0.92, when the 3.0 mm thick coating pads fabricated from the material 2 were used. Equal rotor losses were achieved when a 2.5 mm thick copper ring was applied as the rotor coating. Nevertheless, the use of the copper ring cannot be recommended in this case because it causes a lower power factor value and consequently higher stator copper losses in the motor.

The best efficiency value was achieved with coating pads made of the material 2. Simultaneously, with this material 2, the power factor value was lower than the other ferromagnetic coating pads. The slip increased, when the resistivity of the coating material was increased. This is because the coating does not produce torque as well as the core material. According to the numerical calculations, the copper coating ring should give a remarkable torque contribution to the rotor and, as a result, also a low slip value compared with the rotors in which poorly conducting coating pads are used.

The coating material Fe52 was used, when the effects of the thickness of the coating on the performance characteristics of the motor were studied with measurements. It was noticed that when the thickness of the coating was increased, the efficiency and the slip of the motor were increased, and the power factor decreased at the nominal point of the motor. When the coating pads and the rotor core were manufactured from the same material, the rotor apparent resistance and also the slip increased. The slip losses do not, however, increase to a harmful extent. Also FEM calculations confirm the phenomena of the efficiency and power factor when Fe52 is used as a coating material. Generally, it is evident that Fe52 is not a good coating material if a good efficiency of the motor is a design target. Other coating materials have to be considered instead.

5. Conclusion

The target of this research work was to study the properties of the solid-rotor-core AFIM. The prototype motor studied was of one-rotor-one-stator type, and thus there was only one air-gap between the rotor and the stator. The rated power of the prototype motor was 45 kW and the no-load operating speed 6000 min^{-1}. The motor speed was designed to be higher than what can be reached directly by network frequency. The benefits of this kind of a higher speed AF motor are: the axial length is short and the motor can be integrated directly into the working machine such as a pump or a fan.

To the author's knowledge, there are no publications on the design or optimization of the solid-rotor-core AFIM; neither the prototype motor studied in this work is a result of any special optimization process, but its dimensions are based on the practical knowledge of AXCO-Motors Oy. Therefore, the main objective of this work was to find out design specifications and guidelines on the performance characteristics of one-rotor one-stator axial-flux induction motors.

A 2D/3D FEM-based calculation model for the solution of time-transient and time-harmonic eddy current problems is introduced. The most relevant problem especially in 3D FEM calculations is the control of the size of the mesh within the skin depth regions, that is, the regions of the rotor coating and the rotor itself. In 3D modelling, the mapped mesh generator is used for meshing the air-gap and rotor coating pads. When the mapped mesh generator is used, the user has full control over the number and quality of the elements. Generally, in 3D modelling, the extrusion mesh generator is applied to provide a layered surface and volume mesh on the domain obtained by extrusion. The results from the simulations compared with the measurements show that the calculation models are accurate enough for AFIM design purposes.

The aim of this work was not to develop any specific analytical design program for the AFIM. A central contribution of the thesis is that the results from the measurements and FEM calculations provide specifications for design and guidelines on the performance characteristics of one-rotor one-stator AFIMs. Some analytical design considerations of a one-rotor-one-stator AFIM are given. However, no particular optimization procedure is presented, because the performance analysis of the AF induction motor is very complicated owing to the disc-shape geometry and the saturation effect in the solid-rotor-core. Optimization would require 3D time-stepping FE calculations. Computation of the numerical field in 3D gives accurate results, but it is very cumbersome, time-consuming and hence too expensive for present-day personal computers, and cannot therefore be used in machine design optimization.

From the cost point of view, the rotor core should be as thin as possible to achieve material savings. Because the rotor of the motor was fabricated from solid materials, there were no mechanical limitations for the thickness of the rotor. However, the flux densities in different parts of the rotor core set limits for the rotor thickness. According to the time-harmonic 3D FEM and measurements, the depth of the rotor teeth should be at least 20 mm and the depth of the rotor yoke at least 40 mm. In particular, the rotor yoke dimensions are difficult to define without 3D FEM tools, since it is impossible to evaluate accurately the eddy current distribution in the yoke by using analytic tools.

Reductions of the effects of the harmonics on solid-rotor RFIMs in order to increase the efficiency of the machine are extensively discussed in the literature. The main task, when

solid-rotor induction machines are designed, is to find out an air-gap form that would give a non-disturbed flux density distribution on the rotor surface. The permeance harmonics can be reduced by modifying the stator slot opening (a quarter of a circle nodule on both sides of the slot opening), by making the stator slot opening as small as possible, by increasing the air-gap length, and by using some semi-magnetic material (semi-magnetic slot wedges) to close the stator slot openings. All these methods smoothen the flux density distribution under the slot opening and reduce the losses on the rotor surface. A traditional and very probably the most effective method to suppress the winding harmonics resulting in a better efficiency is the use of two-layer windings. Additionally, the ratio W/τ_p should be selected such that the value for the leakage factor (Eq. 2.28) gives the minimum value. Two-layer windings have not usually been used in small machines, but in solid-rotor and especially in high-speed machines, these winding types should be used. By considering these aspects, the stator slot openings of the prototype AFIM were closed with semi-magnetic wedges, and double-layer 7/9- or 8/9-short pitch windings were used. The air-gap length was determined by the time-stepping 2D FEM and measurements. When the air-gap was increased, the stator copper losses increased, and when the air-gap length decreased, the rotor eddy current losses caused by air-gap harmonics increased. Thus, the selected air-gap length was a compromise between the motor power factor and efficiency.

Additionally, the losses on the rotor surface of the AFIM can be reduced by coating the rotor with a suitable layer of a material that forms either as high or as low a surface impedance (Eq. 3.5) as possible. The small conductivity increases the depth of penetration, but using a poorly conducting coating gives the same effect as increasing the air-gap; it smoothens the flux density distribution before the flux penetrates into the rotor core material. In this study, three different, commercially available coating materials and four different coating material thicknesses were studied on the performance of the prototype AFIM. The best performance was achieved, when the ratio of the coating material and rotor core material was 4.60 and the thickness of the coating material was 2.5 mm. Also well conducting coating were studied and quite good results may be found by using them, too. However, in this case the ferromagnetic high resistivity coatings produces slightly better results.

It may be concluded that the solid-rotor-core AFIM can be integrated directly into the working machine. However, the solid-rotor-core AFIMs are characterized by a low power factor value. The poor power factor value is the main problem when designing these kinds of solid-rotor-core AFIMs. Further, in a well-designed solid-rotor-core AF motor, the harmonic losses may be reduced to a level at which the efficiency of the machine will not be decreased compared with commercial squirrel cage RF machines of the same power. When the construction of the rotor is optimized, special attention has to be paid to the flux densities in the rotor. Generally, the results of this thesis give guidelines for designing the AF solid-rotor-core induction motor. The effect of the frequency converter supply on the efficiency of the motor studied is notable, and thus a further recommendation is to investigate the influence of switching patterns of the converter.

References

Agarwal, P. D., 1959. *Eddy-current losses in solid and laminated iron*. AIEE Transaction 78, pp. 169–181.

Agarwal, P. D., 1960. *Equivalent circuit and performance calculations of canned motor*. AIEE Transaction, pp. 635–642.

Aho, T., 2007. *Electromagnetic design of a solid steel rotor motor for demanding operational environments*, Dissertation manuscript in pre-examination, Lappeenranta University of Technology.

Aho, T., Nerg, J., Pyrhönen J., 2006. *Analyzing the effects of the rotor coating on the rotor losses of medium-speed solid-rotor induction motor*. Proceedings of SPEEDAM, Taormina, Italy, 23–26 May 2006, on CD-ROM.

Albanese, R., Rubinacci, C., 1988. *Solution of three dimensional eddy current problems by integral and differential methods*. IEEE Transaction on Magnetism, vol. 24, no. 1, pp. 98–101.

Aluminium-Verlag, 1999. *Aluminium handbook*. Published by Aluminium-Zentrale, first edition, p. 704.

Alup, 2004. Leaflet: ALUP Compressoren.

Angst, G., 1962. *Polyphase induction motor with solid rotor. Effects of saturation and finite length*. AIEE Transaction P.III 81, pp. 902–909.

Atherton, W. A., 1984. *From compass to computer; A history of electrical and electronics Engineering*. London: The Macmillan Press Ltd.

AXCO MOTORS OY, 2004. *Axial flux induction electric machine*. International application number. PCT/FI2005/000367.

Bamuner, A., 2006. *Inverter switching frequency effects on the losses of a solid-core rotor axial-flux induction motor*. Master of Science Thesis. Lappeenranta University of Technology.

Bergmann, D., 1982. *Betriebseigenschaften von wärmerohrgekühlten Asynchronmaschinen mit gerillten Massivrotor und kurzschlusskäfig unter besonderer Berücksichtigung der Stromrichterspeisung.* Dissertation. TH – Aachen.

Bîrô, O., Preis, K., 1989. *On the use of the magnetic vector potential in the finite element analysis of three-dimensional eddy-currents*. IEEE Transactions on Magnetics, vol. 25, no. 4, pp. 3145–3159.

Brimer, C. M., 1978. *Electric motor*. US Patent no. 4,081,726.

Campbell, P., 1974. *Principles of a permanent-magnet axial-field D.C. machine*. Proceedings of the IEE, vol. 121, no. 12, pp. 1489–1494.

Caricchi, F., Crescimbini, F., Di Napoli, A., Santini, E., 1992. *Optimum CAD-CAE design of axial flux permanent magnet motors*. Proceedings of ICEM, Manchester, UK, 15-17 September 1992, pp. 637–641.

Caricchi, F., Crescimbini, F., Santini, E., Santucci, C., 1995. *Basic principle and design criteria of axial-flux PM machines having counterrotating rotors*. IEEE Transactions on Industry Applications, vol. 31, no. 5, pp. 1062–1068.

Caricchi, F., Crescimbini, F., Santini, E., Santucci, C., 1998. *FEM evaluation of performance of axial flux slotted permanent magnet machines*. Proceedings of IEEE Industry Applications Conference, St. Louis, Missouri, 12–15 October 1998, pp. 12–17.

Carpenter, C. J., 1977. *Comparison of alternative formulation of 3-D magnetic field and eddy current problem at power frequencies*. IEE Proceedings, vol. 124, no. 11, pp. 1062–1034.

Carter, F. W., 1901. *Air-gap induction*. Electrical world and engineering. Vol. XXXVIII, no. 22, pp. 884–888.

Cedrat, 2005. *User's guide of Flux 2D* (version 9.10) *finite element program*.

Chalmers, B. J., Hamdi, E. S., 1982. *Multi-layer analysis of composite-rotor induction machine.* Electric machines and electromechanics, no. 7, pp. 331–338.

Chalmers, B. J., Saleh, A. M., 1984. *Analysis of solid-rotor induction machines*. Proceedings IEE, vol. 131, pt. B, no. 1, pp. 15–16.

Chalmers, B. J., Woolley, I., 1972. *General theory of solid-rotor induction machines*. Proceedings IEE, vol. 119, no. 9, pp. 1301–1308.

Chan, C.C., 1987. *Axial-field electrical machines – design and applications*. IEEE Transaction on Energy Conversion, vol. EC-2, no. 2, pp. 294–300.

Cogent power Ltd, 2003. *Product catalogue*: electrical steel, non-oriented, fully processed.

Cullen, A. L., Barton, T. H., 1958. *A simplified electromagnetic theory of the induction motor, using the concept of wave impedance*. Proceedings IEE, vol. 105, no. 8, pp.331–336.

Dorairaj, K. R., Krishnamurthy, M. R., 1967. *Polyphase induction machine with a slitted ferromagnetic rotor: 1 – Analysis*. IEEE transaction on power apparatus and systems, vol. PAS-86, no. 7, pp. 844–855.

El-Hasan, T. S., Luk, P. C. K., Bhinder, F. S., Ebaid, M. S., 2000. *Modular design of high-speed permanent-magnet axial-flux generators*. IEEE Transactions on magnetics, vol. 36, no. 5, pp. 3358–3561.

Freeman, E. M., 1968. *Travelling waves in induction machine: input impedance and equivalent circuits*. Proceeding IEEE, vol. 115, no. 12, pp.1772–1776.

Freeman, E. M., Smith, B. E., 1970. *Surface impedance method applied to multilayer cylindrical induction device with circumferential existing currents*. Proceeding IEE, vol. 117, no. 10, pp. 2012–2013.

Gerling, D., Lürkens, P., 1997. *Induction Motor*. US Patent no. 5,608,281.

Gibbs, W. J., 1947. *Tooth-ripple losses in unwound pole-shoes*. Journal IEEE, vol. 94, pt. 2, pp. 2–12.

Greig, J., Freeman, E. M., 1967. *Travelling wave problem in electrical machines*. Proceeding IEE, vol. 114, no. 11, pp. 1681–1683.

Hakala, H., 2000. *Integration of motor and hoisting machine changes the elevator business*. Proceedings of ICEM, Espoo, Finland, 28–30 August 2000, vol. 3, pp. 1242–1245.

Heller, B., Hamata, V., 1977. *Harmonic field effects in induction machines*. Amsterdam, Elsevier.

Ho, S. L., Li, H. L., Fu, W. N., 1999. *Inclusion of Interbar Currents in a Network-Field Coupled Time-Stepping Finite Element Model of Skewed-Rotor Induction Motor*. IEEE Transaction on Magnetism, vol. 35, pp. 4218–4225.

Huppunen. J., 2004. *High-speed solid-rotor induction machine –electromagnetic calculation and design*. Dissertation. Acta Universitatis Lappeenrantaensis. Lappeenranta University of Technology.

Huppunen, J., Pyrhönen, J., 1997. *Filtered PWM-inverter output waveform in a medium speed (<30000 rpm) solid-rotor induction motor drive*. Proceedings of EPE, Trondheim, Norway, 8-10 September 1997.

IEC 34-2 Standard, 1972. *Methods for determining losses and efficiency of rotating from tests*.

Jamieson, R. A., 1968. *Eddy-current effects in solid, unslotted iron rotors*. Proceedings IEE 115, no. 6, pp. 813–820.

Jinning, L., Fengli, F., 1987. *Calculation of magnetic field and rotor parameters for induction motor with slitted rotor*. Proceedings of Electrical Energy Conference, pp. 306–310.

Jokinen, T., Arkkio, A., 1999. *High-speed AC motors*. Proceedings of CICEM, Xi'an, China, 29-31 August 1999.

Kesavamurthy, N., Rajagopalan, P. K., 1959. *The polyphase induction machine with solid iron rotor*. Transaction AIEE-78, pp. 1092–1098.

Kubzdela, S., Weglinski, B., 1988. *Magnetodielectrics in induction motors with disk rotor*. IEEE Transaction on Magnetics, vol. 24, no. 1, pp. 635–638.

Laurila, L., 2004. *Analysis of torque and speed ripple producing non-idealities of frequency converters in electrical drives*. Dissertation. Acta Universitatis Lappeenrantaensis. Lappeenranta University of Technology.

Lee, R., 1965. *Dynamo-electric machine stator structure*. US Patent no. 3,225,235.

Liese, M., 1977. *Verfahren zur berechnung von wirbelströmen in massive eisen*. Archiv für Elektrotechnik 59, pp. 75–85.

Lähteenmäki, J., 2002. *Design and voltage supply of high-speed induction machines*. Dissertation. Acta Polytechnica Scandinavica, Electrical Engineering Series, no. 108, HUT.

MacLean, W., 1954. *Theory of strong electromagnetic waves in massive rotor*. Journal of applied physics 25, pp. 1267–1270.

McConnell, H., 1953. *The polyphase induction machine with solid rotor*. AIEE Transaction, vol. PAS-72, pp. 103–111.

McConnell, H., Sverdrup, E., 1955. *The induction machine with solid iron rotor*. AIEE transaction, vol. PAD-74, pp. 343–349.

Morinigo, F. B., 1996. *Induction machine using ferromagnetic conducting material in rotor*. US patent no. 5,734,217.

Nerg, J., 2000. *Numerical modelling and design of static induction heating coils*. Dissertation. Acta Universitatis Lappeenrantaensis, Lappeenranta University of Technology.

Parker, L. W., 1967. *Dynamo-electric machines, and rotors therefore*. US Patent no. 3,296,475.

Parviainen, A., Valtonen. M., 2007. *Influence of the stator slot opening configuration to a performance of axial flux induction motor*. Proceedings of ISEF, Prague, Czech Republic, 13–15 September 2007.

Peesel, H., 1958. *Über das verhalten eines Asynchronmotors bei vershiedenen läufern aus massive stahl*. Dissertation. Technische Hochschule Carolo-Wilhelmina zu Braunschweig.

Perho, J., Niemenmaa, A., Jokinen, T., Arkkio, A., 1999. *Vaihtosähkökoneiden yliaaltoilmiöt*. (in Finnish)

Pillai, K. P. P., 1969. *Fundamental-frequency eddy-current loss due to rotating magnetic field. Part 1 – Eddy current loss in solid rotors*. Proceedings of IEE, vol. 116, no. 3, pp. 407–110.

Pipes, L. A., 1956. *Matrix theory of skin effect in laminations*. Journal of the Franklin Institute, 262, pp. 127–138.

Profumo, F., Zhang, Z., Tenconi, A., 1997. *Axial flux machines Drives: A new viable solution for electric cars*. IEEE Transactions on Industrial Electronics, vol. 3, pp. 1948–1954.

Pyrhönen, J., 1991a. *The high speed induction motor: calculating the effects of solid rotor material on machine characteristics*. Dissertation. Acta polytechnica Scandinavica Electrical Engineering Series no. 68, Lappeenranta University of Technology.

Pyrhönen, J., 1995. *Pyörivän sähkömoottorin suunnittelu*. (in Finnish)

Pyrhönen, J., Huppunen, J., Nerg, J., Niemelä, M., Kurronen, P., 2002. *Medium-speed induction machine permanent magnet machine comparison*. Proceeding of ICEM, Brugge, Belgium, 25–28 August 2002.

Pyrhönen, J., Kurronen, P., 1991b. *Research on solid-rotor induction machines*, part. 1. Research report EN B-73 Lappeenranta University of Technology, p. 24. (in Finnish)

Pyrhönen, J., Kurronen, P., 1994. *Increasing the efficiency of high-speed solid-rotor induction machines*. Proceedings of ETEP, vol. 4, no. 2, pp. 301–310.

Rajagopalan, P. K., Balarama Murty, V., 1969. *Effects of axial slits on the performance of inducition machines with solid rotors*. IEEE Trasaction PAS 88, pp. 1695–1709.

Richter, R., 1954. *Electrische Maschinen*: Band IV. 2. Auflage. Birkhäuser Verlag, Basel. p. 440.

Richter, R., 1967. *Electrische Maschinen*: Band I. 3. Auflage. Birkhäuser Verlag, Basel. p. 691.

Riepe, F., 1981a. *Eindimensionale Berechnung der Drehstrom-Asynchronmaschine mit ungenutetem Stromverdrängungsläufer*. Archiv für Elektrotechnik 63, pp. 253–259.

Riepe, F., 1981b. *Zweidimensionaler rechnergestützter Entwurf von Drehstrom-Asynchronmaschinen mit massiven Läufern*. EtzArchiv 3, no. 3, pp. 71–75.

Saari. J., 1998. *Thermal analysis of high-speed induction machines*. Dissertation. Acta Polytechnica Scandinavica Series no. 90.

Sarna, M. S., Soni, G. R., 1972. *Solid rotor and composite rotor induction machines*. IEEE transaction on aerospace and electronic systems, vol. 8, no. 2, pp. 147–155.

Senckel, K., 1976. *Two-phase asynchronous motor*. US Patent no. 4,095,150.

Sharma, N. D., Anbrasu, R., Dangare, A. Y., Bhattacharjee, B., 1996. *Experimental investigation on high-speed solid and composite rotor induction motor*. Proceeding of PEDES, vol. 2, pp. 913–919.

Silvester, P., Ferrari, R., 1990. *Finite elements for electrical engineering*. Cambridge university press.

Steele, C., 1987. *Numerical computation of electric and magnetic fields*. Van Nostrand Reinhold Company Inc., New York.

Stenbacka, 2006. *Product catalogue*: MAGNOVAL 2067.

Stoll, R. L., Hammond, P., 1965. *Calculation of magnetic field of rotating machines: part 4. Approximate determination of the field and losses associated with eddy currents in conducting surfaces*. Proceedings of IEE, vol. 112, no. 11, pp. 2083–2094.

Vogt, K., 1983. *Elektrische Maschinen. Berechnung rotierender elektrischer Maschinen*. Dritte bearbeitete Auflage, Berlin, Veb Verlag Technik.

Vogt, K., 1996. *Berechnung elektrischer Maschinen*. VCH Verlagsgesellschaft mbl Weinheim.

Wood, A., Concordia, C., 1960a. *An analysis of solid rotor machines: Part I. Operational impedance and equivalent circuits*. AIEE transaction power apparatus and systems, vol. 78, pp. 1657–1665.

Wood, A., Concordia, C., 1960b. *An analysis of solid rotor machines: Part IV. An approximate nonlinear analysis*. AIEE transaction PAS, vol. 79, pp. 26–31.

Webb, J. P., Forghani, B., 1990. *A scalar-vector method for 3D eddy current problems using edge elements*. IEEE transaction on magnetics, vol. 26, no. 5, pp. 2367–2369.

Webb, J. P., Forghani, B., 1995. ***T***-Ω *method using hierarchal edge elements*. IEE Proceedings – Science, Measurement and Technology, vol. 142, no. 2, pp. 133–141.

Yamada, H., 1970. *Calculation of torque characteristics of solid-rotor induction machines*. Electrical engineering in Japan, vol. 90, no. 2, pp. 1–9.

Yee, H., Wilson, T., 1972. *Saturation and finite-length of composite-rotor induction machines*. Proceedings of IEE, vol. 119, no.7, pp. 877–882.

Appendix A

The design process of a RF machine can be carried out in the following order presented in Fig. A.1 (Pyrhönen, 1995). This procedure cannot be directly applied to the AFIM, but it can be adopted into the design of AFIMs.

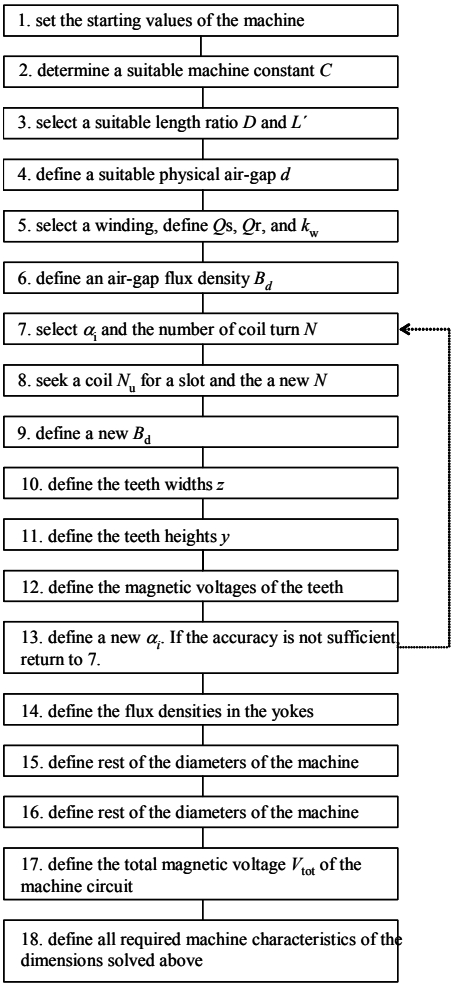

Fig. A.1. Process of the design of a rotating electric machine (Pyrhönen, 1995).

Below, the design procedure of the AFIM based on Fig. A.1 is presented in brief.

1. The starting design parameters are checked up.

2. The tangential stress is determined according to Eq. (2.5).

3. A suitable stator stack length l_e is determined based on Eq. (2.1).

4. A suitable air-gap is defined for the machine.

5. A suitable stator winding is selected for the machine. A guiding principle is that a poly-phase winding produces the more sinusoidal current linkage the more slots there are in the stator (Pyrhönen, 1995). A suitable stator and rotor slotting is selected for the machine according to Richter (1954). The winding factor decreases the harmonics that the number of slots increases. The winding factor depends on the ratio W/τ_p. The ratio W/τ_p should be selected such that the leakage factor Eq. (2.28) achieves its minimum value.

6. Since the tangential stress has already been selected, the air-gap flux density B_δ has to correlate with the selected tangential stress. The starting value can be selected according to Vogt (1996).

7. The required number of coil turns N in the phase windings of the AF machine can be calculated in the same way as it is calculated in the case of RFIMs. However, the saturation factor α_l has to be determined separately in every sub-area shown in Fig. 2.3.

8. The number of bars per slot can be determined with the same procedure as with RFIMs.

9. A new air-gap flux density value has to be calculated, because the selection of the number of turns of a phase winding has an effect on the air-gap flux density value.

10. The flux densities on the stator and rotor teeth are selected similarly as for normal machines according to Vogt (1996). In the case of AFIMs, the flux densities are determined separately in every sub-area shown in Fig. 2.3, because the teeth width increases with the increasing core diameter. Thus, when selecting the widths b_s and b_r it has to be noticed that τ_r and τ_s have different values in the inner and outer radii of the motor. Thus, the flux density is higher in the inner parts than in the outer parts of the motor.

11. When selecting the teeth height the same procedure as with RFIMs can be used.

12. The magnetic voltages of the teeth are calculated.

13. If the new saturation factor α_l does not correspond with sufficient accuracy to the factor selected, the process returns to step 7.

14. The depths w_{yr} and w_{ys} of the rotor and stator yokes are determined. It has to be ensured that the flux density in the yokes is inside the limits given by Vogt (1996).

15. All diameters have already been selected.

16. The total magnetomotive force and the stator magnetizing current are define.

17. As the dimensions have been defined and the winding has been selected, the resistances and inductances of the machine must be calculated. In the case of AFIM, the leakage inductance and the resistance for the inner and outer end-windings have to be calculated separately, since they have different dimensions.

Appendix B

EXAMPLE

Dimensioning of the mean geometric radius r_{av} of an AFIM

Designing parameters:

$P_n = 100$ kW $p = 2$ $f_n = 200$ $s_n = 0.01$ $n_n = 5940$ min^{-1} $T_n = 160$ N

$k_D = 0.58$

$\sigma_{tan} = 14000$ Nm/m^2 σ_{tan}: 10…40 kNm/m^2

$$\frac{r_{in}}{r_{out}} = k_D \tag{B.1}$$

$$r_{av} = \sqrt{r_{out} \cdot r_{in}} \tag{B.2}$$

$$S_r = \pi\left(r_{out}^2 - r_{in}^2\right) \tag{B.3}$$

$$\sigma_{tan} = \frac{T}{r_{av} S_r} \tag{B.4}$$

Eq. (B.1) to Eq. (B.2)

$$r_{av} = r_{out}\sqrt{k_D} \tag{B.5}$$

Eq. (B.2) to Eq. (B.3)

$$S_r = \pi \cdot r_{out}^2\left(1 - k_D^2\right) \tag{B.6}$$

Eq. (B.5) and (B.6) to Eq. (B.4)

$$\sigma_{tan} = \frac{T}{r_{out}^3 \pi\sqrt{k_D}\left(1 - k_D^2\right)} \tag{B.7}$$

From Eq. (B.7)

$$r_{out} = \sqrt[3]{\frac{T}{\sigma_{tan}\pi\sqrt{k_D}\left(1 - k_D^2\right)}} = 0.193\ \text{m}$$

From Eq. (B.1) and (B.2)

$$r_{in} = k_D \cdot r_{out} = 0.112\ \text{m}$$

$$r_{av} = \sqrt{r_{out} \cdot r_{in}} = 0.147\ \text{m}$$

Appendix C

Table C.1 Material data of the slot wedges (MAGNOVAL 2067) used in the prototype motor.

Magnetic flux density [T]	0.1	0.2	0.3	0.4	0.5	0.6	0.7
Relative permeability	2.8	2.9	2.8	2.7	2.4	2.2	1.9
Magnetic field strength [A/cm]	500	1000	1500	2000	2500	3000	
Magnetic flux density [T] ± 10 %	0.17	0.32	0.46	0.56	0.64	0.69	

Table C.2 Properties of the slot wedges used in the prototype motor.

Properties	Unit	Value
Specific weight	g/cm^3	3.3 ± 0.2
Specific resistance	Ωcm	$\geq 1 \cdot 10^6$
nominal thickness	mm	2.0 – 10.0

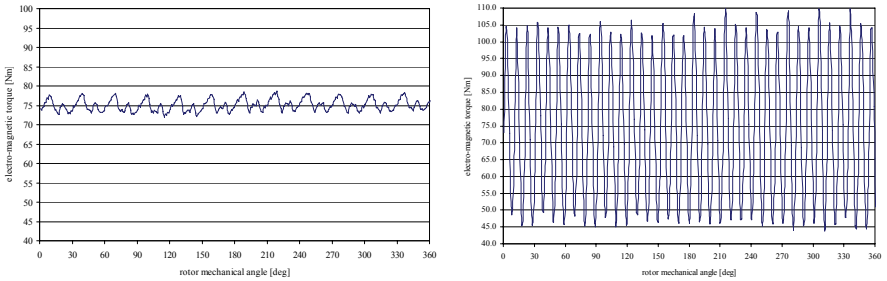

Fig. C.1 Electromagnetic torque of the studied AFIM with the rotor slot numbers 30 (left) and 36 (right).

Table C.3 Data of the prototype AFIM.

Parameter	Value
The number of stator slots	36
The number of rotor slots	30
The number of turns in one slot	6
Slots per pole and phase	3
Stator outer diameter [mm]	310
Stator inner diameter [mm]	190
Mean geometric radii [mm]	121
Air-gap length [mm]	0.9-1.9
Rotor coating pad thickness [mm]	1.5-3.0
Depth of the stator yoke [mm]	53.0
Depth of the rotor yoke [mm]	45.0-30.0
Height of the stator slot [mm]	47.0
Width of the stator slot [mm]	8.0
Depth of the rotor slot [mm]	15.0-20.0
Width of the rotor slot [mm]	9.0
Slot opening width [mm]	2.5
Slot opening height [mm]	2.6

Appendix D

The equations shown in the Appendix D have been presented by Perho et al. (1999). The values of the coefficient g appear in Eqs. (D.1) – (D.6) are g = ±1, ±2,… The harmonics caused by fundamental mmf wave and slot openings of the stator slots can be calculated with the equation

$$\nu = gQ_{\mathrm{s}} + p\,. \tag{D.1}$$

The stator slot harmonic components caused by the stator slotting are -17, 19, -35, 37, -53, 55, -71, 73, -89, and 91. The harmonics caused by the fundamental mmf wave and rotor slot opening can be calculated with the equation

$$\nu = gQ_{\mathrm{r}} + p\,. \tag{D.2}$$

The harmonic components caused by the rotor slotting are -14, 16, -29, 31, -44, 46, -59, 61, -74, 76, -89, and 91. The winding harmonics caused by the double-layer winding of the stator are calculated with

$$\nu = (2mg + 1)p\,. \tag{D.3}$$

The harmonic components -5, 7, -11, 13, -17, 19, -23, 25, -29, 31, -35, 37, -41, 43, -47, 49, -53, 55, -59, 61, -65, 67, -71, 73, -77, 79, -83, 85, -89, 91, -95, 97 are caused by the double-layer stator winding, according to Eq. (D.3). The harmonics caused by the fundamental rotor current wave and the saturation of the rotor

$$\nu = gQ_{\mathrm{r}} + 3p\,. \tag{D.4}$$

$$\nu = gQ_{\mathrm{r}} - p\,. \tag{D.5}$$

The harmonic components calculated from Eq. (D.5) are -12, 18, -27, 33, -42, 48, -57, 63, -72, 78, -87, and 93. The harmonic components calculated from Eq. (D.6) are -16, 14, -31, 29, -46, 44, -61, 59, -76, 74, -91, and 89.

The cage rotor reacts to the flux density harmonics created by the stator. The harmonic ν of the resultant flux density of the air-gap can create rotor harmonics n according to Eq.

$$n = \nu + \frac{Q_{\mathrm{r}}}{p} \cdot g\,, \tag{D.6}$$

where g is 0, ±1, ±2,… These harmonics are listed in Table D.1.

Table D.1. Harmonics caused by the aluminium cage.

ν/*n*	**0**	**-1**	**1**	**2**	**-2**	**3**	**-3**	**4**	**-4**	**5**	**-5**	**6**	**-6**
-5	-5	10	-20	25	-35	40	-50	55	-65	70	-80	85	-95
7	7	22	-8	37	-23	52	-38	67	-53	82	-68	97	-83
-11	-11	4	-26	19	-41	34	-56	49	-71	64	-86	79	-101
13	13	28	-2	43	-17	58	-32	73	-47	88	-62	103	-77
-17	-17	-2	-32	13	-47	28	-62	43	-77	58	-92	73	-107
19	19	34	4	49	-11	64	-26	79	-41	94	-56	109	-71
-23	-23	-8	-38	7	-53	22	-68	37	-83	52	-98	67	-113
25	25	40	10	55	-5	70	-20	85	-35	100	-50	115	-65
-29	-29	-14	-44	1	-59	16	-74	31	-89	46	-104	61	-119
31	31	46	16	61	1	76	-14	91	-29	106	-44	121	-59
-35	-35	-20	-50	-5	-65	10	-80	25	-95	40	-110	55	-125
37	37	52	22	67	7	82	-8	97	-23	112	-38	127	-53
-41	-41	-26	-56	-11	-71	4	-86	19	-101	34	-116	49	-131
43	43	58	28	73	13	88	-2	103	-17	118	-32	133	-47
-47	-47	-32	-62	-17	-77	-2	-92	13	-107	28	-122	43	-137
49	49	64	34	79	19	94	4	109	-11	124	-26	139	-41
-53	-53	-38	-68	-23	-83	-8	-98	7	-113	22	-128	37	-143
55	55	70	40	85	25	100	10	115	-5	130	-20	145	-35
-59	-59	-44	-74	-29	-89	-14	-104	1	-119	16	-134	31	-149
61	61	76	46	91	31	106	16	121	1	136	-14	151	-29
-65	-65	-50	-80	-35	-95	-20	-110	-5	-125	10	-140	25	-155
67	67	82	52	97	37	112	22	127	7	142	-8	157	-23
-71	-71	-56	-86	-41	-101	-26	-116	-11	-131	4	-146	19	-161
73	73	88	58	103	43	118	28	133	13	148	-2	163	-17
-77	-77	-62	-92	-47	-107	-32	-122	-17	-137	-2	-152	13	-167
79	79	94	64	109	49	124	34	139	19	154	4	169	-11
-83	-83	-68	-98	-53	-113	-38	-128	-23	-143	-8	-158	7	-173
85	85	100	70	115	55	130	40	145	25	160	10	175	-5
-89	-89	-74	-104	-59	-119	-44	-134	-29	-149	-14	-164	1	-179
91	91	106	76	121	61	136	46	151	31	166	16	181	1
-95	-95	-80	-110	-65	-125	-50	-140	-35	-155	-20	-170	-5	-185
97	97	112	82	127	67	142	52	157	37	172	22	187	7

ACTA UNIVERSITATIS LAPPEENRANTAENSIS

241. TENHUNEN, JARKKO. Johdon laskentatoimi kärkiyritysverkostoissa. Soveltamismahdollisuudet ja yritysten tarpeet. 2006. Diss.

242. KEMPPINEN, JUKKA. Digitaaliongelma. Kirjoitus oikeudesta ja ympäristöstä. 2006.

243. PÖLLÄNEN, KATI. Monitoring of crystallization processes by using infrared spectroscopy and multivariate methods. 2006. Diss.

244. AARNIO, TEIJA. Challenges in packaging waste management: A case study in the fast food industry. 2006. Diss.

245. PANAPANAAN, VIRGILIO M. Exploration of the social dimension of corporate responsibility in a welfare state. 2006. Diss.

246. HEINOLA, JANNE-MATTI. Relative permittivity and loss tangent measurements of PWB materials using ring resonator structures. 2006. Diss.

247. SALMELA, NINA. Washing and dewatering of different starches in pressure filters. 2006. Diss.

248. SISSONEN, HELI. Information sharing in R&D collaboration – context-dependency and means of governance. 2006. Diss.

249. PURANEN, JUSSI. Induction motor versus permanent magnet synchronous motor in motion control applications: a comparative study. 2006. Diss.

250. PERÄLÄ, KARI. Kassanhallintakäytännöt Suomen kunnissa. 2006. Diss.

251. POUTIAINEN, ILKKA. A modified structural stress method for fatigue assessment of welded structures. 2006. Diss.

252. LIHAVAINEN, VELI-MATTI. A novel approach for assessing the fatigue strength of ultrasonic impact treated welded structures. 2006. Diss.

253. TANG, JIN. Computational analysis and optimization of real gas flow in small centrifugal compressors. 2006. Diss.

254. VEHVILÄINEN, JUHA. Procurement in project implementation. 2006. Diss.

255. MIROLA, TUULI. Impacts of the European integration and the European Union membership on Finnish export industries – Perceptions of export business managers. 2006. Diss.

256. RAUMA, KIMMO. FPGA-based control design for power electronic applications. 2006. Diss.

257. HIRVONEN, MARKUS. On the analysis and control of a linear synchronous servomotor with a flexible load. 2006. Diss.

258. LIU, JUNHONG. On the differential evolution algorithm and its application to training radial basis function networks. 2006. Diss.

259. LAITINEN, RISTO. Development of LC-MS and extraction methods for the analyses of AKD, ASA, and rosin sizes in paper products. 2006. Diss.

260. KUISMA, PETRI. Seinärakenteen infrapunakontrastin pienentäminen käyttäen ilmajäähdytystä ja säteilysuojausta. 2007. Diss.

261. ELLONEN, HANNA-KAISA. Exploring the strategic impact of technological change – studies on the role of Internet in magazine publishing. 2007. Diss.

262. SOININEN, AURA. Patents in the information and communications technology sector – development trends, problem areas and pressures for change. 2007. Diss.

263. MATTILA, MERITA. Value processing in organizations – individual perceptions in three case companies. 2007. Diss.

264. VARTIAINEN, JARKKO. Measuring irregularities and surface defects from printed patterns. 2007. Diss.

265. VIRKKI-HATAKKA. TERHI. Novel tools for changing chemical engineering practice. 2007. Diss.

266. SEKKI, ANTTI. Successful new venturing process implemented by the founding entrepreneur: A case of Finnish sawmill industry. 2007. Diss.

267. TURKAMA, PETRA. Maximizing benefits in information technology outsourcing. 2007. Diss.

268. BUTYLINA, SVETLANA. Effect of physico-chemical conditions and operating parameters on flux and retention of different components in ultrafiltration and nanofiltration fractionation of sweet whey. 2007. Diss.

269. YOUSEFI, HASSAN. On modelling, system identification and control of servo-systems with a flexible load. 2007. Diss.

270. QU, HAIYAN. Towards desired crystalline product properties: In-situ monitoring of batch crystallization. 2007. Diss.

271. JUSSILA, IIRO. Omistajuus asiakasomisteisissa osuuskunnissa. 2007. Diss.

272. 5th Workshop on Applications of Wireless Communications. Edited by Jouni Ikonen, Matti Juutilainen and Jari Porras. 2007.

273. 11th NOLAMP Conference in Laser Processing of Materials Lappeenranta, August 20-22, 2007. Ed. by Veli Kujanpää and Antti Salminen. 2007.

274. 3rd JOIN Conference Lappeenranta, August 21-24, 2007. International Conference on Total Welding Management in Industrial Applications. Ed. by Jukka Martikainen. 2007.

275. SOUKKA, RISTO. Applying the principles of life cycle assessment and costing in process modeling to examine profit-making capability. 2007. Diss.

276. TAIPALE, OSSI. Observations on software testing practice. 2007. Diss.

277. SAKSA, JUHA-MATTI. Organisaatiokenttä vai paikallisyhteisö: OP-ryhmän strategiat institutionaalisten ja kilpailullisten paineiden ristitulessa. 2007. Diss.

278. NEDEOGLO, NATALIA. Investigation of interaction between native and impurity defects in ZnSe. 2007. Diss.

279. KÄRKKÄINEN, ANTTI. Dynamic simulations of rotors during drop on retainer bearings. 2007. Diss.

280. KARPOVA, TATJANA. Aqueous photocatalytic oxidation of steroid estrogens. 2007. Diss.

281. SHIPILOVA, OLGA. Particle transport method for convection-diffusion-reaction problems. 2007. Diss.

282. ILONEN, JARMO. Supervised local image feature detection. 2007. Diss.

283. BOTAR-JID, CLAUDIU CRISTIAN. Selective catalytic reduction of nitrogen oxides with ammonia in forced unsteady state reactors. Case based and mathematical model simulation reasoning. 2007. Diss.

284. KINNUNEN, JANNE. Direct-on-line axial flux permanent magnet synchronous generator static and dynamic performance. 2007. Diss.